Ionized and molecular gas studies to unveil AGN feedback

Darshan Kakkad

München 2017

Ionized and molecular gas studies to unveil AGN feedback

Darshan Kakkad

Dissertation
an der Fakultät für Physik
der Ludwig–Maximilians–Universität
München

vorgelegt von
Darshan Kakkad
aus Kollam, Indien

München, den 30 Mai, 2017

Erstgutachter: Prof. Dr. Andreas Burkert
Zweitgutachter: Prof. Dr. Kirpal Nandra
Tag der mündlichen Prüfung: 12 Juli, 2017

To my Family

Contents

List of Figures

List of Tables

Zusammenfassung

Starke Winde von supermassiven schwarzen Löchern in den Zentren von Galaxien werden in Simulationen oft aktiviert, um beobachtete Eigenschaften wie z.B. das obere Massenende der Galaxienmassenfunktion zu reproduzieren. Obwohl mehrere Studien im vergangenen Jahrzehnt durchgeführt worden sind, um die Auswirkung der Rückkopplung von solchen aktiven galaktischen Kernen (AGN) sowohl bei geringen als auch bei hohen Rotverschiebungen aufzudecken, erbrachten Beobachtungen bislang noch keinen direkten und überzeugenden Nachweis ihrer Auswirkung auf die Muttergalaxie. Galaxien mit Rotverschiebungen $1< z <3$ sind ideale Versuchsobjekte, um zu prüfen, welche Auswirkung Strahlungswinde auf die Muttergalaxie haben, da in diesem Zeitraum die volumengemittelte Akkretions rate der schwarzen Löcher maximal war. In der vorliegenden Arbeit werden zwei unabhängige Ansätze präsentiert, mit denen die strahlungsbedingte Rückkopplung von AGNs mit $z \sim 1.5$ untersucht werden kann. Dabei werden die sog. Integral Field Spektroskopie im optischen und nah-infraroten Wellenlängenbereich (WiFeS and SINFONI) und die Spektroskopie von Submillimeterwellen (ALMA) verwendet. Die beiden Methoden untersuchen unterschiedliche Phasen des Gases innerhalb der Muttergalaxie des AGN und liefern daher komplementäre Informationen über den Zustand der interstellaren Materie (ISM). Mit der ersten Methode, den Beobachtungen mit SINFONI zeige ich, dass die ionisierten Ausflüsse von AGNs mit hohen Massenakkretionsraten ausgedehnt sind und sich über die gesamte Muttergalaxie ausbreiten (8-10 kpc). Aufgrund von großen systematischen Unsicherheiten – in erster Linie bei der Bestimmung von Elektrondichten – ist es jedoch eine große Herausforderung, die Quelle dieser Ausflüsse zu unterscheiden, da sie entsprechend aktueller theoretischer Modelle in gleichem Maße durch Sternentstehung oder einen AGN gespeist werden könnten. Basierend auf optischen IFU Beobachtungen von nahen AGN Muttergalaxien mit WiFeS präsentiere ich räumlich aufgelöste Karten der Elektronendichte, mit dem Ziel, die Dichtewerte in der sog. narrow line region einzugrenzen und damit die systematischen

Unsicherheiten bei der Bestimmung der Ausflussstärke zu reduzieren. Bei der zweiten Methode werden ALMA CO(2-1) Beobachtungen von Galaxien verwendet, die auf der Hauptreihe von sternbildenden Galaxien liegen und einen AGN beherbergen. Die molekulare Gasmasse der AGN-Galaxien mit $z \sim 1.5$ wird verglichen mit jener von Galaxien, die keinen AGN besitzen, aber ähnliche sternentstenungsraten und stellare Massen haben. Dabei zeigt sich, dass Galaxien mit einem AGN tendenziell einen geringeren Anteil an molekularem Gas haben und ihr Gas über einen kürzeren Zeitraum abbauen (Faktor von ~ 2) im Vergleich zu den Galaxien ohne AGN, was darauf hindeutet, dass die AGN-Rückkopplung eine Rolle spielt. Die in dieser Arbeit vorgestellten Beobachtungen zeigen, dass AGNs in der Lage sind, die Eigenschaften ihrer Muttergalaxie zu beeinflussen. Allerdings sollten zukünftige Beobachtungen konzipiert werden, um systematische Unsicherheiten zu reduzieren.

Abstract

Powerful winds from super massive black holes at the centers of galaxies are often invoked in simulations to reproduce observed properties such as the high-mass end of the galaxy mass functions. While several studies have been conducted during the past decade to unveil the effect of such Active Galactic Nucleus (AGN) feedback at both low and high redshift, we are still missing direct and convincing observational evidence of their impact on the host galaxies. Galaxies at redshift $1< z <3$ represent an ideal laboratory to test effects of radiative winds on their host galaxies as it is at this epoch that the volume averaged accretion rate of the black holes were at its maximum. The following thesis presents two independent approaches to test radiative AGN feedback at $z \sim 1.5$ using optical and near-Infrared Integral Field Spectroscopy (WiFeS and SINFONI) and sub-millimeter spectroscopy (ALMA). Both the methods trace different gas phases within the AGN host galaxies with each phase giving complementary information about the Interstellar medium. In the first method using SINFONI observations, I show that ionized outflows from AGNs with high mass accretion rates are extended and sweep the entire host galaxy (8-10 kpc). However, due to large systematic uncertainties, primarily in the determination of electron densities, it is challenging to discern the source of these outflows and based on current theoretical models, they can be powered equally by star formation or AGN. Using WiFeS optical IFU observations of nearby AGN host galaxies, I present spatially resolved electron density maps with an aim to constrain the density values in the narrow line region and hence bring down the systematic uncertainties in outflow power determination. The second method utilizes ALMA CO(2-1) observations of AGNs hosted in the main sequence of star forming galaxies to compare the molecular gas content of AGN galaxies at $z \sim 1.5$ with that of star formation rate and stellar mass matched non-AGN galaxies. I find that AGN host galaxies tend to have lower molecular gas fraction and shorter gas depletion time scales (a factor of ~ 2) compared to their non-AGN counterparts indicating an AGN feedback at play. The

observations presented in this thesis demonstrate that AGNs are capable of having an impact on the host galaxy properties, however future observations should be designed to lower the systematic uncertainties.

Chapter 1

Introduction

We have come a long way to understand the nature and types of galaxies since their discovery by Kant and Wright (Kant 1905) who suggested that the Milky Way represents a finite disk of stars and that the blurred patches might be distant *nebulae* similar to the Milky Way. The discovery of Quasars just over half a century ago began a new era in astronomy, namely that of Active Galactic Nuclei (AGN, see e.g. D'Onofrio et al. 2012; Kellermann 2015) which added an interesting twist to the study of evolution of galaxies. The past 50 years have also seen the establishment of new classes of telescopes around the world and in space over a wide range of wavelengths from Radio, sub-mm, near-Infrared, optical, UV, X-rays and Gamma rays. This has pushed our observational capabilities and with high spatial and spectral resolution, AGN-galaxy co-evolution has become the forefront of extra-galactic astronomy in the past decade. In spite of this, there are a lot of challenging unanswered questions in this field such as how does the AGN affect their host galaxies, if it does? A comparison between different theoretical models and observations has given rise to both agreements and disagreements which pushes the need for a better synergy between the micro scale physics employed in the simulations with that of the macro scale observed properties. The process of AGN affecting their host galaxies over cosmic time has been popularly called "AGN feedback", which is the topic of the current thesis. This thesis presents a multi-wavelength data set from a string of instruments and my attempts to address the questions posed above. A general overview of the past work which is the foundation for the work done during the course of the PhD is described in this Chapter.

1.1 The world of galaxies: An overview

Speculations surrounding the composition of Milky Way as a collection of stars existed since the time of Democritus. However it was not until the observations by Tycho Brahe and Galileo that the speculative cosmology was put to an end which broke the ground on the nature of the diffuse *nebulae*. Mid-18th century saw the advent of various catalogs of these *nebulae* such as the Messier and the New General Catalog (NGC). The origin and nature of these objects was only settled in 1920s with Edwin Hubble's observations of Cepheid variable stars in M31 whose distance measurements far exceeded the predictions of the size of the Milky Way paving the way for an extra-galactic origin for these objects.

Today we know that the Milky Way is just one among the 2 trillion galaxies in the Universe (Conselice et al. 2016). Early classification of galaxies by Edwin Hubble represented these galaxies in a tuning fork diagram based on their morphological appearance. The commissioning of the Hubble Space Telescope (HST) saw more complicated morphology which led to further sub-classifications. An overview of the morphological classification of galaxies is beyond the scope of this thesis and we refer the reader to D'Onofrio et al. (2016) for a detailed view on this topic. For simplicity and within the scope of this thesis, we classify the massive galaxies (which consists of the Elliptical and the Spiral galaxies) into two broad categories based on their optical colors[1]- the blue galaxies (or spirals) which show an active star formation and the red galaxies (or elliptical) which have little or no on-going star formation. Often we shall refer to them as star forming and quenched galaxies respectively. Another category of galaxies, called starburst galaxies show unusually large star formation rates compared to normal star forming galaxies at similar stellar mass.

All the above types of galaxies can be distinguished based on their location on the plane of star formation rate (SFR) and stellar mass as shown in Fig. 1.1. Most of the star forming galaxies show a correlation between their SFRs and stellar mass which is generally referred as the Main Sequence (MS) of star forming galaxies. Starbursts lie above this main sequence since they have higher star formation rates compared to stellar mass matched MS galaxies. Vice versa, the red and dead Elliptical galaxies i.e. the quenched population, lie below the MS. The region between the MS and the quenched galaxies in this plane is called the green valley and the galaxies in this region are believed to be in a transition phase to

[1]This should not be taken as a strict definition as the optical colors are often subjected to obscuration by dust within the host galaxy which can change definitions.

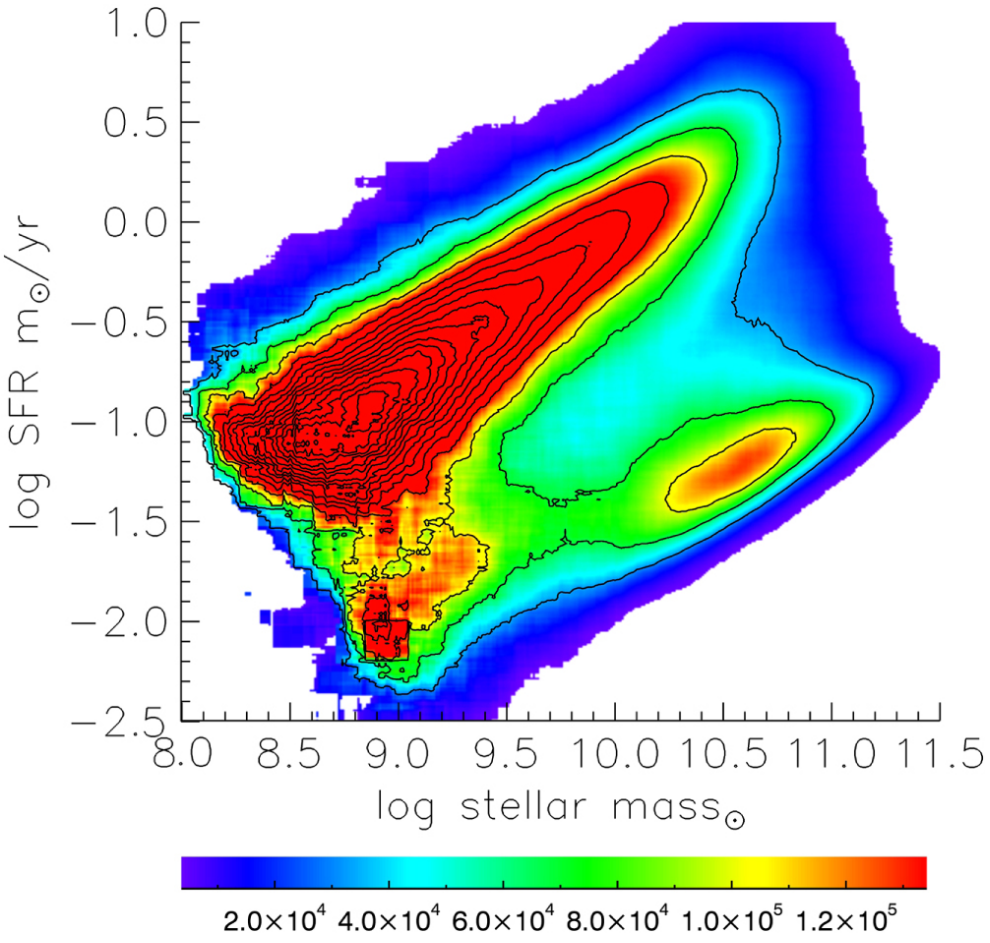

Figure 1.1: An objective view of the Main Sequence of galaxies as defined by the correlation between the SFR and stellar mass (M_*) adapted from Renzini & Peng (2015). The Main Sequence of star forming galaxies is the bright red region of this plot and the faint sequence right below this Main Sequence is populated by the quenched galaxies. All the galaxies lying in between these two sequences are called the green valley galaxies and the galaxies lying above the MS are the star burst galaxies.

being quenched.

The SFR-M_* plane represents one of the fundamental tools to classify extra-galactic sources on the basis of their star formation rates. The MS of star forming galaxies is known to evolve with cosmic time, however the correlation persists with redshift (e.g. Whitaker et al. 2012; Speagle et al. 2014; Bonzini et al. 2015; Schreiber et al. 2015; Davies et al. 2017). We discuss the latest parametrization of the MS of star forming galaxies in Chapter 4. Future references to the terminologies- Star forming, Quiescent and starburst galaxies refer to the classification scheme as outlined in Fig. 1.1.

1.2 Active Galactic Nuclei

1.2.1 A brief history

Although quasars were discovered in 1963 (Schmidt 1963), people had been looking at similar objects more than 50 years earlier (e.g. Fath 1909; Seyfert 1943). Distance measurements using highly redshifted Balmer lines in the spectra revealed an extra-galactic origin of these sources which also laid down an important role of these quasars as cosmological probes. Early quasars were mainly detected in the radio band with sources often showing the presence of massive radio jets emanating from a radio source (Fig. 1.2). Later some of these radio sources were identified with optical counterparts and were called "Quasi Stellar sources". Apart from being at large distances, they also showed unusually large line widths which led to the realization that radio sources showing such properties only formed 10% of the population of a much wider class of objects. Quasi-Stellar Objects (QSOs) showed large *blue excess* in their optical colors but had large line widths like in case of Quasars. These were later termed *Radio Quiet* sources and the former *Radio loud* sources.

The terms *Radio quiet* and *Radio loud* can often be misleading since Radio quiet sources turned out to be *Radio faint* and the definition of Radio loudness often was ambiguous. The basic property that distinguish between these two classes of AGNs is the presence or absence of a strong, relativistic radio jet. To keep matters simple, we use the terms "jetted" and "non-jetted" to refer to *Radio loud* and *Radio faint* class of objects (See Padovani et al. (2017) for more details). Both these class of objects fall under a more general term known as the "Active Galactic Nucleus" (AGN).

An AGN is the central region of a galaxy and it is believed to host a super

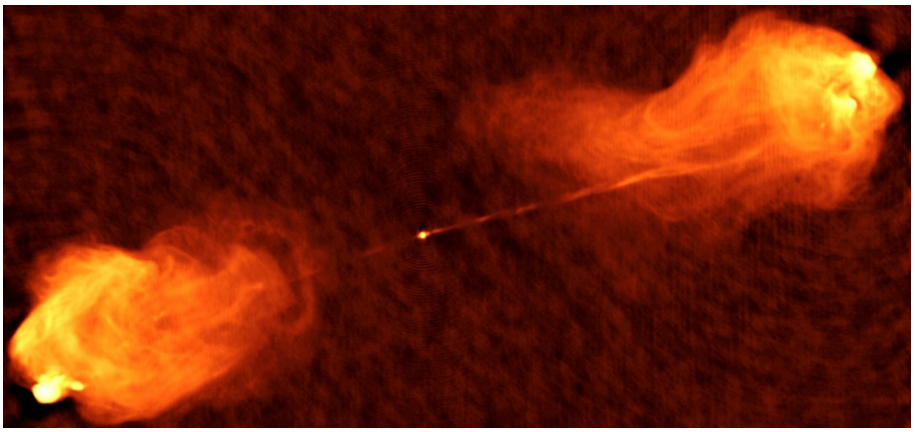

Figure 1.2: Radio jets emanating from the nucleus of the galaxy Cygnus A. The extremely energetic jets are believed to originate from an Active Galactic Nucleus. Image Credit: NRAO/AU.

massive black hole surrounded by an accretion disc and in some cases, a visible collimated radio jet. AGNs were known to be hosted at large redshifts with spectral line widths ranging from a few hundreds to thousands of km/s. A subset of these AGNs are known to be extremely luminous such that the luminosity of the AGN can outshine that of the host galaxy. Today AGNs encompass a wide range of taxonomy and it may refer to Seyfert-1s, Seyfert-2s, jetted, non-jetted, QSOs, Quasars, BL Lac, Blazars etc.. We refer the reader to Table 1 of Padovani et al. (2017) for a complete list of names used for defining an AGN over the previous years. Today we know that non-jetted AGNs form about 90% of the AGN population. A fraction of these wide range of names for AGNs can be explained using a unification model (Antonucci 1993; Urry & Padovani 1995) as discussed later in Sect. 1.2.3.

1.2.2 The black hole paradigm

Quasars being powered by the accretion of material onto a black hole has been in place shortly after their discovery (Salpeter 1964). The enormous amounts of energy released from the accretion disk as inferred from the UV/optical spectrum cannot be justified solely on the basis of nuclear fusion reactions. A more powerful and efficient mechanism such as accretion of the matter onto a black hole seemed to be the most plausible explanation. The energy released during an ac-

cretion process, L_{acc} can be described by the equation:

$$L_{acc} = \eta \dot{M} c^2 \tag{1.1}$$

where $\dot{M}$ is the accretion rate and η is the efficiency conversion from the gravitational accretion energy to radiation. η depends on the spin of the black hole (Kerr 1963; Thorne 1974) and is typically estimated to be 0.1[2]. The maximum possible L_{acc} is reached when the radiation pressure generated due to the accretion processes on to the black hole equals the gravitational pressure on the surrounding matter. At this point, the black hole is said to be accreting at "Eddington Luminosity" which is given by:

$$L_{Edd} = \frac{4\pi G M_{BH} m_p c}{\sigma_T} \tag{1.2}$$

where M_{BH} is the mass of the black hole, m_p is the proton mass and σ_T is the Thomson cross section of an electron. The ratio between the accretion luminosity and the Eddington luminosity if called the Eddington ratio, $\lambda_{Edd} = L_{acc}/L_{Edd}$ which is a useful quantity to compare accretion luminosity for a range of black hole masses. In the presence of dust, we no longer use the cross section for electrons but rather a cross section for the dust and gas together. This has been discussed in detail in Chapter 2.

Over the last couple of decades, observational evidence in different bands has also accumulated to support the notion of a black hole in the center of galaxies. In our own Milky Way, high spatial resolution kinematic studies of stars around the central radio source Sgr A* suggests the presence of a black hole (Genzel et al. 2000). Early HST observations of nearby AGNs show that the gas in the vicinity of the nuclei moves at very high velocities in opposite directions on opposite sides of the nucleus (Harms et al. 1994; Ford et al. 1998; Ho et al. 1998) interpreted as motions around a black hole.

As explained in the next section, AGNs emit radiation in a wide range of wavelengths and one of the largest amplitude and variability in the luminosity is visible in the X-ray band which is believed to originate from a hot corona around the accretion disk. X-ray observations provide the most convincing evidence of the presence of an active black hole for extra-galactic sources since the hard X-rays are originating from the central source. The following section describes the

[2]The efficiency of a fusion process would have been 0.008 which is much less than what is observed

widely accepted unified model of AGNs which explains the wide band emission from these systems.

1.2.3 A Unified model of AGN

AGNs emit radiation in a broad range of wavelengths ranging from Radio, sub-mm, far-infrared, optical/UV, X-ray and Gamma rays which is apparent from the Spectral Energy Distribution of different classes of AGNs as shown in Fig. 1.3. The shape of the SED suggests a non-thermal origin of the emission from different parts of the same system with each component contributing to a particular or multiple bands of the spectrum. The difference between a jetted and non-jetted AGN is apparent in the radio band of the SED where the jetted AGNs show a higher radio emission compared to the non-jetted ones. The unified model of AGNs proposed in early nineties (Antonucci 1993; Urry & Padovani 1995) is shown in Fig. 1.4 which explains the different classes of AGNs such as Type 1 and Type 2 as a consequence of viewing angle along different axes of the same system. The model consists of a black hole surrounded by an accretion disk and a thick dusty torus. Fast moving clouds surrounding the black hole make up the Broad Line Region (BLR, Sect. 1.3) while further out is the Narrow Line Region (NLR, Sect. 1.3). In case of jetted-AGNs, a strong relativistic jet emanates from the center. Hence, in this model an AGN viewed through a torus would appear as Type 2 since the broad line region is obscured and an AGN viewed directly onto the central engine would be classified as Type 1 AGN.

Some notable features of the SED and the plausible explanation based on the unified model presented above (Fig. 1.4) are listed below:

1. *UV and X-ray emission*: As mentioned above, the central engine is believed to a black hole powered by the accretion of the surrounding matter. The energy dissipated during the accretion process is observed in the form of photons at UV/optical wavelengths which explains the bump at the blue part of the spectrum ("Big Blue Bump" Shakura & Sunyaev 1973; Merloni 2016) along with soft excess in the X-rays. The accretion disk is further surrounded by a corona of hot electrons at a temperature of 10^5-10^6 K. The inverse Compton scattering of the UV photons from the accretion disk off the hot corona results in the emission of hard X-rays. Multiple inverse Compton scattering results in a non-thermal power law in the X-ray regime with spectrum ranging from 1 keV to hundreds of keV.

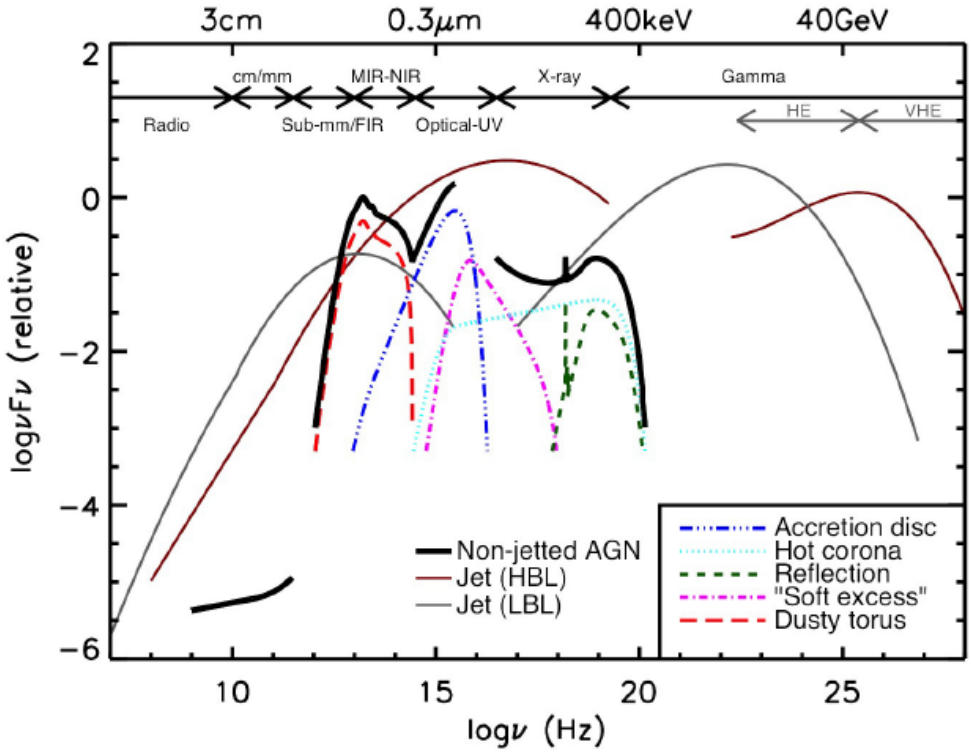

Figure 1.3: A Schematic representation of the Spectral Energy Distribution (SED) of jetted (thin solid lines) and non-jetted AGNs (thick solid black line). Various coloured dotted curves represent the emission from individual components of an AGN namely the accretion disk (blue), the corona (cyan), reflection of X-rays from the dusty torus (green), soft-excess emission from the accretion disk (magenta) and the emission from the dusty torus (red). The difference between the jetted and non-jetted AGN is apparent from the differences in the level of emission in the radio band. Adapted from Padovani et al. (2017). Image Credit: C. M. Harrison.

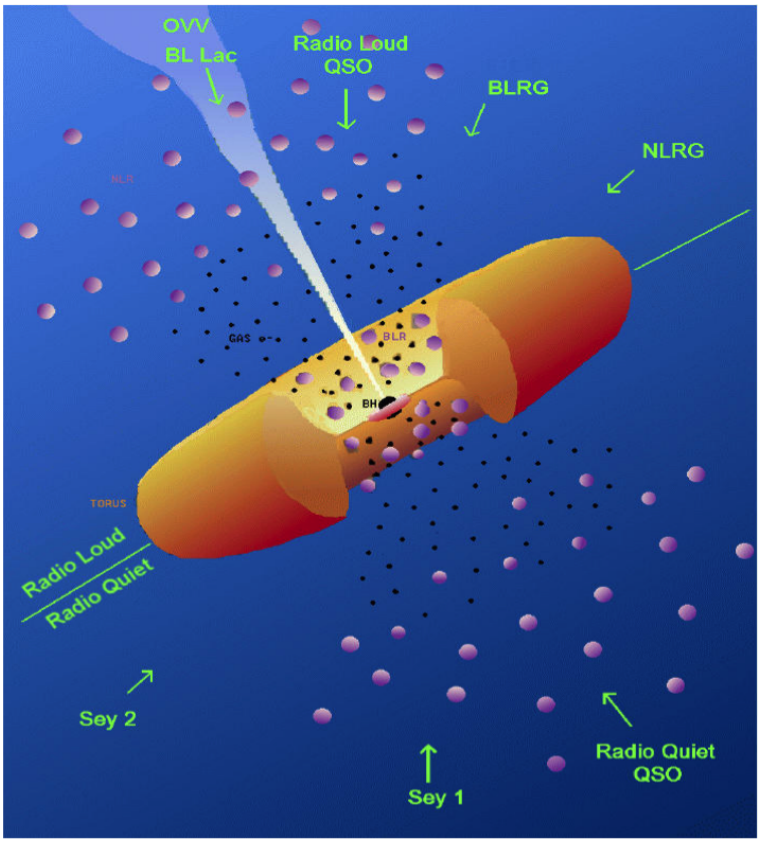

Figure 1.4: Unified model of AGN adapted from (Urry & Padovani 1995).The current accepted model proposes a black hole at the center of the galaxy surrounded by an accretion disk and a thick dusty torus shaped like a ”doughnut”. There is a hot corona on either side of the accretion disk. High velocity clouds surrounding the black hole make up the Broad Line Region (BLR) and further out is the Narrow Line Region (NLR) discussed in Sect. 1.3. Classes of AGNs such as Type 1, Type 2, Blazars etc are believed to be a consequence of varying viewing angles of the same system. At certain viewing angles, the BLR might be obscured rendering the absence of broad emission lines in the spectra.

2. *Infrared emission:* The black hole accretion disk system is further surrounded by what can be approximated to be a highly obscuring dusty torus (Hönig et al. 2006; Nenkova et al. 2008). The ionizing radiation from the accretion disk heats up the dust in the torus and the surrounding ISM which is re-emitted at mid-infrared (MIR) and far-infrared (FIR) wavelengths (Pier & Krolik 1992; Polletta et al. 2000). The dust has a range of temperatures and can be classified into hot and cold dust depending on whether the reflection is taking place from dust closest to the AGN or from the host galaxy. The infrared emission can can occur at wavelengths 1-1000 μm and depending upon the star formation rate and the luminosity of the AGNs, it can be contaminated by star formation processes as well (e.g. Lutz 2014; Mullaney et al. 2015).

3. *Radio emission:* Most of the radio emission from the AGNs is believed to originate due to Synchrotron radiation from ultra-relativistic electrons gyrating along magnetic field lines. As pointed out earlier, AGNs can be classified on the basis of their radio emission as jetted or non-jetted AGNs and they can be distinguished by their SEDs which show an enhanced emission in the radio part of the spectrum (Fig. 1.3). Jetted AGNs are associated with very strong and relativistic jets emanating well beyond the scales of the host galaxy while the non-jetted AGNs have a faint radio emission and they primarily emit through thermal radiation from the accretion disk (e.g. see reviews by Padovani 2016; Tadhunter 2016).

4. *Gamma ray emission:* Astrophysical sources emitting in the gamma rays exhibit the most extreme environments known in the Universe. Among the AGNs, Blazars dominate the gamma ray sky. The origin of the gamma rays is still debated but there are two schools of thought: a "leptonic" and "hadronic" model. In the leptonic model, the electrons (leptons) in the jet get inverse Compton scattered off their own Synchrotron radiation or an external radiation (e.g. Maraschi et al. 1992). In the hadronic model, these γ rays are believed to originate from the decay of pions as a result of proton-proton collisions. For more details about γ-ray emission in AGNs, I refer the reader to Padovani et al. (2017).

1.3 Host galaxies of AGN

Studying the properties of galaxies which host an AGN is a challenging task since at several wavelengths the emission from the AGN outshines the galaxy. It was only after the commissioning of HST that one of the first detailed images of the host galaxies of QSOs became available (e.g. Hutchings et al. 1994; Bahcall et al. 1994). It is now a well established fact that most of the QSOs in the low and high redshift universe reside in massive galaxies. However it remains still unclear whether the galaxies hosting an AGN are intrinsically different compared to galaxies without an AGN. If they are indeed intrinsically different, how does the AGN affect the host galaxy?

Some subsets of AGNs seem to prefer a particular kind of galaxy such as the jetted AGNs are known to reside in quiescent galaxies while the non-jetted AGNs tend to reside in more star forming galaxies since the radio emission is believed to originate from star formation. Hence, it is important to understand the nature of the AGN host galaxies which can give us clues about the evolution (or co-evolution) of the AGN-galaxy system.

1.3.1 Broad Line Region

As mentioned in the beginning of this chapter, one of the primary features of AGN spectra are the existence of extremely broad emission lines which span several thousand km/s. Such broad features are believed to originate from the central regions of the galaxy close to the AGN called as the Broad Line Region (BLR). In the current section, I summarize the basic properties of the Broad Line Region such as electron densities, temperatures and BLR size estimation.

The width of a line assuming thermal motions at the typical BLR temperature of 10,000 K, estimated based on line intensity ratios of ionized gases, is 10 km/s. However, the observed line width of several thousand km/s far exceed the 10 km/s limit indicating that these extreme velocities are a result of Doppler broadening due to the bulk motions of individual line emitting clouds (Gaskell 2009) in the BLR.

The electron density of the BLR is typically very high since all the forbidden emission lines are collisionally suppressed. The broad line spectrum usually has weak or absent [OIII]λ4363,4959,5007 emission which sets a minimum electron density value of $\sim 10^8 \mathrm{cm}^{-3}$ and observations of strong non-permitted lines such as CIII]λ1909 which sets an upper limit at $\sim 10^{10} \mathrm{cm}^{-3}$ (Peterson 1997).

The size and structure of the broad line region can be determined using a

technique called reverberation mapping (e.g. Peterson 1997; Mejía-Restrepo et al. 2016). Reverberation mapping uses the delayed response of the emission lines to continuum variations since any change in continuum emission takes a finite time to reach the ionized regions or the BLR clouds. The size of the broad line region can then be approximated by $r \sim \Delta t/c$ (Bentz et al. 2006).

Reverberation mapping can also be used to calculate the mass of the black holes, M_{BH} knowing the velocity width of the emission line used for reverberation mapping study using the virial theorem:

$$M_{bh} = \frac{f c \Delta t \sigma_{line}^2}{G} \tag{1.3}$$

where σ_{line} is the width of the broad line and f is a factor that depends on the structure of the BLR. Reverberation mapping is usually expensive in terms of the time invested in such studies, hence alternatives techniques to determine the black hole masses exists using scaling relations such as M_{BH}-σ and M_{BH}-M_{bulge}.

Greene & Ho (2005) present a comprehensive view of determination of black hole masses from broad lines such as H_α, H_β, $[CIV]$ and $[MgII]$ using the fact that the continuum luminosity, the emission line luminosity and the size of the broad line region are all correlated with each other. This is because harder the ionizing radiation, the more luminous will be the BLR clouds and larger the distance of the BLR.[3].

1.3.2 Narrow Line Region

The Narrow line Region (NLR) offers an ideal way to do dynamical studies of AGN host galaxies since unlike the BLR, this region is resolved due to its large spatial scale. Due to a mixture of ionizing radiation from stars and the AGN, the NLR is key to unveiling the impact of stellar and AGN feedback on galaxies. The lines emitted in the NLR are significantly narrower (FWHM $\sim$ 400 km/s) compared to those in the BLR but they are still broad compared to normal star forming galaxies which do not host an active nucleus.

Due to low densities in the NLR, many forbidden lines can be detected as they are not collisionally suppressed. Due to this, various physical quantities such as the density, temperature and the ionization state can be derived over a wide range

[3]For more details on black hole mass measurements using scaling relations or broad emission lines see Ho et al. (2012); Matsuoka et al. (2013); Wang et al. (2014); La Franca et al. (2016); Jun et al. (2015); Subramanian et al. (2016); Coatman et al. (2017)

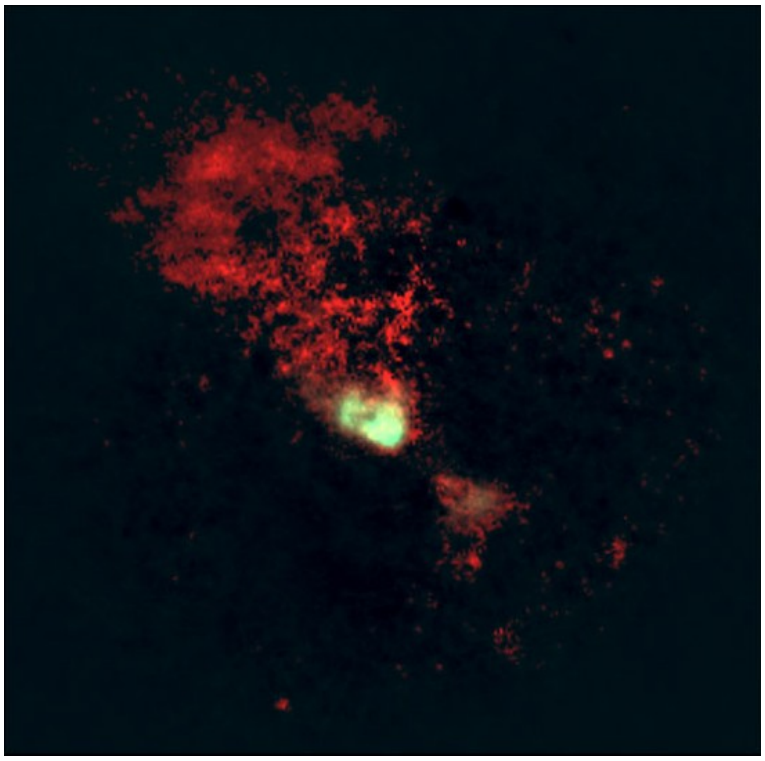

Figure 1.5: HST image of NGC5728 showing the emission morphology in the Narrow line region as traced by [OIII]λ5007 emission line. The emission is biconical in nature primarily ionized by the ionizing radiation from the AGN. Image Credit: Andrew S. Wilson (STScI)/NASA/ESA, James A. Braatz (Univ. Of Maryland), Timothy M. Heckman (STScI), Julian H. Krolik (JHU), George K. Miley (Leiden Observatory), and Allan Sandage (Carnegie Observatories)

of parameter space. One of the most widely studied set of forbidden lines in the NLR is the bright [OIII]λ4959,5007 lines. The [OIII]λ5007 is widely used in studying the structure and morphology of the NLR and is ideal for tracing ionized gas outflows in low and high redshift AGN host galaxies (see chapter 2). Other prominent emission lines visible in the NLR include the forbidden transitions [SII]$\lambda\lambda$6716,6731, [NII]6548,6585 and the permitted Balmer lines Hα, Hβ and Hγ. The intensity of most of these emission lines, however, are susceptible to the presence of dust in the host galaxy.

The size of the NLR can vary from a few hundred parsecs to a few kiloparsecs (see e.g. Bennert et al. 2006; Peterson et al. 2013). Reverberation mapping tech-

nique could not be used to discern the sizes since the time scales for the change in the emission line profiles with the changes in the continuum are much larger than the observing time scales. Observations of nearby Seyfert galaxies suggests that the NLR is not necessarily spherical, but rather shows a bi-conical morphology as inferred from the ionization cones from [OIII]λ5007 emission maps (e.g. Fig. 1.5, NGC5728: Evans et al. 1999).

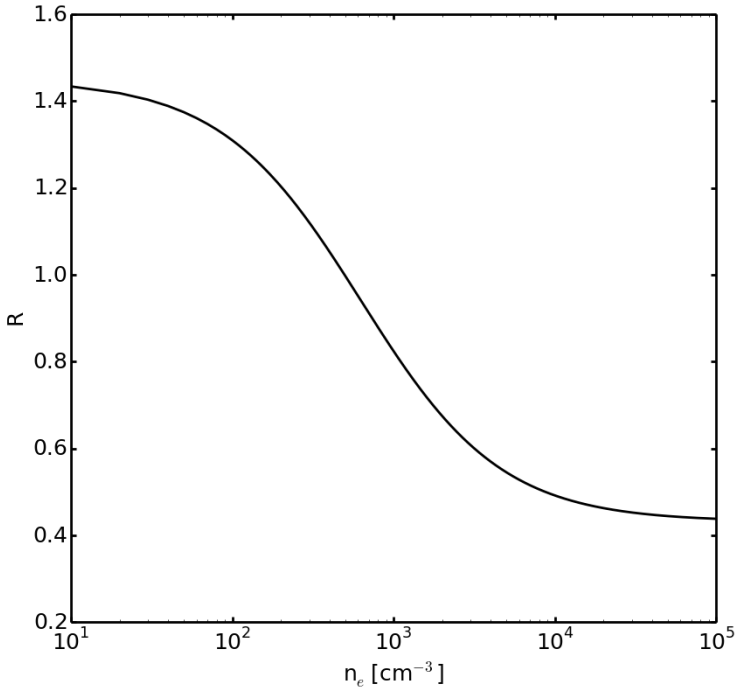

Figure 1.6: Response of the flux ratio of [SII] doublet as the ambient electron density for an electron temperature of 10,000 K. Based on Osterbrock & Ferland (2006).

The physical conditions within the NLR significantly differ from the BLR. Due to the presence of forbidden transitions such as [SII]λ6716, 6731 and [OII]λ 3726, 3729, it is possible to measure the density of this region accurately enough as long as the lines are not collisionally de-excited. These transitions occur from closely spaced excitation levels from a single ion due to which the relative fraction of the emission fluxes depend only the density of electrons occupying the higher level states. The resolving power of some of the instruments limit the use of

[OII]λ 3726, 3729 as a tracer of NLR density as the lines blend with each other. The larger separation between [SII]λ6716, 6731 makes it ideal for electron density measurements for most of the instruments. The range in densities which can be probed using the sulfur lines is $\sim 50 - 1500\text{cm}^{-3}$ where the flux ratio of the two lines uniformly decreases with increasing density as shown in Fig. 1.6. Chapter 3 of this thesis includes a study of electron density structures and profiles in the NLR of nearby Seyfert galaxies using the sulfur lines.

Similarly to the measurement of electron density, the electron temperature measurements in the NLR is ideally measured from flux ratios of emission lines from the same ion such as [OIII]$\lambda\lambda$4363, 4959, 5007 and [NII]$\lambda\lambda$5755, 6548, 6583 which are sensitive to temperature changes. Typical electron temperatures in the NLR are in the 10,000-25,000 K range.

1.4 AGN-galaxy co-evolution

Numerous studies seem to indicate that there is a co-evolution between the AGNs and their host galaxies based on linear correlations between the black hole and host galaxy properties. This is surprising given the several orders of magnitude difference in the size of the black hole and the host galaxy. A large theoretical and observational effort has been devoted in the past years to understand which influence the AGN has in shaping the host galaxy. In this section, I focus on two well established observational results which point to the evolution of the AGN and the host galaxy being linked to each other.

1 *Cosmic star formation and black hole growth history:* Fig. 1.7 shows the evolution of volume averaged star formation rate and the black hole accretion rate with cosmic time, adapted from Madau & Dickinson (2014) (see also Shankar et al. 2009). The plot clearly shows that the two quantities seem to follow the same trend with a peak star formation and black hole activity between redshift 1 and 3. This redshift is ideal for testing radiative feedback from AGNs on their host galaxies as due to the high accretion rates, the galaxies at this redshift are likely to drive winds and outflows which can potentially sweep the gas clean from the galaxies. Chapters 2 and 4 extensively discuss a few observational experiments to test this hypothesis.

2 *Black hole-Host galaxy scaling relations:* Black hole masses are found to correlate with their host galaxy bulge mass and luminosity (e.g. Kormendy

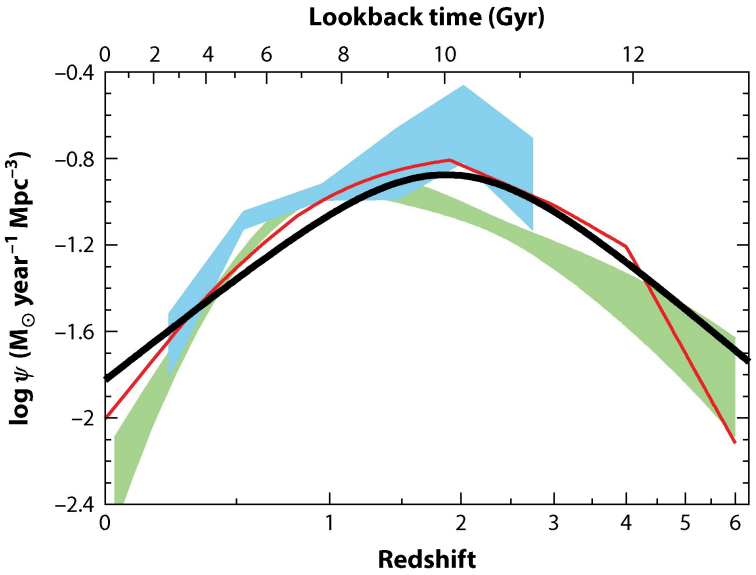

Figure 1.7: The black hole accretion rate and star formation rate (Y-axis) as a function of the cosmic lookback time (Gyr, X-axis) from Madau & Dickinson (2014). The solid black curve shows the star formation history while the other curves trace the black hole accretion rate history from X-ray (solid red curve (Shankar et al. 2009), green shade (Aird et al. 2010)) and infrared (blue shade (Delvecchio et al. 2014)). The black hole growth co-evolves with the host galaxy star formation rate over cosmic time.

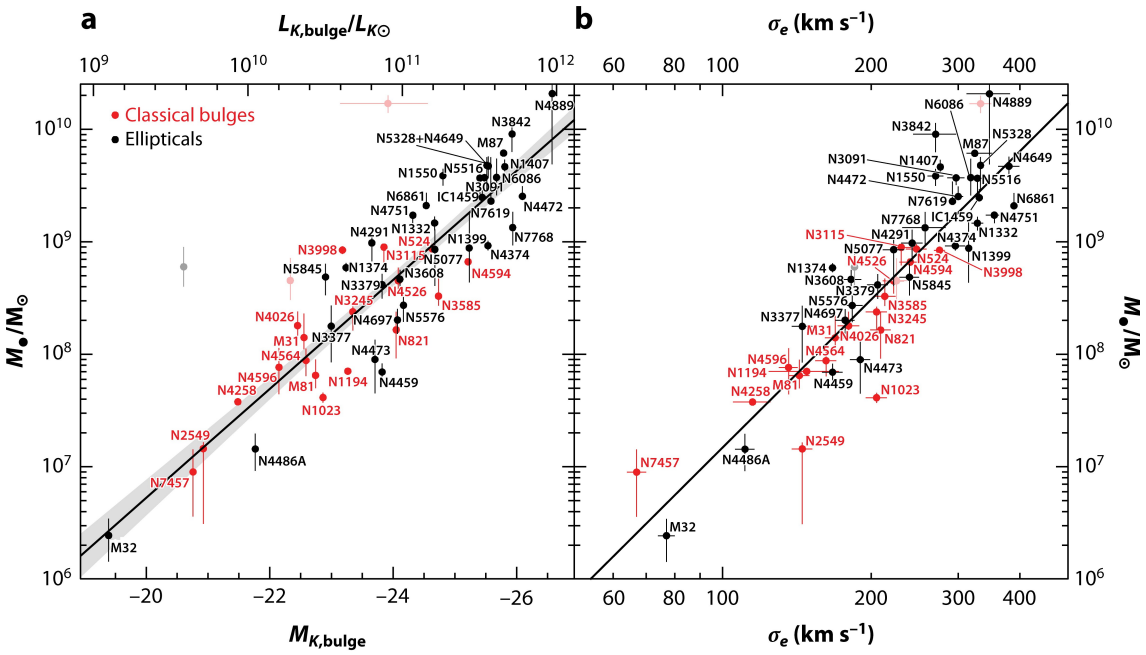

Figure 1.8: The correlation between black hole mass derived dynamically with the bulge mass (left panel) using K band magnitudes and stellar velocity dispersion (right panel) of classical bulges (red) and elliptical galaxies (black) from Kormendy & Ho (2013).

& Ho 2013; Marconi & Hunt 2003; Gültekin et al. 2009). The black hole mass also shows a tight relationship with the stellar velocity dispersion in the classical and elliptical bulges as shown in Fig. 1.8 (e.g. Tremaine et al. 2002; Shankar et al. 2016), both of which again point to the AGN influencing the growth of the central bulge in these galaxies. These scaling relations have often been used to measure black hole masses as well although for high redshift galaxies, it is a challenge to apply this technique (for a review on this topic, see Kormendy & Ho 2013).

1.5 AGN feedback

AGN feedback is the process through which the AGN interacts with the host galaxy through coupling of the radiated energy with the surrounding Interstellar Medium (ISM). As indicated in the previous section, it has been speculated that the black hole at the center of the galaxies plays a pivotal role in determining the stellar mass of the host galaxy. Theoretical simulations and observations in the past years have revolutionized the way we understand the process of AGN feedback and the following section aims to summarize the key breakthroughs in the field of AGN feedback from both an observational and theoretical point of view.

1.5.1 AGN feedback through simulations

Galaxy formation through cosmological simulations is a major challenge due to the numerous physical processes involved. Nevertheless, these simulations have done a remarkable job to bring a qualitative picture for the evolution of galaxies with the paradigm of the Cold Dark Matter (CDM) universe (Klypin et al. 2011). Current simulations employ ΛCDM cosmology where galaxies are formed at over-dense sites which bind due to gravitational forces, overcoming the Hubble expansion and collapse to form a dark matter halo.

A plethora of physical processes are included in the current models of galaxy formation which are briefly explained here (For details, see Somerville & Davé 2015). One of the main ingredients is gravity which plays a key role in merger processes triggering star formation and accretion on to the black holes. Radiative and hydrodynamical processes cool the gas which had been heated by collapse of dark matter halos. Once the gas cools down sufficiently in the central regions of the halo, self-gravitation can lead to star formation through Giant Molecular Clouds (GMC). The enormous scales of cosmological simulations make it a chal-

lenging task to understand the formation of black holes due to which the formation and growth of seed black holes are usually modeled using sub-grid recipes. These sub-grid recipes frequently employ a spherical accretion processes suggested by Bondi (1952) for the growth of black holes.

Without feedback effects, the galaxy formation models would not have been able to reproduce some of the observed properties. For example, without the presence of stellar and supernovae feedback, the star formation would be highly efficient contrary to observations. Hence theoretical models need to invoke star formation feedback to heat the surrounding medium in order to reproduce the observed efficiency of star formation. However at the high mass end, star formation feedback alone could not explain the observed lower number of galaxies (See Fig. 1.9). In this case, a much stronger processes such as AGN feedback has been invoked in order to remove or heat the gas from the host galaxies and quench the star formation. Similar to the formation and evolution of black holes, AGN feedback processes are also treated with sub-grid recipes.

AGNs may affect the host galaxies either heating the gas (Thermal feedback), or driving winds that may either sweep the gas away from the host galaxy using mechanical processes (Kinetic feedback) or ionizing it (Radiative feedback). Winds arising from black-hole accretion disk can drive shocks which can propagate feedback effects up to kpc scales (see review by Fabian 2012). We will be mostly studying the phenomenon of "Radiative feedback" within this thesis as we focus on high redshift galaxies where this mode of feedback is believed to be more prevalent.

The radiative mode of feedback is observed in black holes having a high mass accretion rate and is able to drive wide angled winds from the host galaxies (see Fig. 1.10). Apart from observations, such wide angled outflows have also been reproduced in simulations invoking AGN feedback from highly accreting black holes (Gabor & Bournaud 2014). Such outflows can be energy or momentum driven depending on the ambient conditions surrounding the ISM. In case of short cooling times, the winds are predominantly momentum driven since the momentum cannot be radiated away (Debuhr et al. 2011; King 2005; Ostriker et al. 2010). For fast winds driven by AGN and where the cooling processes are inefficient, the outflows are energy conserving. Simulations show that a 5% coupling between the output energy and the bolometric luminosity of the AGN is sufficient to drive high velocity outflows which has been observationally confirmed as molecular outflows in local ULIRGs (see Fig. 1.12, (Springel 2005; Di Matteo et al. 2005a; Zubovas & King 2012)). Such models are able also to reproduce tight scaling relations such as $M_{BH} - \sigma$, matching the observations (see Sect. 1.4).

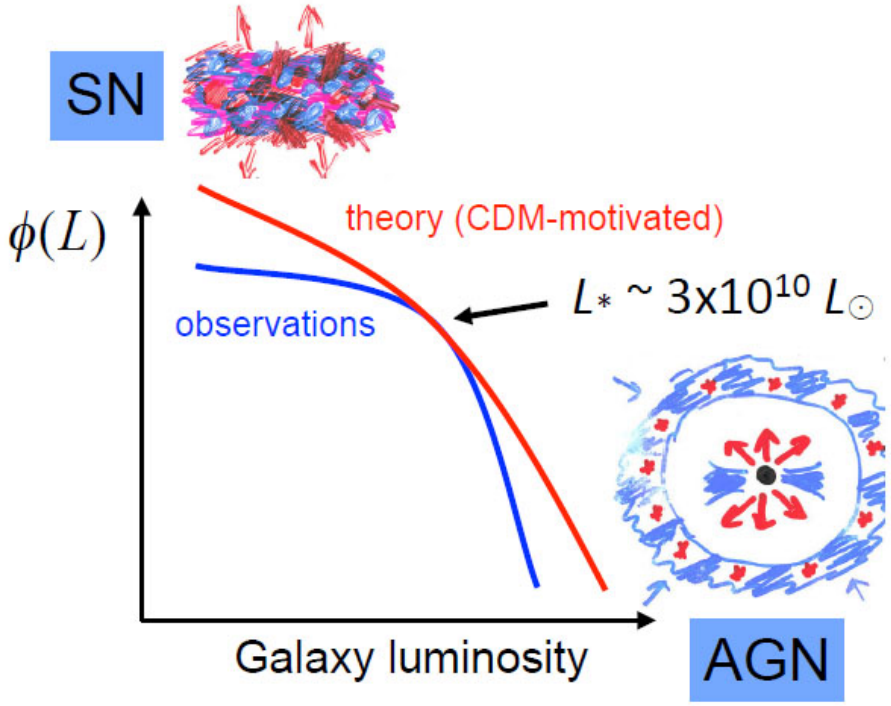

Figure 1.9: Galaxy luminosity function through observations and assuming a ΛCDM cosmology adapted from Silk & Mamon (2012). For low mass galaxies, the star formation is more efficient in comparison with what is expected from observations due to which star formation feedback has to be invoked. Similarly, at the high mass end, the star formation and supernovae feedback is not sufficient to heat the gas and a more powerful process such as feedback due to AGNs is expected to remove gas away from the host galaxies and thereby quench star formation to match the observed luminosity function.

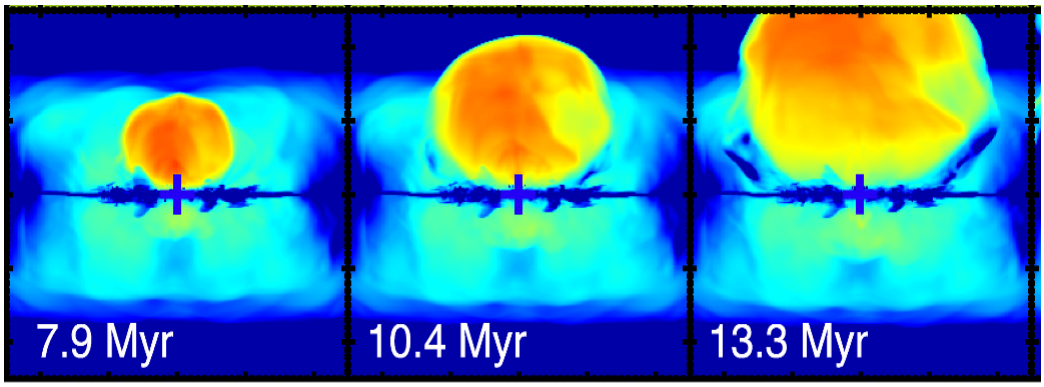

Figure 1.10: Snapshot of a radiatively driven wind from an AGN host galaxy (edge-on view) showing wide-angled high velocity outflows from Gabor & Bournaud (2014). The color-scale represents the velocity.

Apart from the scaling relations, these models are able to give insights into the outflow morphology. For example, Gabor & Bournaud (2014) showed that the outflow morphology need not necessarily be bi-conical but it can be one-sided if there is a dense material obscuring the flow of gas.

1.5.2 Kinetic AGN feedback

The Kinetic mode[4] of AGN feedback involves coupling of mechanical energy in the form of radio jets with the surrounding ISM. This type of feedback is generally observed in low-accretion rate jetted AGNs. The host galaxies of AGNs exhibiting kinetic mode of feedback usually resemble elliptical galaxies in the optical images.

The kinetic energy of these relativistic jets can far exceed the bolometric luminosity of the AGN by several orders of magnitude and the jets are responsible of the cavities or ”bubbles” seen in X-ray observations of galaxy clusters (e.g. the Perseus cluster). These are regions of hot plasma heated as a result of the interaction between the radio jet and the Intra Galactic Medium (IGM). These observation mostly in low-redshift galaxy clusters form a convincing indirect evidence for the existence of the mechanical mode of feedback from AGNs.

[4]The terms Mechnical mode, radio mode or maintenance mode are also used interchangeably

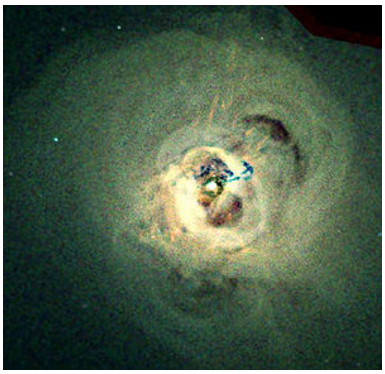

Figure 1.11: Chandra X-ray image of Perseus cluster showing bubbles in the IGM believed to be blown by relativistic radio jets from a radio source in the center (Fabian 2012).

1.5.3 Radiative AGN feedback

Radiative AGN feedback is a result of the influence of radiation pressure from the energy released due to the accretion processes onto the central black hole. Consequently, this mode of feedback is prevalent in objects which high mass accretion rates. The AGNs are in general non-jetted and the interaction between the central black hole and the surrounding ISM is primarily through radiative winds.

Assuming that a gas of mass $M_{gas} = f \cdot M_{galaxy}$ is swept by this radiation, equating the radiation pressure experienced by this mass (see Eq. 1.2) with that of the gravitational pressure gives us the following relation:

$$M_{BH} = \frac{f\sigma^4\sigma_T}{\pi G^2 m_p} \Rightarrow M_{BH} \propto \sigma^4 \tag{1.4}$$

where I have used $M_{galaxy} = 2\sigma^2 r/G$ using the virial theorem, σ being the velocity dispersion of stars in the bulge. Eq. 1.4 is the observed M-σ relation and provides an indirect observational evidence of radiative AGN feedback. The equation above was derived assuming radiation pressure only on gas. In the presence of dust, the cross section of the particles experiencing the radiation pressure increases and we can replace σ_T with $\sigma_d/1000$, which is the dust cross section assuming a Galactic dust-to-gas ratio. This is discussed in detail in Sect. 2.2.

Outflows possibly triggered by radiative winds from the AGN have been detected using observations from X-ray, optical, near-IR and sub-mm wavelengths. The velocities of these outflows range from a few 100 km/s to several 1000 km/s.

In most of these cases, the highest velocity winds (>500 km/s) have outflow powers exceeding that predicted for stellar processes as supernovae and a more stronger energy source, i.e. an AGN, has to be invoked.

Early X-ray observations of AGNs showed the presence of blue shifted absorption lines due to ionized gas outflowing towards the observer (Chartas et al. 2002; Pounds et al. 2003; Reeves et al. 2003; Cappi 2006). These X-ray observations have prompted many subsequent studies of the ionized gas in AGN host galaxies. [OIII]λ5007 is an ideal tracer of ionized gas on galaxy scale since being a forbidden line cannot be produces in high density regions, as the BLR, but rather in the extended NLR. Integral Field Spectroscopy (IFS) has proven to be a perfect tool for outflow studies since it provides spatially resolved information on the outflow morphologies and the distances involved. Numerous Integral Field Unit (IFU) observations of low as well as high redshift galaxies, including the one presented in Chapter 2, have shown evidence of the presence of ionized outflows in AGN host galaxies (Cano-Díaz et al. 2012; Rupke & Veilleux 2011, 2013; Harrison et al. 2012, 2014; Liu et al. 2013; McElroy et al. 2015; Husemann et al. 2016; Kakkad et al. 2016; Wylezalek et al. 2016; Wylezalek & Zakamska 2016; Perna et al. 2015a; Brusa et al. 2015b; Carniani et al. 2015; Cresci et al. 2015a). A fraction of these observations have found a direct evidence of suppression of star formation (negative feedback) where the outflow is prominent (Cano-Díaz et al. 2012; Cresci et al. 2015a; Carniani et al. 2016) as well as enhancement of star formation (positive feedback), probably due to shocks in the ISM at the edges of the outflow (Cresci et al. 2015a). Hence, the AGNs are possibly capable of quenching as well as enhancing star formation.

As explained later in Chapter 2, most likely ionized outflows represent just part of the story and most of the outflow mass may be in the molecular gas phase. Evidence of molecular outflows exists at very high redshift where outflow velocities >1000 km/s are observed in CII emission line profiles (Maiolino et al. 2012). Cicone et al. (2014) showed molecular outflows in local ULIRGs and found that the coupling between the kinetic energy of the outflow and the bolometric luminosity of the AGN is ∼5%, as predicted by the theoretical models of Zubovas & King (2012) for an AGN driven outflow. Currently, several on-going studies also using ALMA are focusing on molecular outflows at z∼2-3.

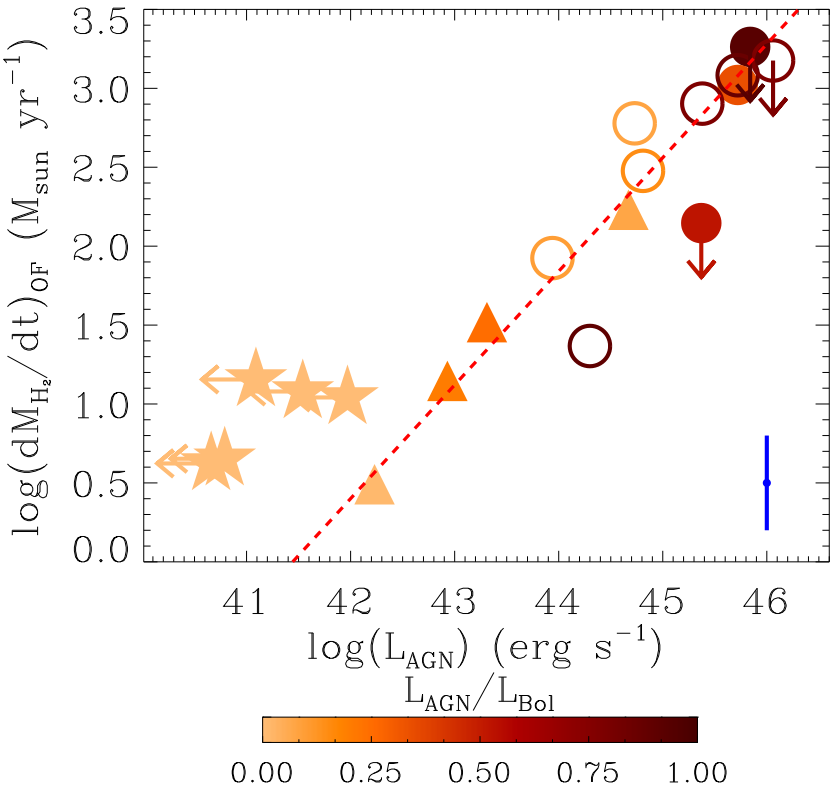

Figure 1.12: The plot shows the coupling between the molecular outflow power derived from CO observations and the bolometric luminosity of the AGN. The red dashed line is the 5% coupling line, which is the theoretical coupling value for AGN driven outflows. Filled and open circles represent AGNs, triangles are Low Ionization Nuclear Emitting Regions (LINERs) and pure star burst galaxies as the stars. The data points for AGN host galaxies clearly follow the 5% coupling trend suggesting that the observed outflows are driven by AGN (Cicone et al. 2014).

1.6 Observational tools

Using the generation of telescopes and instruments commission in the past decade, AGN feedback studies have become one of most active research topics in Extragalactic astronomy. The main aim of this thesis is to search for direct observational evidences of AGN feedback through studies of the ionized and molecular gas in high redshift galaxies using Integral Field Spectroscopy (IFS) and sub-mm spectroscopy respectively. In this section, I briefly summarize the basic aspects of these tools and the instruments used in this thesis namely, SINFONI, WiFeS and ALMA.

1.6.1 Integral Field Spectroscopy

One dimensional spectra obtained from slit spectroscopy of high redshift galaxies can be used to obtain global quantities such as the integrated flux of emission lines and overall velocity inferred from the width of these lines. However, such a technique has the limitation that we cannot get spatially resolved information about the extent of the line or continuum emission. IFS on the other hand gives a comprehensive view of spatially resolved kinematics within the host galaxy.
IFUs have three designs as briefly explained below:

- *Lenslets:* Arrays of microlenses (or lenslets) focus the image to several points which are then dispersed with a spectrograph. Though the design of such an IFU is simple, the detector space is not optimally used and the spectra have to be shortened in case of large bandwidths to avoid overlapping. The Large Binocular Telescope mid-infrared Camera (LMIRCam) is an example of an instrument which uses a lenslet based set up for its IFU.

- *Lenslets and Fibres:* To avoid the issue of non-optimal usage of detectors, the output of the lenslet can be focused on a fiber which provides a flexible output location. These fibers are then aligned together to mimic a slit which is then dispersed to give the final cube. While this set up makes up for the limitations of the lenslets, the use of optical fibers introduces loss of light. Instruments such as Gemini Multi-Object Spectrograph- IFU (GMOS-IFU) use this set up for its IFU.

- *Image slicer:* The Image slicer design is similar to the way single slit spectrographs work. The image obtained from the telescope is sliced into several rows and each of these slices are diffracted by a grating. This technique is

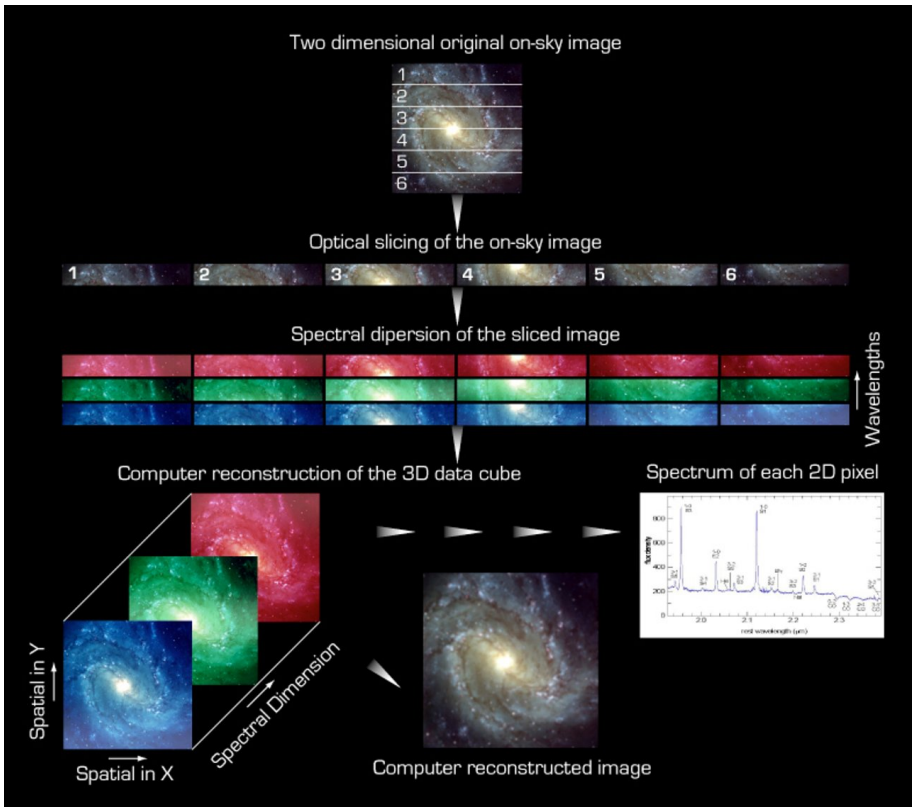

Figure 1.13: A schematic diagram showing the construction of an Integral Field image using the image slicer technique described in Sect. 1.6. Credit: ESO.

highly efficient and gives a high spatial resolution along the slices. Compared to other IFU designs, the image slicer tends to be bulkier. Fig. 1.13 shows a schematic diagram of an image slicer set up and the final cube obtained. Instruments such as SINFONI (used in this thesis) use the image slicer technique and future instruments such as HARMONI on board E-ELT will also make use of this design for its IFU.

The final product of any IFU instrument is a data cube with three dimensions: The first two dimensions representing the spatial coordinates while the third dimension represents the spectrum. Hence, such a data product would consist of an image where every pixel represents a spectrum.

The data in this thesis make use of SINFONI instrument at the Very Large Telescope (VLT) and WiFeS instrument on ANU 2.3m telescope, both of which

Instrument	Technical Specifications
SINFONI	•Field of View: 8×8, 3×3 & 0.8×0.8 arcsec •Wavelength bands:J, H, K & H+K bands •Detectors: Hawaii 2RG (2kx2k) •Pixel Scale: 125×125, 50×100 & 12.5×25 mas.
WiFeS	•Field of View: 38 ×25 arcsec •Wavelength coverage: 330 - 900 nm •Detectors: 4096 x 4096 pixel Fairchild Imaging CCD in each camera •Pixel scale: 1 arcsec (slitlet width) x 0.5 arcsec (spatial sampling along slitlets)

Table 1.1: Technical specifications of SINFONI IFU on board UT4/VLT and WiFeS IFU on board ANU 2.3m telescope. SINFONI operates in the near-infrared in the wavelength range 1.1-2.4 μm while WiFeS is an optical IFU operating the wavelength range 330-900 nm.

use the image slicer technique for an IFU. Table 1.1 summarizes the technical specifications of the IFU instruments used in this thesis.

1.6.2 Sub-mm Spectroscopy

Sub-millimeter/millimeter observations require excellent weather conditions with low water vapor since this band of wavelength is affected due to absorption by water vapor. The response of this band as a function of the Precipitable Water Vapor (PWV) content is shown in Fig. 1.14 and clearly, the atmospheric transmission changed considerably with PWV, especially at higher frequencies. The field of mm/sub-mm astronomy has boomed in the 21st century since the commissioning of highly sensitive telescopes with better spatial resolution with interferometry. Due to the low atmospheric transmission in the presence of water vapor, there are only a few sites around the world where such a telescope can be built and these include the *Llano de Chajnantor* site which hosts the Atacama Pathfinder EXperiment (APEX) telescope and Atacama Large Millimeter Array (ALMA) and *Mauna Kea* which hosts the Sub-millimeter Array (SMA). This thesis makes use of data from ALMA, hence further discussions would be limited to this facility.

ALMA is a mm/sub-mm interferometer located in Chajnantor in northern Chile's Atacama desert 5000 m above the sea level consisting of an array of 12 m and 7 m antennas with baseline capabilities of 16 km. Such large baselines

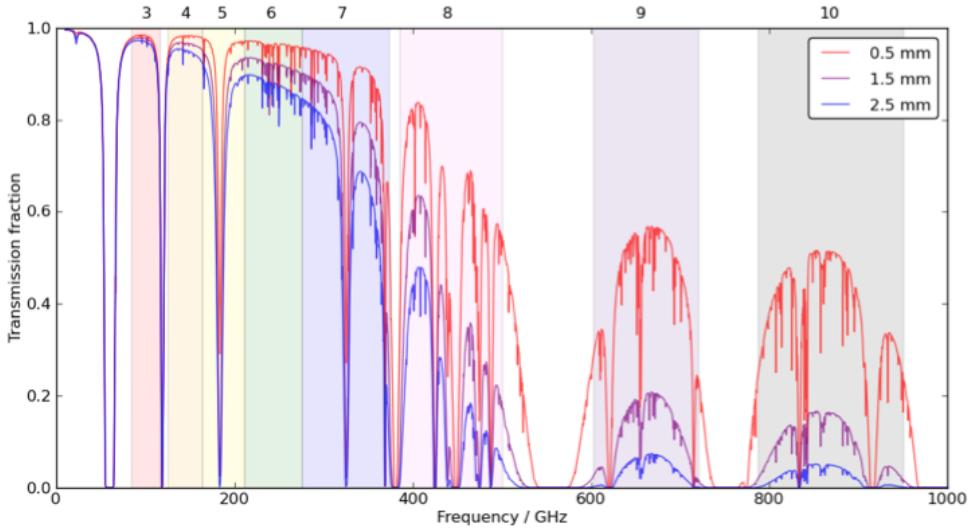

Figure 1.14: Atmospheric transmission for various ALMA bands at Precipitable Water Vapour (PWV) levels of 0.5, 1.5 and 2.5 mm. The atmospheric transmission of Band 3, the data for which has been used in this thesis, is the highest among all the bands in ALMA. Image Credit: ESO/ALMA.

are ideal to achieve very high spatial resolution of ~0.1 arcsec in sub-mm wavelengths which has not been possible before. Current ALMA configurations allow observing from Band 3 to Band 10 spanning a frequency range of 84-950 GHz. The atmospheric transmission is not continuous which is apparent from Fig. 1.14. The presence of these bands allow molecular gas studies for high redshift galaxies using different CO transitions. Chapter 4 presents a comprehensive study of molecular gas properties of AGN host galaxies using Band 3 receiver of ALMA.

1.7 Thesis Overview

The overall aim of this thesis is to find a direct observational evidence of the manifestation of feedback due to radiative winds from AGN located at high redshift. We use dynamical studies of ionized gas and molecular gas content using the tools described in the previous sections. A short synopsis of all the chapters is mentioned as follows:

- **Chapter 2:** This chapter presents IFU observations from SINFONI for AGN host galaxies at high redshift with the aim to trace and characterize ionized outflows using [OIII]λ5007 as tracer. We have pre-selected our targets based on their high mass accretion rates. We derived the mass outflow rates and outflow kinetic powers and compared with the expected power driven by an AGN and star formation to deduce the sources of these outflows. A key highlight of this chapter is the careful PSF analysis and the estimation of large systematic uncertainties in the calculation of outflow power. The entire work has been published as Kakkad et al. (2016)

- **Chapter 3:** In Chapter 3, we present a survey of electron densities in the NLR of nearby Seyfert galaxies using the *Siding Spring Southern Seyfert Spectroscopic Snapshot Survey* (S7). Our main aim is to arrive at a general picture of what processes determine the electron densities in the NLR of AGN host galaxies and construct density profiles in order to bring down systematic uncertainties in the outflow models of AGN discussed in chapter 2.

- **Chapter 4:** In this chapter, a statistical study of the molecular gas properties of high redshift AGN host galaxies has been presented and compared with that of normal star forming galaxies matched in redshift, stellar mass and star formation rate. I show that the AGNs tend to occupy a different parameter space in the observed molecular gas properties compared to the star forming galaxies and that this might be an evidence of radiative AGN feedback at play. The entire work has been published as Kakkad et al. (2017).

- **Chapter 5:** This chapter provides an overall summary of the observations presented in the thesis along with the current and future prospects. I also give a brief overview of an on-going survey for high redshift AGN host galaxies (SUPER) aimed at providing an overall picture of the ISM content and dynamics of the host galaxies.

Chapter 2

Tracing outflows in AGN forbidden region with SINFONI

Published as **D. Kakkad**, *V. Mainieri, P. Padovani, G. Cresci, B. Husemann, S. Carniani, M. Brusa, A. Lamastra, G. Lanzuisi, E. Piconcelli, M. Schramm; A& A, 592, A148 (2016)*

Abstract: AGN driven outflows are invoked in numerical simulations to reproduce several observed properties of local galaxies. The z>1 epoch is of particular interest as it was during this time that the volume averaged star formation and the accretion rate of black holes were maximum. Radiatively driven outflows are therefore believed to be common during this epoch. In this chapter, we aim to trace and characterize outflows in AGN hosts with high mass accretion rates at z>1 using integral field spectroscopy. We obtain spatially-resolved kinematics of the [OIII] λ5007 line in two targets which reveal the morphology and spatial extension of the outflows. The chapter presents J and H+K band SINFONI observations of 5 AGNs at 1.2< z <2.2. To maximize the chance of observing radiatively driven outflows, the sample was pre-selected based on peculiar values of the Eddington ratio and the hydrogen column density of the surrounding interstellar medium. We observe high velocity (∼600-1900 km/s) and kiloparsec scale extended ionized outflows in at least 3 of our targets, using [OIII] λ5007 line kinematics tracing the AGN narrow line region. We estimate the total mass of the outflow, the mass outflow rate, and the kinetic power of the outflows based on theoretical models and report on the uncertainties associated with them. We find mass outflow rates of $\sim 1-10\ M_{\odot}$/yr for the sample presented in this chapter. Based on the high SFRs of the host galaxies, the observed outflow kinetic power and the expected power due to the AGN, we infer that both star formation and

AGN radiation could be the dominant source for the outflows. The outflow models suffer from large uncertainties, hence we call for further detailed observations for an accurate determination of the outflow properties to confirm the exact source of these outflows.

2.1 Introduction

It is a well established fact that most galaxies in the Universe host a super massive black hole (SMBH) in their nucleus (Magorrian et al. 1998; Kormendy et al. 2011). These black holes grow by accretion of surrounding gas and dust (Silk & Rees 1998) and may turn active for a certain period of time ($\sim 10^5$-10^7 yrs) (Martini & Weinberg 2001; Schawinski et al. 2015; King & Nixon 2015). Various galaxy evolutionary models invoke outflows driven by AGN to reproduce several properties of local massive galaxies (Silk & Rees 1998; Granato et al. 2004; Di Matteo et al. 2005b; Croton et al. 2006; Hopkins & Beacom 2006; Menci et al. 2006; Fabian 2012; King & Pounds 2015). Such outflows couple to the surrounding gas and dust and this process, named AGN feedback, is invoked to explain various observed properties such as the black hole and bulge mass relation and the exponential break in the galaxy luminosity function, to name a few (Silk & Mamon 2012; Kormendy & Ho 2013).

The coupling between the outflows and the interstellar medium (ISM) could be in the form of mechanical energy, commonly called jet-mode feedback or radiation energy, called the radiative-mode feedback (see Fabian (2012) and Heckman & Best (2014) for a recent review). Jet-mode feedback occurs in black holes having low mass accretion rates. The outflows from such black holes are in the form of relativistic jets with narrow opening angles launched along the axis of the accretion disc. The impact of such feedback mode has been confirmed through X-ray observations of the centers of galaxy clusters or groups with a radio-loud AGN in their centers (Cavagnolo et al. 2011; David et al. 2011; Nesvadba et al. 2008, 2011). On the other hand, black holes with high mass accretion rates are more likely to drive the radiative feedback mode since these radiative winds are believed to originate from the accretion disc (Granato et al. 2004; Di Matteo et al. 2005b; Menci et al. 2008; Nayakshin 2014). Although there is some observational evidence for the presence of radiative feedback in a few objects (Cano-Díaz et al. 2012; Zakamska et al. 2016b; Cresci et al. 2015a; Perna et al. 2015a; Carniani et al. 2015), we are far from reaching a general conclusion on its impact on the host galaxy.

Outflows have been commonly revealed in local as well as high redshift galaxies using X-ray and UV absorption line studies with velocities reaching >1000 km/s (Crenshaw et al. 1999; Chartas et al. 2002; Ganguly et al. 2007; Piconcelli et al. 2005; Tombesi et al. 2010). Since the radiative mode of feedback should be more relevant at $1 < z < 3$, the epoch of peak volume averaged accretion density of the black holes and the star formation density of the galaxies (Shankar et al. 2009; Madau & Dickinson 2014), there has been an increasing interest to observe galaxies in this redshift range to detect such outflows. In order to quantify their impact on the host galaxy one needs to determine their spatial extension and energetics. Long slit spectroscopy has been widely used to detect such outflows from the presence of broad and extended emission line profiles in the object spectra (Alexander et al. 2010; Harrison et al. 2012; Brusa et al. 2015a). However, one dimensional spectroscopy has the disadvantage that the spatial information and the outflow morphology cannot be inferred from it. Integral field spectroscopy (IFS) is the ideal tool as one can get an idea of both the spatial extension and the morphology of the outflow around the host galaxy in addition to obtaining the total gas content traced by the respective emission lines. In recent years, there has been extensive work on this front using IFS on local as well as high redshift quasars. A few examples of such works are described in brief below.

Harrison et al. (2014) used GMOS-IFU (Gemini Multi Object Spectrograph-Integral Field Unit) observations to spatially resolve ionized gas kinematics in a sample of 16 local radio-quiet luminous Type 2 AGN. They found high velocity and disturbed gas extended over scales of the host galaxies in all of their objects. Though no specific mechanism behind such outflows, i.e. star formation driven or AGN driven, is favored for the sample in general, the most extreme ionized gas velocities seem to be due to the AGN. Husemann et al. (2013) also studied the gas kinematics of a sample of ∼30 low redshift QSOs using Potsdam Multi-Aperture Spectrophotometer (PMAS) where the disturbed gas kinematics is attributed to small scale radio-jet and cloud interactions rather than being AGN-driven. Cano-Díaz et al. (2012) found an extended kiloparsec scale quasar driven outflow for a high redshift Type 1 quasar using SINFONI data. The outflow was asymmetric in morphology and the star formation, traced by the narrow component of Hα line, was mostly found in the regions not directly affected by the strong outflow. This was one of the first direct observational evidence of a negative AGN-feedback. Cresci et al. (2015a) also detected an extended outflow for a high redshift Type 2 quasar. However, in this case, the outflow seems to affect the distribution of star formation in the host galaxy such that star formation is suppressed in the regions dominated by ionized outflows, but enhanced at the edges of the outflow,

making it one of the first observational evidences of both negative and positive feedback at play in a galaxy. Finally, Carniani et al. (2015) studied a sample of six high redshift luminous quasars and found extended kiloparsec scale and high velocity outflows in all their objects. These studies demonstrate the capability of IFS to investigate the impact of AGN on host galaxies, both at high as well as low redshifts. They also suggest that outflows are very common in this redshift range, which should be ideal to study AGN feedback due to radiation pressure driven outflows.

In most of these works, the key diagnostic feature for the presence of kiloparsec scale outflows is the presence of asymmetric [OIII] λ5007 profiles. [OIII] λ4959,5007 are ideal tracers of ionized gas in the NLR as it could not be emitted from the high density sub-parsec scales of the broad line region (BLR). The direction of the outflow can be inferred from the presence of a blue or a red wing in the asymmetric [OIII] λ5007 profile, which indicates gas flow towards or away from the observer respectively. Assuming a bi-conical outflow morphology in most galaxies, it is not uncommon to observe only the blue wing as the red wing is thought to be obscured by dust in the host galaxy.

IFS observations, as the ones listed above, are very expensive in terms of telescope time, and therefore previous studies have always tried to pre-select the targets in order to maximize the chances of observing the AGN in an outflowing phase (Lípari & Terlevich 2006; Brusa et al. 2015a). We have recently completed a SINFONI program at VLT on a sample of five radio quiet Quasi-stellar objects (QSOs) at $1.2 < z < 2.2$. The main goal of this program was to prove the effectiveness of selecting AGN in an outflowing phase based on the peculiar values of the Eddington ratio (which is the ratio of the bolometric luminosity and the Eddington luminosity) or its mass accretion rate and column density of the surrounding interstellar medium. We selected only radio-quiet QSOs since the main goal was to use this selection criterion for studies on the impact of radiative feedback on the host galaxy.

This chapter is arranged as follows: in Sect. 2.2, we present the selection strategy of our sample, in Sect. 2.3, we discuss the observations and the technical details of the data reduction procedure, Sect. 2.4 presents a detailed description of line fitting, creation of kinematic maps and the velocity definitions used in the chapter. In Sect. 2.5, we describe the properties of individual objects derived from the line fitting and the kinematic maps. In Sect. 2.6, we provide details about the formulas used and the assumptions that go into our model while deriving the outflow properties. In Sect. 2.7 we discuss our results and compare them with previous work and finally the conclusions are presented in Sect. 2.8. Throughout

this chapter, we use an $H_o = 70$ km s^{-1}, $\Omega_\Lambda = 0.7$ and $\Omega_M = 0.3$ cosmology.

2.2 Sample selection

As mentioned before, to maximize the chance of observing outflows driven by an AGN, we need to pre-select our objects based on peculiar values of the physical properties of the black hole such as its mass accretion rate or the Eddington ratio and the column density of the surrounding interstellar medium (ISM). Radiatively driven winds are believed to originate from the acceleration of the disk outflows by the AGN radiation field (Begelman 2003). Therefore, our selection criterion is skewed towards objects showing high mass accretion rates or equivalently objects having higher Eddington ratio. An object at higher Eddington ratio, will have a tendency to induce a larger radiation pressure on the surrounding ISM. The additional constraint on the column density is motivated by the impact of the radiation pressure generated by the SMBH on the cold gas responsible for the nuclear obscuration (Fabian et al. 2008). The ISM might be able to withstand the high radiation pressure from the AGN provided it has enough gravitational support, an estimate of which can be obtained from the hydrogen column density measurements. The coupling area between the radiation pressure and that of the surrounding gas is given by the cross section of the particles and in presence of a gas (say a dominant atom like hydrogen), this would be simply the Thomson cross section. However, the ISM consists of both gas and dust grains and in the presence of dust radiation pressure is more efficient due to its higher cross section, thereby lowering the Eddington limit. The effective Eddington limit due to interaction with dust, defined at the balance between radiation pressure and gravity, can be a factor of 1000 lower than the "classical" L_{Edd} for a gas with a Galactic dust-to-gas ratio exposed to a typical quasar spectrum. The result is that long lived clouds would avoid a region of intermediate column densities and high Eddington ratios. Fig. 2.1 shows the possible dividing lines between the objects having long-lived clouds (or in other words, those which are not expected to show outflows) shown by the grey region and those which are expected to be in an active outflowing phase (or the "forbidden region" for long lived clouds), shown by the un-shaded region labeled as "Outflows", adapted from Fabian et al. (2008). The curve labeled "1" in Fig. 2.1 shows the effective Eddington limit for a standard dust abundance for a galaxy while the dashed and dotted lines are for dust abundance of 0.3 and 0.1 of galactic dust abundance respectively.

We looked for objects in this forbidden region from the full XMM-COSMOS

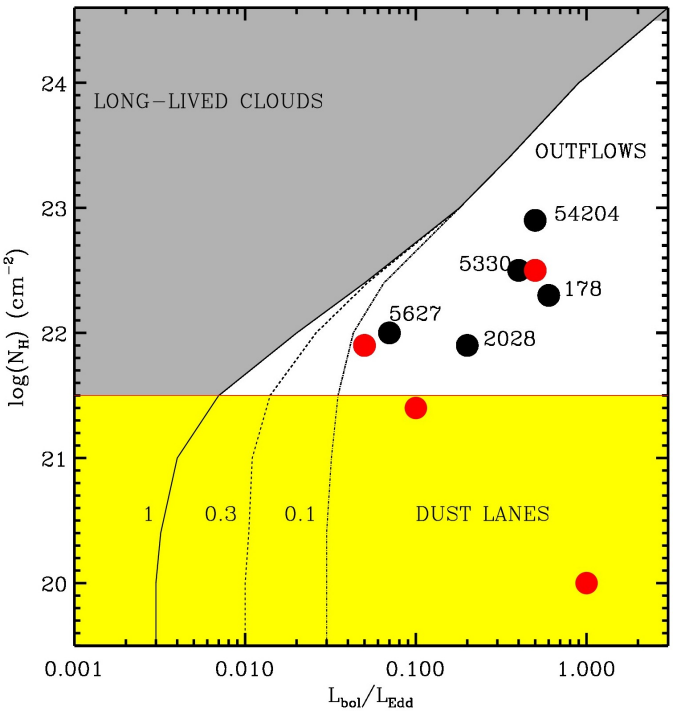

Figure 2.1: Our sample from the COSMOS field in the hydrogen column density, N_H vs. Eddington ratio, $\lambda = L_{bol}/L_{Edd}$ plot, adapted from Fabian et al. (2008). The data points from this work are depicted in black circles, while those in red circles have been obtained from Brusa et al. (2015a) for the objects for which the presence of outflows have been verified (see Sect. 2.7). Various regions of the plot are divided by the expected Eddington limit curves shown in solid, dashed and dotted lines representing galactic dust abundance, 0.3 and 0.1 of the galactic dust abundance respectively. The objects in grey regions are expected to have long lived clouds, while those on the un-shaded region are expected to be in a "blow-out" or an outflowing phase.

catalogue (Scoville et al. 2007; Hasinger et al. 2007; Cappelluti et al. 2009) which consists of ∼1800 AGN from the entire 2 deg^2 COSMOS field, with data having a wavelength coverage from radio to UV, with additional information on the morphology, stellar masses, star formation rate and infrared (IR) luminosities of the host galaxies (Brusa et al. 2010; Salvato et al. 2011; Civano et al. 2012; Bongiorno et al. 2012; Rosario et al. 2012). We restrict our study to objects at z >1 because it is at these redshifts that we expect the radiative feedback to have more significant impact. Our parent sample consisted of 49 objects with z=1.2-2.2, having secure spectroscopic redshifts obtained from ancillary optical spectra, black hole mass and bolometric luminosity measurements (to measure the Eddington ratio, $\lambda = L_{bol}/L_{Edd}$) and reliable column density. The column densities have been derived from detailed X-ray spectral fits (Mainieri et al. 2007; Lanzuisi et al. 2013), the bolometric luminosities have been estimated from SED fitting (Lusso et al. 2011) and the black hole masses from broad MgII lines in the optical spectra (Merloni et al. 2010; Matsuoka et al. 2013) using the virial theorem. Since we want to detect the presence of radiative outflows, we exclude 6 objects which are radio loud with radio-to-optical flux density ratio ($R = \log(S_{1.4GHz}/S_V)$) > 1.4. Of the remaining 43 objects which are radio-quiet, 20 are in the forbidden region. Of these, we followed up the five best candidates in terms of the location of the [OIII] λ4959,5007 emission lines compared to the OH sky emission lines in the infrared spectra. To estimate the stellar mass of the host galaxies, we used an SED fitting technique to model the observed photometry with a galactic and an AGN component (Bonzini et al. 2013). We took advantage of the superb photometry up to the Herschel bands to have a good estimate of the far-infrared (FIR) emission which we used as a tracer of the star-formation (Bonzini et al. 2015). The basic properties of the selected objects are listed in Table 2.1. The results of the analysis of XID2028, one of the objects from our selection sample, were published in Cresci et al. (2015a). In this chapter, we will present some of the information from XID2028 data which were not reported in Cresci et al. (2015a) and the analysis of the rest of the sample from our selection.

Object ID	RA	DEC	z	$\log(L_{bol})$	$\log(m_{bh})$	$\log(N_H)$	M_{acc}	L/L_{edd}	Log M*	SFR
	(h:m:s)	°:′:″		(erg/s)	($M_\odot$)	(cm^{-2})	($M_\odot$/yr)		($M_\odot$)	($M_\odot$/yr)
(1)	(2)	(3)	(4)	(5)	(6)	(7)	(8)	(9)	(10)	(11)
178	10 00 14	02 28 37	1.253	45.7	7.78	22.3	0.8	0.6	10.8	134
5330	09 59 30	02 41 26	2.169	45.9	8.22	22.5	1.2	0.4	10.5	101
5627	09 58 44	01 43 09	1.337	45.7	8.77	22.0	0.8	0.07	10.4	157
54204	09 58 20	02 03 02	1.356	46.1	8.27	22.9	1.7	0.5	10.7	438
2028	10 02 11	01 37 07	1.592	46.3	8.83	21.9	2.8	0.2	11.6	250

Table 2.1: Our sample from the COSMOS field. Column (1): The X-ray ID of the objects; columns (2) and (3): Optical coordinates (J200); Column (4): the spectroscopic redshift of the targets; column (5) Bolometric luminosity from SED fitting; column (6) Black hole mass from broad MgII lines; column (7): column density from X-ray spectral fits; column (8): Mass accretion rate of the black hole; column (9): the Eddington ratio of the black hole; column (10): stellar mass of the host galaxy and column (11): SFR of the host galaxy following the procedure by Bonzini et al. 2015. See Sect. 2.2 for a detailed description of the selection procedure.

Object ID	λ_{narrow}	v_{narrow}	λ_{broad}	v_{broad}	Δv
	(μm)	(km/s)	(μm)	(km/s)	(km/s)
(1)	(2)	(3)	(4)	(5)	(6)
178	1.1310 ± 0.0001	308 ± 4	1.1299 ± 0.0001	1250 ± 130	-275 ± 46
5330	1.5930 ± 0.0001	557 ± 21	-	-	-
5627	1.1766 ± 0.0001	206 ± 66	1.1765 ± 0.0001	537 ± 50	-9 ± 4
54204	1.1810 ± 0.0002	305 ± 71	1.1796 ± 0.0004	1796 ± 882	-359 ± 134
2028*	1.2989 ± 0.0001	366 ± 3	1.2976 ± 0.0001	611 ± 48	-300 ± 50

Table 2.2: [OIII] λ5007 line fitting parameters for the J band integrated spectra of XID178, XID5627, XID54204 and XID2028 and H band spectra of XID5330. Details of the line fitting and the contraints are mentioned in Sect. 2.4. (1) The X-ray ID of our sample; (2) the central wavelength of the narrow Gaussian component of [OIII] λ5007 line; (3) the velocity corresponding to the width (FWHM) of the narrow Gaussian component; (4) the central wavelength of the broad Gaussian component of [OIII] λ5007 line; (5) the velocity corresponding to the width (FWHM) of the broad Gaussian component; (6) velocity offset between the centroids of the narrow and the broad Gaussian components.
*The values for XID2028 reported are from our line fitting results using the two Gaussian components for consistency.

2.3 Observations and data reduction

The aim of our observations is to confirm the presence of outflowing winds in such short-lived objects, and spatially resolve outflows on the scale of the host galaxy i.e. several kpcs. As mentioned before, the key diagnostic feature used to detect outflowing gas is the presence of broad and extended forbidden [OIII] lines at λ = 5006.8 Å. This traces the ionized gas in the NLR, which could be extended up to the scale of the host galaxy.

At the redshift of our objects, the [OIII] λ4959,5007 lines fall in the near-infrared (NIR) and therefore we used SINFONI (Eisenhauer et al. 2003) at the UT4, Very Large Telescope (VLT). Observations were taken between January-March, 2014 as part of the program 092.A-0144 (PI Mainieri). The observations were carried out in seeing limited mode in J band (targets with X-ray ID (XID): XID178, XID5627, XID54204) providing a spectral resolution of 2000 and H+K band (XID5330) providing a spectral resolution of 1500. SINFONI provides rectangular pixels with a spatial scale of 0.125"×0.25", which is re-sampled to a square pixel with a spatial scale of 0.125"×0.125" and a total field of view (FOV) of 8"×8". This means that the gas kinematics can be traced to a spatial scale of few tens of kpc for the entire FOV for galaxies at $z > 1$. In the observations, the object was dithered by 3.5" across the field of view to ensure an optimal sky subtraction during the data reduction process without losing observing time. The total integration time on source for XID178, XID5627 and XID54204 was about 3.5 hours while for XID5330 it was about 50 minutes reaching depths of 9.67, 2.84, 4.96 and 1.29 $\times 10^{-15}$erg s^{-1}cm$^{-2}\mu$m^{-1} respectively. The air mass for all the observation blocks was between X$\sim$ 1.1-1.2 for XID178, X$\sim$ 1.1-1.4 for XID5627, X$\sim$ 1.2-1.4 for XID5330 and X$\sim$ 1.7-2.0 for XID54204. The standard stars for telluric and point spread function (PSF) estimation were observed shortly before and after each observing block with an air mass within 0.2 of that of the science observations.

The data were reduced using the ESO-SINFONI pipeline (version 2.5.2) which corrects for bad pixels and distortions, applies a flat field and performs a wavelength calibration. The final image of the object is reconstructed in the form of 32 slices which contains both the spatial and the spectral information. The raw science frames were first corrected for cosmic ray features using the Laplacian Cosmic Ray Identification procedure (L. A. Cosmic) by van Dokkum (2001) before being fed into the pipeline. The sky subtraction was done externally using the improved procedure proposed by Davies (2007). To remove the infrared sky background, adjacent science frames were used as sky for the object. Two consec-

utive frames are separated by ∼10 minutes, a time interval over which the infrared sky should not change significantly. The final science frames were obtained after correcting for telluric features and flux calibrating the cube using the standard star observed before or after each observing blocks. The header information was used to combine different science cubes within the same observing block while the flux calibrated cubes of different observing blocks were combined by measuring the offset in the centroid emission in a given spectral channel.

2.4 Data analysis

For each of the final science cubes, the integrated spectrum was extracted from a circular region, centered at the object position and with a radius that maximizes the signal-to-noise ratio (S/N) of the [OIII] λ5007 line. Similar to previous studies (e.g. Harrison et al. 2014; Perna et al. 2015a) we performed a simultaneous fit of the continuum, [OIII] λ5007 and [OIII] λ4959 using the IDL routine MPFIT (Markwardt 2012). The Hβ line remained undetected or it was very faint for all our objects. The errors were estimated from the standard deviation of the spectrum extracted from an object-free region of the SINFONI field of view. Eq. 2.1 below shows the mathematical form of the function used for line fitting:

$$f(x) = a \cdot e^{-b \cdot x} + \xi_1(x) + \xi_2(x) \tag{2.1}$$

where the first term corresponds to the local continuum with a and b as free parameters. For fitting the overall [OIII] λ5007 profile, we used either a single or a double Gaussian, the choice of which depended on the S/N of the data and the ability of the components to reproduce the emission line profile. ξ_1 and ξ_2 in Eq. 2.1 correspond to these two Gaussian components - a narrow and a broad component, each with three free parameters defining the central wavelength, width and the flux. The narrow component corresponds to the systemic line which is at rest with respect to the host galaxy, while the broad component(s) would trace the outflowing or the turbulent gas. For all the line profiles, the narrow and broad line widths were constrained. For the narrow Gaussian component, we assume a maximum width (FWHM) of ∼500 km/s corresponding to the rotational velocity of the host galaxy and motion in the NLR while the width of the broad Gaussian was kept greater than 500 km/s to decouple it from the narrow component. When only a single Gaussian was used no constrains on the line width were applied. The line fitting was checked by plotting the residuals of the fit over the [OIII] λ5007 profile. The parameters of [OIII] λ4959 were coupled to those of [OIII] λ5007,

imposing the same velocity dispersion and a flux ratio of $f_{[OIII]5007}/f_{[OIII]4959} \approx 3$ since they are emitted from the same gas (Storey & Zeippen 2000; Dimitrijević et al. 2007). The line fit results of the integrated spectrum for each object are given in Table 2.2 where we list the wavelength (μm) and width (FWHM in km/s) of the individual Gaussian components and the velocity offset between their centroids.

Since we are interested in spatially resolved kinematics, similar line fitting procedure was performed across the entire field of view for each spaxel separately. The robustness of the fitting procedure across each pixel was checked by creating a residual map of the entire [OIII] λ5007 profile. From the results of the spaxel by spaxel fit, we constructed flux maps. Wherever necessary, a re-binning was performed on the cube to improve the S/N across each spaxel. Clearly, this increases the spatial scale of each pixel in the field of view.

Wherever possible, for a better quantitative estimate of the spatial extension of the emission, we created maps for the narrow and the broad components of the [OIII] λ5007 line profile separately, tracing the gas at rest with respect to the system and the outflowing gas. To verify if the emission is extended, we derived the surface brightness profiles of the narrow and the broad components as a function of radius from the peak of the flux weighted mean of the maps. These were compared to the surface brightness profile of the PSF star, which was observed shortly before or after the science observations. We would conclude that the narrow or broad component emission is truly extended if there is an excess in emission of the surface brightness profile compared to the bona-fide point like source represented by the PSF star.

For determining the errors on our measurements, we created 100 mock data cubes by adding Gaussian random noise to the data based on the standard deviation of the spectra extracted from an object free region. The fitting procedure described earlier was repeated for each of these mock cubes (without any constraints on the parameters) and the error associated is the standard deviation of these 100 measurements.

The outflow velocities were estimated from the [OIII] λ5007 in the integrated spectrum of the objects using different prescriptions adopted previously in the literature. Due to the low S/N in each spaxel despite the re-binning procedure, we did not create velocity maps. We used non-parametric analysis of the line profile and refer the reader to Zakamska & Greene (2014); Liu et al. (2013); Rupke & Veilleux (2013) and Perna et al. (2015a) among others for a detailed description of this procedure. The advantages of using a non-parametric measurement is that it does not depend on the details of the fitting procedure and the properties of the individual Gaussian components in the model. After subtracting the continuum

and reproducing the residual line profile, the velocities at different percentiles are evaluated using the cumulative flux function $F(v) = \int_{-\infty}^{v} F_v(v')dv'$, where F_v is the line profile in the velocity space. The zero velocity is taken to be at the peak of the line profile, which is the redshifted wavelength of [OIII] λ5007. The velocity at x percentile, v_x is defined as the velocity at which the cumulative flux function reaches x percent of the overall flux of the asymmetric line profile. Throughout this work, we have calculated v_{10} and $w_{80} = v_{90} - v_{10}$ for the entire [OIII] λ5007 profile on the integrated spectra of the objects i.e. the velocities at the 10th percentile and the width containing 80% of the total flux respectively and v_{10} on the broad-only Gaussian component as estimates of outflow velocity.

These diagnostics have been used in the literature to estimate the outflow velocities and we will compare these values for our targets to estimate the uncertainties affecting such measurements (see Sect. 2.7). Finally, in the kinematic analysis, we assume that the highest velocity is reached in the outermost region of the outflow.

2.5 Results

In the following subsections, we will present the results of the data analysis described above for the individual targets. We refer the reader to Table 2.2 for the results of line fitting for the integrated spectra of each object.

2.5.1 XID178 and XID5627

XID178 and XID5627 are the candidates in our sample (apart from XID2028 which was published in Cresci et al. 2015a) which show definite evidence for the presence of outflow from the [OIII] λ5007 profile. At a redshift of 1.253 and 1.337, both targets were observed using the J grating of SINFONI to sample the [OIII] lines at λ = 4959 Å and 5007 Å. The total exposure time on source was 3.5 hours for each object achieving a S/N ratio of 34 (XID178) and 11 (XID5627) on the integrated spectrum for the [OIII] λ5007 line. Due to the low S/N of the [OIII]λ4959 profile in both targets, the analysis has been restricted to [OIII] λ5007 only. Table 2.2 lists the results of the line fitting procedure described in Sect. 2.4. Figs. 2.2 and 2.3 show the integrated spectrum, the flux maps corresponding to narrow and broad Gaussian components and the surface brightness profiles of XID178 and XID5627 respectively.

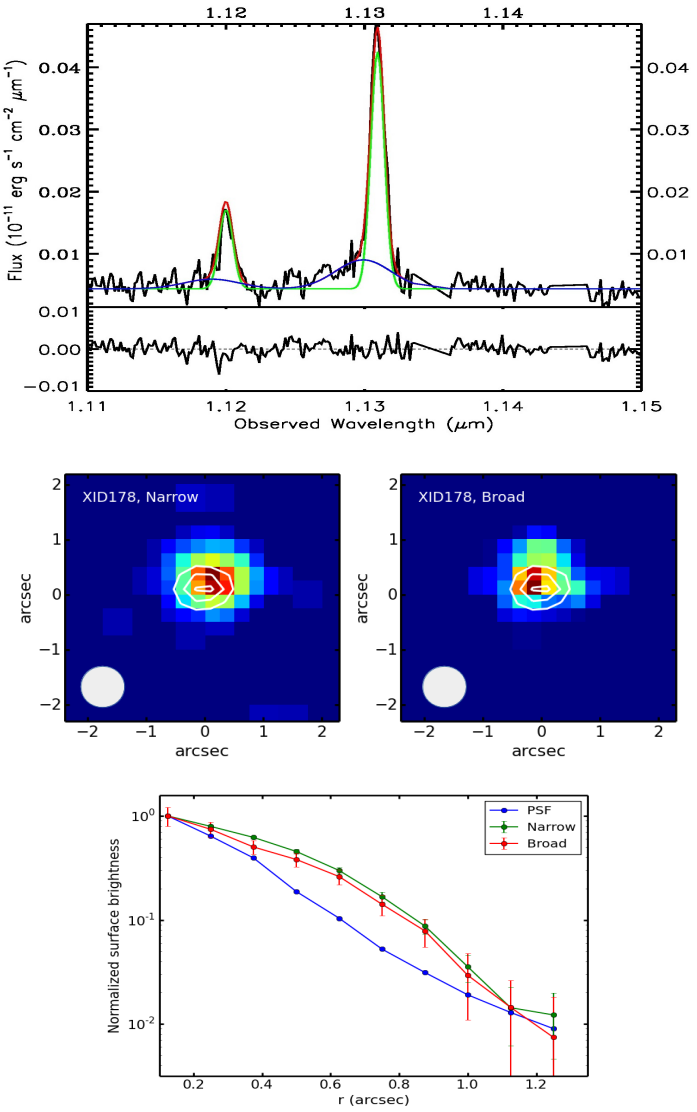

Figure 2.2: *Upper Panel:* The J band spectrum of XID178 around the [OIII] λ4959, 5007 lines extracted from a region of 1.25"×1.25" centered at the QSO position. The observed spectrum is shown in black, the red curve shows the full fit, the green curve shows the narrow line component while the blue curve shows the broad line component. The residuals of the fit are shown in the smaller panel below the integrated spectrum. *Middle panel:* maps of the narrow (left) and broad (right) component in the [OIII] λ5007 profile for XID178. Each pixel corresponds to a spatial scale of 0.25" which at the redshift of this object is equivalent to 2.15 kpc.The white contours in these maps represent the respective continuum emission of the object at levels 50%, 75% and 95%. North is up and East is left. The maps show a one pixel offset between the narrow and the broad components. The gray circle on the lower left shows the size of PSF. *Lower panel:* Surface brightness profiles of the individual Gaussian components in XID178 derived from the flux maps in the middle panel. Green curve denotes the narrow component, red curve the broad component and the blue curve is the PSF of the observations. Both components show an extension up to a distance of 1".

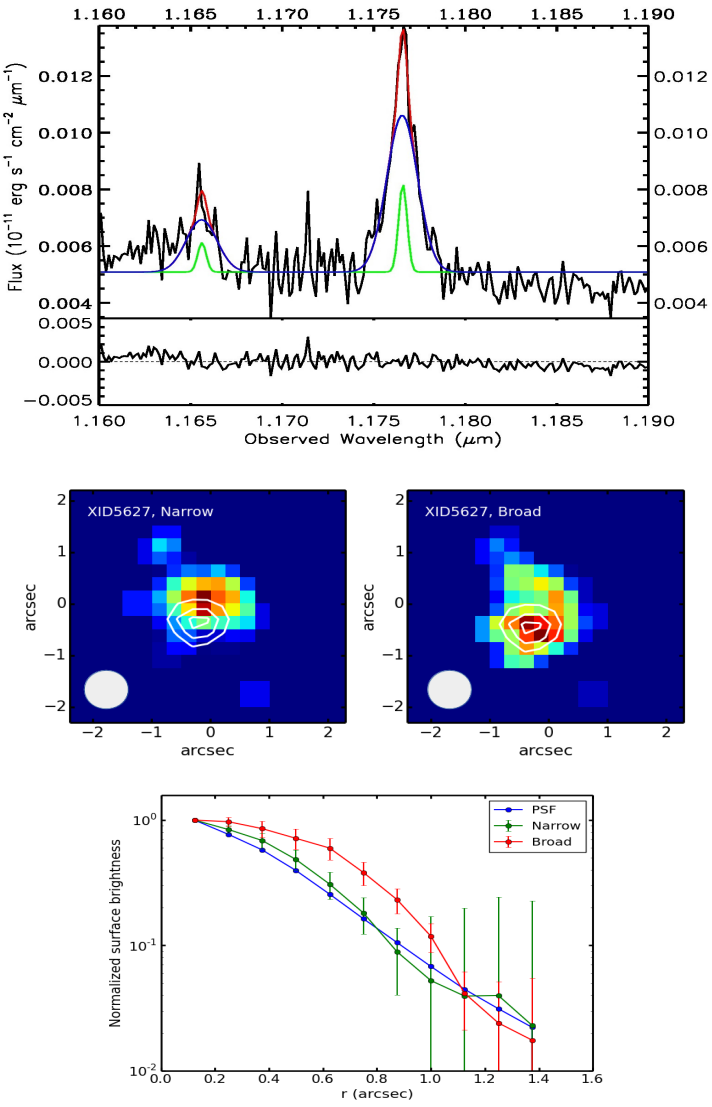

Figure 2.3: *Upper Panel:* The J band spectrum of XID5627 around the [OIII] λ4959, 5007 lines extracted from a region of 1"×1" centered at the QSO position. The color coding for the plot is the same as that of XID178 in Fig. 2.2. The residuals of the fit are shown in the smaller panel below the integrated spectrum. *Middle panel:* maps of the narrow (left) and broad (right) component in the [OIII] λ5007 profile for XID5627. Each pixel corresponds to a spatial scale of 0.25" which at the redshift of this object is equivalent to 2.16 kpc.The white contours in these maps represent the respective continuum emission of the object at levels 50%, 75% and 95%. North is up and East is left. The maps show a significant offset between the spatial locations of narrow and broad emission.The gray circle on the lower left shows the size of PSF. *Lower panel:* Surface brightness profiles of the individual Gaussian components in XID5627 derived from the flux maps in the middle panel. Green curve denotes the narrow component, red curve the broad component and the blue curve is the PSF of the observations. Only the broad component shows an extension. The narrow component is point-like since it is consistent with the profile of the PSF star.

In order to obtain the flux maps and therefore determine the spatial distribution of the outflow, we re-binned the reduced cube by clustering a 2×2 group of pixels into a single pixel for both the targets. This increases the S/N and allows for a better line fitting across the spaxels. As a result, the re-binning procedure increases the spatial scale of the pixel by a factor of 2 to 2.15 kpc and 2.16 kpc for XID178 and XID5627 respectively.

The [OIII] λ5007 profile in the integrated spectrum of XID178 in Fig. 2.2, top panel shows a clear blue wing which traces outflowing gas moving towards us. The velocity offset between the narrow and the broad line Gaussian component is about -275 km/s. The blue wing is not present in the [OIII] λ4959 profile, but we notice that its location coincides with a significant telluric absorption line as can be seen in the residual spectra. Moreover, as mentioned earlier, the [OIII] λ4959 profile has too low a S/N to draw any conclusions about the presence of an outflow. Unfortunately, the presence of a red wing in [OIII] λ5007 cannot be verified since this region of the spectrum is also affected by telluric absorption features as well.

The location of the outflow is apparent from the spatial offset between the narrow and the broad component maps in Fig. 2.2, middle panels. The white contours in the figure represent the location of the continuum emission. The broad emission appears slightly shifted towards east with respect to the continuum as well as the narrow profile. The surface brightness profiles of these individual components in Fig. 2.2, bottom panel confirm that they are extended since there is an excess in the [OIII] λ5007 emission compared to the PSF profile up to 1" ($\sim$ 8.6 kpc).

The integrated spectrum of XID5627 around the [OIII] λ4959,5007 is shown in Fig. 2.3, top panel. The [OIII] λ5007 line profile is nearly symmetric, though two Gaussian components were required to reproduce the overall extended line profile, with a velocity offset of about -9 km/s between the narrow and the broad Gaussian components. The line profile thus suggests that the ionized gas might be moving both towards and away from the observer.

The middle panels of Fig. 2.3 show the map tracing the narrow and the broad components of [OIII] λ5007 profile in XID5627. There is a clear offset between the spatial locations of the narrow and broad component emissions. In addition, the narrow component is point-like since it is consistent with the PSF profile, while the broad component is extended up to a distance of 1" ($\sim$ 8.40 kpc) from the center (Fig. 2.3, bottom panel).

The outflow velocities have been estimated from the integrated spectrum as described in Sect. 2.4. The values from the different prescriptions are tabulated in

	XID178	XID5627	XID5330	XID54204
v_{10}^{a}	-493 ± 27	-247 ± 21	-258 ± 21	-1265 ± 32
w_{80}^{a}	730 ± 60	517 ± 29	659 ± 21	1879 ± 135
v_{10}^{b}	-665 ± 31	-265 ± 28	–	-963 ± 584

Table 2.3: The velocity values derived from the integrated spectrum. v_{10} denotes the 10th percentile velocity value, w_{80} denotes the velocity width containing 80% of the flux.
[a] Derived from the integrated spectra. [b] for broad component only

Table 2.3. The error values are 1σ errors computed by creating 100 mock spectra as described in Sect. 2.4. The velocity values cover the range $\sim 490 - 730$ and $\sim 250 - 520$ km/s for XID178 and XID5627 respectively. Clearly, these ranges of velocities will imply a range in the outflow properties calculated in Sect. 2.6, as discussed in Sect. 2.7.

2.5.2 XID5330

XID5330 has the shortest integration time among the targets of our program. The spectral resolution is lower compared to the rest of the sample since the observations were taken in the SINFONI H+K band. At a redshift of 2.169, the [OIII] line falls in the H band at a wavelength of 1.593 μm and we also detect Hα line at 2.088 μm in the K band. In ~50 minutes, we were able to reach a S/N of 5 for [OIII] λ5007 and 8.3 for Hα in the integrated spectrum.

The integrated H band spectrum around the [OIII] λ4959,5007 lines is shown in Fig. 2.4, top left panel. We have a low S/N ratio for the [OIII] λ5007 profile and hence only one Gaussian has been used for line fitting. Fig. 2.4, top right panel shows the map tracing the narrow component which shows an extension of ~1.1" , which translates to a spatial scale of 9.5 kpc from the centre, when compared to the PSF profile (Fig. 2.4, bottom panel). The absence of a broad Gaussian component coupled with low spectral resolution and low S/N on the spectrum does not allow us to compute mass outflow rates and the associated kinetic power as done for other objects in the sample.

The K band spectrum around the Hα line profile, shows a clear distinction between the narrow and broad Hα components in the spectrum (see Fig. 2.5, left panel). The line fitting parameters for Hα are given in Table 2.4. The broad component of Hα has a velocity dispersion of $\sim$ 6000 km/s and is clearly AGN

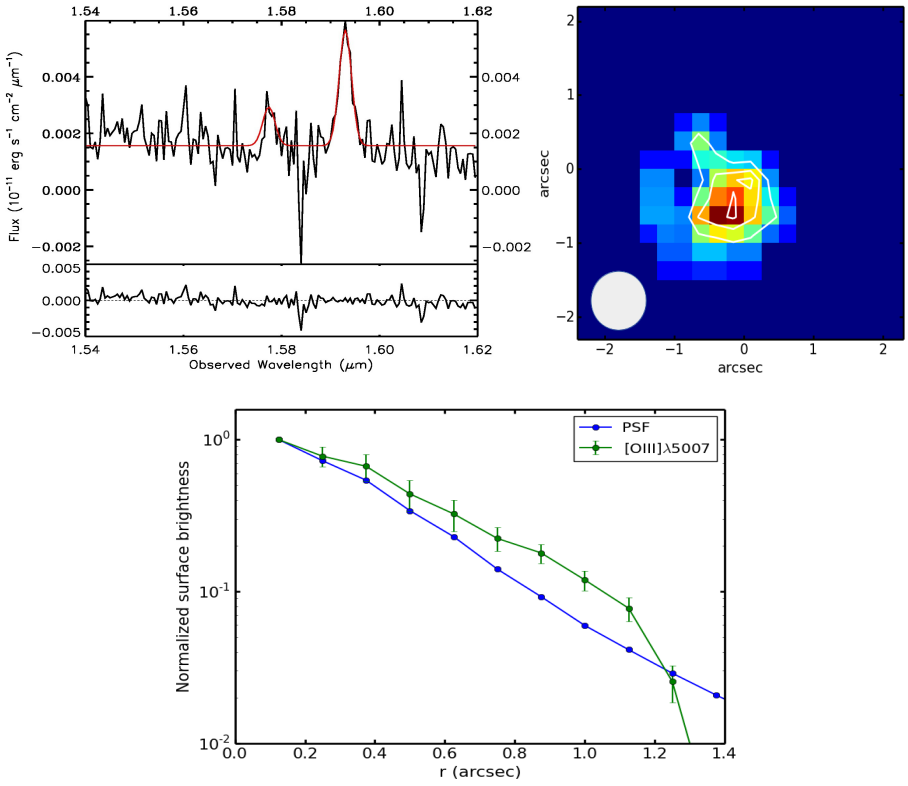

Figure 2.4: *Top left:*The H band spectra of XID5330 around [OIII] λ4959,5007 lines extracted from a region of 1"×1" centered at the QSO position. The observed spectrum in shown in black and the full fit model is shown in red. Due to low S/N on the spectra, only a single Gaussian component was used for line fitting. The lower panel shows the residuals of the line fit. *Top right:* Map tracing the Gaussian component in [OIII] λ5007 profile of XID5330. The white contours show the continuum levels at 50%, 75% and 95%. Each pixel corresponds to a spatial scale of 0.25" (~2.12 kpc). North is up and east is towards left. The gray circle on the lower left shows the size of PSF. *Bottom panel:* The surface brightness profile of the narrow component of the map in the top right panel compared to the PSF profile. The [OIII] λ5007 emission is extended up to 1.1" (~ 9.5 kpc).

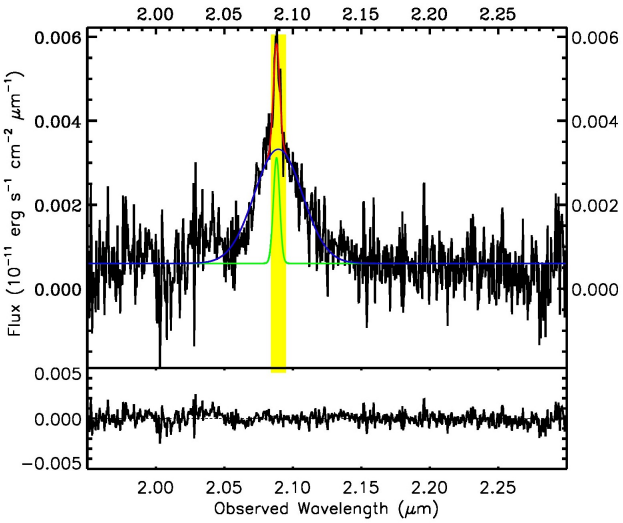

Figure 2.5: The K band spectra of XID5330 around Hα line extracted from a region of 1"×1" centered at the QSO position. There are two distinct components of overall Hα line profile: a narrow component, shown in green and a broad component, shown in blue. The overall fit is shown in red. The lower panel shows the residual of this line fit.

Parameter	Value
$\lambda_{\rm narrow}$	2.0881 ± 0.0005 μm
$v_{\rm narrow}$	770 ± 282 km/s
$\lambda_{\rm broad}$	2.0894 ± 0.0005 μm
$v_{\rm broad}$	5950 ± 808 km/s

Table 2.4: Line fitting parameters for K band spectra of XID5330. Two components, narrow and broad Gaussian were used to fit the entire Hα profile. $\lambda_{\rm narrow}$ = central wavelength of the narrow Gaussian component; $v_{\rm narrow}$ = velocity corresponding to the FWHM of the broad Gaussian; $\lambda_{\rm narrow}$= central wavelength of the broad Gaussian component and $v_{\rm broad}$ = velocity corresponding to the FWHM of the broad Gaussian component. The wavelength of the broad component is redshifted by 190 km/s with respect to the narrow component.

related. The velocity offset between the narrow and the broad Gaussian components is about +190 km/s (the broad component is redshifted with respect to the narrow component). The low S/N of the spectra does not allow us to disentangle contributions (if any) to the flux from [NII]λ6549,85 lines which are expected to lie at 2.0837μm and 2.0951μm respectively i.e. on either side of the narrow Hα component.

The presence of the broad Hα line gives us the possibility to estimate and verify the mass of the black hole. We use the Greene & Ho (2005) formalism wherein the black hole mass from the Hα line is given by:

$$m_{bh}^{H\alpha} = 2.0 \times 10^6 \left(\frac{L_{H\alpha}}{10^{42}\ \mathrm{erg\ s^{-1}}} \right)^{0.55} \left(\frac{FWHM_{H\alpha}}{1000\ \mathrm{km\ s^{-1}}} \right)^{2.06} M_\odot \qquad (2.2)$$

We consider only the broad line component of the flux of the Hα profile for the estimation of luminosity, which comes out to be $2.7 \pm 1.0 \times 10^{43}$ erg/s. Using the values from Table 2.4 and the luminosity of the broad component, we arrive at a black hole mass of $8.9 \pm 0.2 \times 10^8$ $M_\odot$. This is a factor of ~5 larger than the value given in Table 2.1, which is based on broad MgII line. This discrepancy might be due to the low S/N in both optical as well as H+K band data. Moreover, we are unable to disentangle the contribution due to [NII]λ6549,85 on the entire Hα profile which, if present, could bring down our mass estimate.

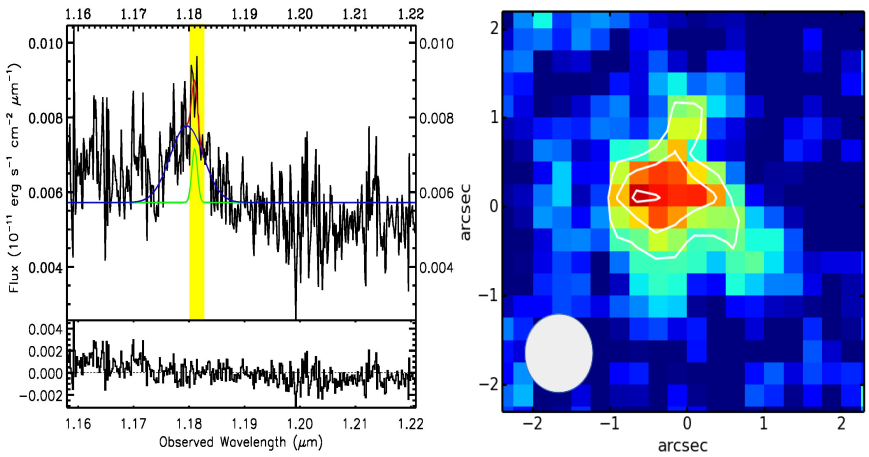

Figure 2.6: *Left panel:* The J band spectrum of XID54204 around [OIII] λ5007 line extracted from a region of 1"×1" centred at the QSO position. The color codes for different part of the spectra are defined in the same way as Fig. 2.2, top panel. *Right Panel:* Continuum collapsed channel map around the narrow component of [OIII] λ5007 line (yellow region in the left panel, 1.180-1.182 μm). Each pixel corresponds to a spatial scale of 0.25" which at the redshift of this object is equivalent to ∼2.16 kpc. The white contours indicate the peak of the [OIII] λ5007 emission at levels 50%, 75% and 95%. North is up and East is towards left. The gray circle on the lower left shows the size of PSF.

2.5.3 XID54204

XID54204 has a very faint [OIII] λ5007 signal despite an integration time of 3.5 hours on the target. The [OIII] λ5007 line is detected at a wavelength of 1.1796 μm consistent with the object being at z=1.356. A S/N of 4.4 could be reached in the integrated spectrum of the [OIII] λ5007 emission line.

Although faint, the [OIII] λ5007 profile in the integrated spectrum is quite broad, so a single Gaussian is not able to provide a good fit of the line profile. Therefore we added a second component and the resulting integrated spectrum is given in Fig. 2.6, left panel. The integrated spectrum indicates the presence of a blue wing in the [OIII] λ5007 profile, hence the outflow direction is towards the observer. The velocity offset between the narrow and the (blue-shifted) broad Gaussian component is ~360 km/s.

Fig. 2.6, right panel shows the continuum subtracted [OIII] λ5007 line core map, confirming [OIII] emission from this object. The line core map was obtained by integrating the continuum collapsed SINFONI data cube between 1.180-1.182 μm, shown by the yellow region in the integrated spectrum in Fig. 2.6. Due to low S/N in each spaxel, one cannot do line fitting across the FOV and consequently we could not obtain surface brightness profiles as we did for other objects. In this case, one can only put an upper limit of the spatial extension of the outflow from the FWHM of the PSF, which is 0.8" (~ 6.9 kpc). The outflow velocity from the integrated spectrum have been estimated in the range ~950-1900 km/s (see Table 2.3).

2.6 Outflow properties

The determination of the properties of the outflow such as its mass is complicated by the fact that the outflow has a multi-phase nature. While we are tracing the outflow in its warm ionized phase using the [OIII] λ5007 line, a significant fraction of the outflows are believed to be in the cold molecular gas phase (Veilleux et al. 2013; Cicone et al. 2014; Feruglio et al. 2015; Brusa et al. 2015b; Nyland et al. 2013). There are many papers in the literature which discuss the estimation of the mass of the ionized outflows from either Hβ or [OIII] λ5007 (e.g., Holt et al. 2011; Cano-Díaz et al. 2012; Liu et al. 2013; Harrison et al. 2014). Due to the limited information available to us (e.g., lack of Balmer lines), we derive the outflow gas mass from the [OIII] λ5007 line based on Cano-Díaz et al. (2012). [OIII] lines are very sensitive to temperature and ionization but poor tracers of mass, hence

the current analysis only provides (at best) an order-of-magnitude estimate of the outflow properties.

Below, we summarize the essential formulas used to arrive at the outflow properties and the assumptions associated with them. The mass of the ionized outflowing gas is given by:

$$M_{ion}^{out} \approx 5.33 \times 10^8 \left(\frac{C}{10^{[O/H]-[O/H]_\odot}}\right)\left(\frac{L[OIII]}{10^{44}\ \mathrm{erg\ s^{-1}}}\right)\left\langle\frac{n_e}{100\ \mathrm{cm^{-3}}}\right\rangle^{-1} M_\odot \qquad (2.3)$$

where C ($= < n_e >^2 / < n_e^2 >$) ~ 1 based on the hypothesis that all the ionizing gas clouds have the same density, L[OIII] is the luminosity of the [OIII] λ5007 line tracing the outflow, n_e is the electron density of the outflowing gas and $10^{[O/H]-[O/H]_\odot}$ represents the oxygen abundance in Solar units. The luminosity of [OIII] λ5007 is derived from the flux of the broad line component in the integrated spectrum, when present. In the absence of a broad component, mass estimate of the outflowing gas could not be obtained. The normalization factor in Eq. 2.3 is dependent on the emissivity of the ionized gas which is further dependent on electron density and the temperature of the gas. The emissivity calculations were done using PyNeb (Luridiana et al. 2015). The following assumptions go into Eq. 2.3:

- Most of the oxygen in the outflow is in its ionized form, O^{+2} i.e. $n(O^{+2}) \approx n(O)$.
- The number density of atomic helium is 10% that of atomic hydrogen i.e. $n(He) \approx 0.1\ n(H)$. This is based on the "cosmic composition" from abundance measurements in the Sun, meteorites and other disk stars in the Milky Way (Ferrière 2001).
- The electron density, n_e is assumed to be equal to 100 cm^{-3}. The electron density is usually measured using the line ratio of the [SII] λ6716,31 doublet (Peterson 1997). As a recent example of this technique, Perna et al. (2015a) estimate $n_e \approx 120$ cm^{-3} from the [SII] doublet in the outflow component for a high S/N target XID5321 in the COSMOS field which is within the typical value estimates of electron density for the NLR ($\lesssim 50 - 1500$ cm^{-3}). Previous works also use a value within this range when the electron density is not known. For example, Cano-Díaz et al. (2012) use a value of 1000 cm^{-3}, while Cresci et al. (2015a) and Liu et al. (2013) assume a value of 100 cm^{-3} and Harrison et al. (2014) and Carniani et al. (2015) use a value

of 500 cm^{-3}. We have taken these differences into account while comparing the outflow rates we derive to the previous works in Sect. 2.7. We also discuss the level of uncertainties due to these assumptions.

- Emission lines from a single ion having different excitation potentials are highly temperature dependent which makes them suitable for electron temperature measurement in the NLR Peterson. As mentioned before, the normalization factor in Eq. 2.3 depends on the emissivity of the ionized gas which is sensitive to temperature changes. Hence the normalization factor in Eq. 2.3 will change with the assumed temperature. Usually, [OIII] λ4363,4959,5007 or [NII]λ5755,6548,6583 are the set of lines used for this purpose. Typical temperatures measured for the NLR using this method come out to be about 10,000-25,000 K. For our calculations, we assume a value of 10,000 K.

- Since the current data do not allow us to determine oxygen abundances, solar metallicity values have been used.

Due to the limited information available to us about the morphology of the outflow, we assume a simple conical outflow model[1] for our objects. The volume averaged density of the outflowing gas, $< \rho_{\rm out} >$ (not to be confused with the gas density of individual clouds) is given by:

$$< \rho_{out} >= 3\frac{M_{out}}{\Omega \cdot R_{out}^3} \tag{2.4}$$

where Ω is the solid angle subtended by the (bi)-conical outflow and $R_{\rm out}$ is the extension of the outflow in the cone. The mass outflow rate is then given by $\dot{M}_{\rm out} \approx < \rho_{\rm out} >_{\rm v} \cdot \Omega R_{\rm out}^2 \cdot v_{\rm out}$. When combined with Eq. 2.3, this gives:

$$\begin{aligned} \dot{M}_{ion}^{out} \approx 1.64 \times 10^3 \cdot \left(\frac{1}{10^{[O/H]-[O/H]_\odot} R_{kpc}}\right)\left(\frac{L[OIII]}{10^{44}\ \mathrm{erg\ s^{-1}}}\right) \\ \left(\frac{v}{1000\ \mathrm{km\ s^{-1}}}\right)\left\langle\frac{n_e}{100\ \mathrm{cm^{-3}}}\right\rangle^{-1} M_\odot/yr \end{aligned} \tag{2.5}$$

where v is the velocity of the outflowing gas (from Table 2.3) out to a radius $R_{\rm kpc}$ in units of kiloparSect. The kinetic energy of the outflow due to the ionized component is simply $1/2\ \dot{M}_{\rm out}^{\rm ion} v^2$:

[1] It might actually be a bi-conical outflow morphology, but since we observe only one side of the outflow we only take into account this part in our calculations.

$$\dot{E}_K^{ion} = 5.17 \times 10^{44} \cdot \frac{1}{10^{[O/H]-[O/H]_\odot} R_{\rm kpc}} \left(\frac{L[OIII]}{10^{44}\ {\rm erg\ s^{-1}}} \right) \cdot \left(\frac{v}{1000\ {\rm km\ s^{-1}}} \right)^3 \left\langle \frac{n_e}{100\ {\rm cm^{-3}}} \right\rangle^{-1} {\rm erg\ s^{-1}} \tag{2.6}$$

If the distance of the outflowing region is known from the maps, we can also compute the dynamical time scale of the outflow:

$$t_d \approx R_{out}/v_{out} \tag{2.7}$$

where v_{out} is the outflow velocity inferred from the kinematic analysis. The dynamical time scales could give us an idea about the "on" phase of the outflow, which, whenever possible to calculate, would be a direct observational constraint on the time scales of the outflow driven by an AGN at high redshift. The outflow properties mentioned in this section have been derived for every object in our sample and are reported in Table 2.5. The Table indicates a range of these properties obtained using the velocity ranges in Table 2.3, keeping other assumptions such as the electron density, temperature, radius and metallicity constant. The errors on these properties have been ignored compared to the systematic uncertainties.

Object ID	$f_{[OIII]}$ (10^{-16} erg/s/cm^{-2})	$\log(L_{[OIII]})$ (erg/s)	M^{ion}_{out} (10^7 $M_\odot$)	$\dot{M}^{ion}_{out}$ ($M_\odot$/yr)	$\dot{E}^{ion}_{K}$ (10^{41} erg/s)	P_{SFR} (10^{43} erg/s)
(1)	(2)	(3)	(4)	(5)	(6)	(7)
178	2.33 ± 0.16	42.35 ± 0.02	1.13	2.00-2.96	1.53-4.98	9.4
5330*	1.29 ± 0.04	42.68 ± 0.01	–	–	–	7.0
5627	1.65 ± 0.15	42.27 ± 0.02	0.94	0.83-1.74	0.16-1.46	11.0
54204	1.54 ± 0.84	42.26 ± 0.05	0.91	3.91-7.63	11.44-84.95	30.7
2028†	2.64 ± 0.09	42.66 ± 0.01	2.32	8.24	58.44	17.5

Table 2.5: Outflow properties derived from the line fits and the formulas mentioned in Sect. 2.6. (1) The X-ray ID of the sample; (2) Flux of the broad Gaussian component in the [OIII] λ5007 profile; (3) luminosity corresponding the flux in (2); (4) is the outflow mass traced by the [OIII] λ5007 line, (5) & (6) are the range in mass outflow rates and the kinetic energy associated with the ionized component corresponding to the velocity values in Table 2.3, keeping the rest of the assumptions constant; (7) Power due to the star formation in the host galaxy.
*Mentioned values for XID5330 are for the overall line profile.
†Values reported are from [OIII] λ5007 analysis from this work to be consistent while comparing with other objects.

2.7 Discussion

2.7.1 Outflow detection and selection efficiency

At least three of the four targets (XID178, XID5627 and XID54204) presented in this chapter show clear evidence of outflows. The S/N ratio of XID54204 is very low so the spatial information of the outflow could not be derived, although there is an indication of the presence of a blue wing in its [OIII] λ5007 profile in the integrated spectrum. The low S/N of XID54204 could be simply due to the high air mass through which this object was observed (see Sect. 2.3). Due to the low integration time of XID5330 coupled with a lower spectral resolution in the H+K band of the SINFONI grating, we were not able to reach the S/N ratio limit for which we could observe the wings in the [OIII] λ5007 profile. Including XID2028 (Cresci et al. 2015a) which also satisfies the selection criterion of our sample, we can say that Fig. 2.1 is an effective tool to select AGN in an outflowing phase. Our study reinforces previous evidence for absorption variability in the X-ray spectra of AGN close to the forbidden region (Vasudevan et al. 2013). In order to populate this plane with other known outflows, we have added in Fig. 2.1 the sample from Brusa et al. (2015a) for which we have the hydrogen column density and Eddington ratio estimates (red circles). We see that three out of the four objects of that sample lie inside or very close to the forbidden region which further points to the efficiency of this selection procedure.

Previous studies on AGN outflows have been biased in pre-selected targets with higher chances to be in an outflowing phase, similar to what we did. As an example, the Brusa et al. (2015a) selection was based on the fact that the QSOs in an outflowing phase are expected to be dusty and reddened, the so-called "red QSOs". This is shown by the red circles in Fig. 2.7 which shows a plot between the X-ray (2-10 keV) to optical flux ratio (X/O) and R-K (Vega) colors. Three of our targets (marked by blue stars) lie in the blue QSO region (R-K $\sim$ 2). XID54204 is not included in this figure as it is not detected in the 2-10 keV band. XID2028 is the blue star in the red QSO region. We are therefore exploring a completely different region of the X/O vs. R-K plot and we find that the objects in the blue region also show outflows. Clearly the next step would be to test these selection criteria with a blind sample which covers the whole plane in Fig. 2.7 (and Fig. 2.1).

The one dimensional spectra of three of the objects from our sample (XID2028, XID5627 and XID54204 a.k.a XCOS2028, XCOS5627 and COS178 respectively) have also been presented in Harrison et al. (2016) as part of the KMOS AGN sur-

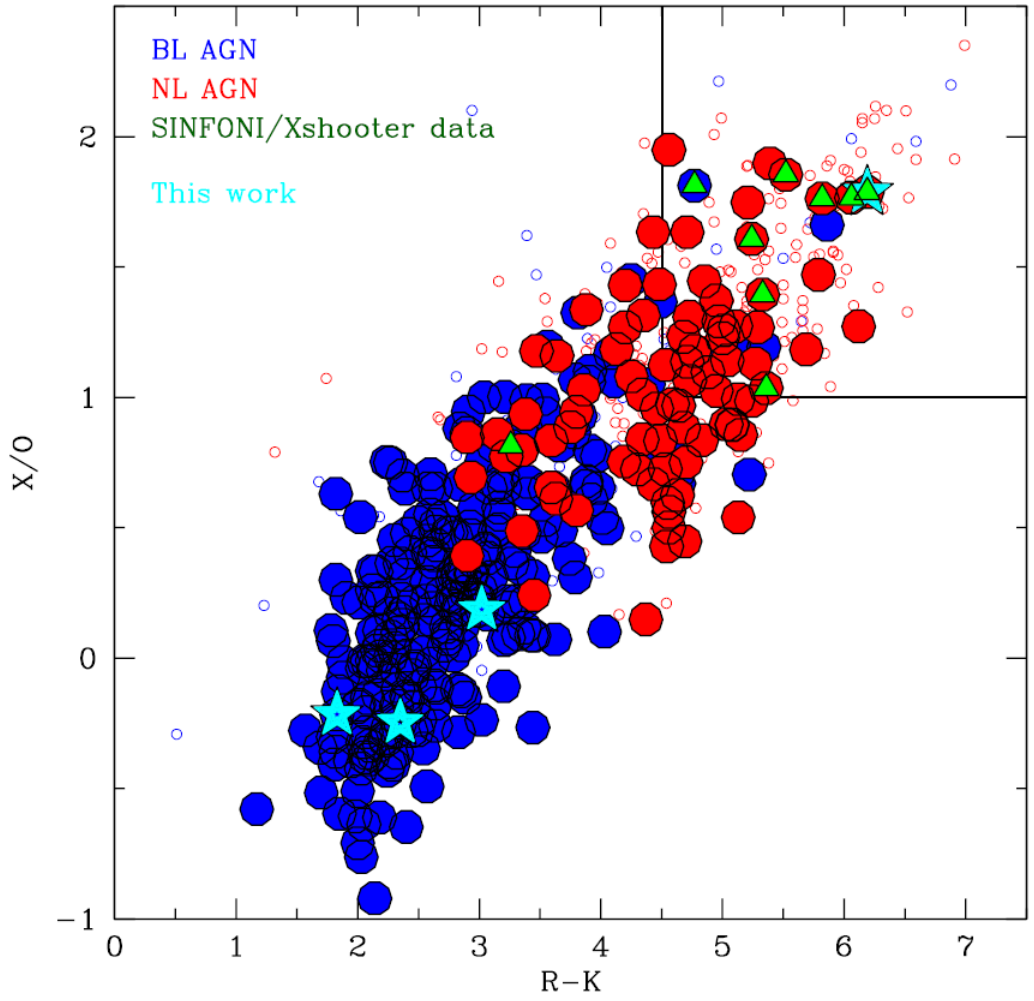

Figure 2.7: X-ray to optical flux ratio (X/O) vs. R-K (Vega) color magnitude plot. Open circles represent all the data points from the XMM-COSMOS survey, red and blue filled circles represent the spectroscopically confirmed narrow line and broad line AGNs respectively. In green are the AGN with detected outflows published in Brusa et al. (2015a); Perna et al. (2015b). Data points in starred cyan represent the objects from this chapter. Clearly, with our sample, we are exploring a different region of the plane.

vey at High Redshift (KASHz). Except for XID54204, our one dimensional results (line wavelengths, widths and luminosity) are compatible with those reported by Harrison et al. (2016). The minor differences might be due to the different apertures used for spectral extraction from the IFU cube and the errors associated with the flux calibration. Harrison et al. (2016) do not detect any [OIII] λ5007 in their analysis for XID54204 (COS178). We were able to detect the presence of the faint [OIII] λ5007 signal by constructing a continuum subtracted channel map over the narrow component of the line as given in Fig. 2.6.

2.7.2 Source of the outflows

In order to understand the nature of ionized outflows, we need to estimate the total mass of the outflowing gas, the mass outflow rate and the kinetic power driven by the AGN using the formulas given in Sect. 2.6. As mentioned in Sect. 2.6, we explore a range of outflow properties depending on the velocity measurements. Tight correlations are expected between these quantities and the bolometric luminosity of the AGN according to theoretical models which also predict high velocity outflows from AGN (King et al. 2011; Zubovas & King 2012). These models predict outflow velocities in the range 1000 – 1500 km/s and mass outflow rates up to 4000 $M_{\odot}$/yr which are extended to kiloparsec scales. XID2028 shows outflow velocities up to 1500 km/s extended up to 13 kpc from the central object with the total mass outflow rate expected to be at least 1000 $M_{\odot}$/yr (Cresci et al. 2015a). Such high velocities could not be sustained by star formation alone and a more powerful source such as an AGN is required. This is also the case for XID54204 where we observe linewidths with velocity exceeding 1000 km/s. XID178 and XID5627 also show outflows which are spatially extended up to $\sim$ 8.6 kpc. Compared to XID2028 and XID54204, these objects have lower outflow velocities up to $\sim$700 km/s. However, these are projected velocities and depending on the inclination of these systems, the actual velocities may be higher than the reported values. Nevertheless, these velocities are compatible with star-formation processes.

Figure 2.8: 3”×3” HST-ACS images of the sample presented in this chapter, with a spatial scale of 3”×3” for each object. For XID178 and XID5627, the white contours represent the narrow component of the [OIII] λ5007 emission line profile while the yellow contours represent the broad component while for XID5330, the white contours represent the single Gaussian component of [OIII] λ5007. All contours are at levels 50%, 75% and 95%. The SINFONI data are not corrected for astrometry.

We looked at the HST images for these objects, and the cutouts are shown in Fig. 2.8. All images have a spatial scale of 3″×3″ which is comparable to the flux and velocity maps presented in Sect. 2.5. None of these images show any disturbed morphology that could hint to a recent merger, therefore we may disfavor the idea that the dynamical signatures interpreted as outflows are actually due to mergers. The white contours in Fig. 2.8 represent the narrow [OIII] λ5007 emission for XID178, XID5330 and XID5627 while the yellow contours represent the broad component. It is clear from the figure that the ionized emission traces a larger fraction of the total gas in the host galaxy compared to the optical images.

Based on the SFRs of the host galaxies of our sample of QSOs, we can also derive the kinetic power driven by supernovae and stellar winds and compare it to the outflow power we obtain to identify the possible source for such outflows. The power driven due to these stellar processes can be calculated using Veilleux et al. (2005) formalism:

$$P_{SF} = 7 \cdot 10^{41} \times SFR \ \mathrm{M}_{\odot}/\mathrm{yr} \tag{2.8}$$

The power due to star formation for each of our targets are listed in column 7 of Table 2.5 and can be compared with the kinetic power of the outflow due to the ionized gas component given in column 6 of the same table. For XID2028, Cresci et al. (2015a) reported a value of $\sim 1.5 \times 10^{44}$ erg/s for the kinetic energy due to the ionized gas as traced by the Hβ line, while we obtain $\sim 5.8 \times 10^{42}$erg/s from the [OIII] λ5007. The apparent discrepancy of a factor of 25 shows the difficulty of using [OIII] lines as tracer of the outflow mass as explained in Sect. 2.6. For reference, we use both the values we obtain using [OIII] λ5007 and that obtained by Cresci et al. (2015a) using Hβ in the plots to follow to demonstrate the differences in power estimates from the two lines. Note that all the mass outflow rates reported in Table 2.5 are lower limits because additional gas phases are missing.

In Fig. 2.9 we compare the outflow kinetic power with the predicted energy input rate from star formation following Veilleux et al. (2005) for our sample and other previous studies (Harrison et al. 2014; Brusa et al. 2015a; Cresci et al. 2015a). The outflow kinetic energy was recomputed for each work from the literature to be consistent with our assumption of electron density (100/cm^3) and temperature (10,000 K). The solid, dashed and dotted lines represent 100%, 5% and 0.1% ratios, respectively. For the two newly detected outflows (XID178 and XID5627, red stars in the figure) having > 0.1% coupling between the stellar energy input and the ISM is sufficient to make star-formation viable as a dominant

power source for the observed outflows. For XID54204, star formation itself could not sustain the observed high velocities and kinetic power (King et al. 2011).

In Fig. 2.10 the outflow kinetic energy is plotted against the AGN bolometric luminosity. We included in the figure other known ionized (Greene et al. 2012; Harrison et al. 2014; Carniani et al. 2015; Brusa et al. 2015a; Cresci et al. 2015a) and molecular (squares, Cicone et al. 2014; Sun et al. 2014; Feruglio et al. 2015) outflows. The dotted, dashed and the solid lines represent the fraction of AGN bolometric luminosity in the form of the outflow power (0.1%, 5% and 100% respectively). Two of the objects presented in this work (XID178 and XID5627, red stars at lower bolometric luminosity) lie at the low energy end of the distribution of previously reported ionized outflows, while XID54204 (red stars at a higher bolometric luminosity) falls in the regime of previously known ionized outflows. Theoretical models predict a coupling of ∼0.1-5% for AGN-driven outflows (King 2005), and for these three objects a coupling less than 0.1% of the radiative power of the AGN with the ISM might be sufficient to power the detected outflows. It is important to note that due to the multi-phase nature of the outflows, our kinetic energy estimates are lower limit, since one should consider the total mass of the outflow in the form of ionized, molecular and neutral gas. This is supported by the fact that the previously reported molecular outflows fall into a regime with higher coupling (∼5%) between the outflow kinetic energy and energy released by the AGN. The exact conversion factor to go from ionized to the total gas mass is not known and might vary on an object-by-object basis. Clearly follow-up observations at mm wavelengths are needed to have a more complete picture.

Knowing the radius of the outflow for XID178 and XID5627 to be ∼8.6 kpc from the surface brightness profiles in Figs. 2.2 and 2.3, the dynamical time scale of the outflow calculated from Eq. 2.7 comes out to be ≈ 18 Myr for both targets. This value is similar to previously reported outflow timescales and AGN lifetimes (e.g. Cresci et al. 2015a; Greene et al. 2012; Martini & Weinberg 2001). This exercise could not be performed for XID54204 as we do not have the spatial resolution to determine the size of the outflow.

In summary both star-formation processes and AGN radiation could be the dominant power source for the outflows presented in this chapter. Although, the observed high kinetic power for XID54204 points to an AGN driven outflow, a higher S/N and better spatial resolution data is required to confirm this.

The outflow momentum rate, defined as $v_o\dot{M}_o$, is another fundamental parameter of the outflow which is crucial to understand if it is momentum or energy conserving (Zubovas & King 2012; Faucher-Giguère & Quataert 2012). Theoretical models predict that the momentum of the kpc-scale outflow is boosted by

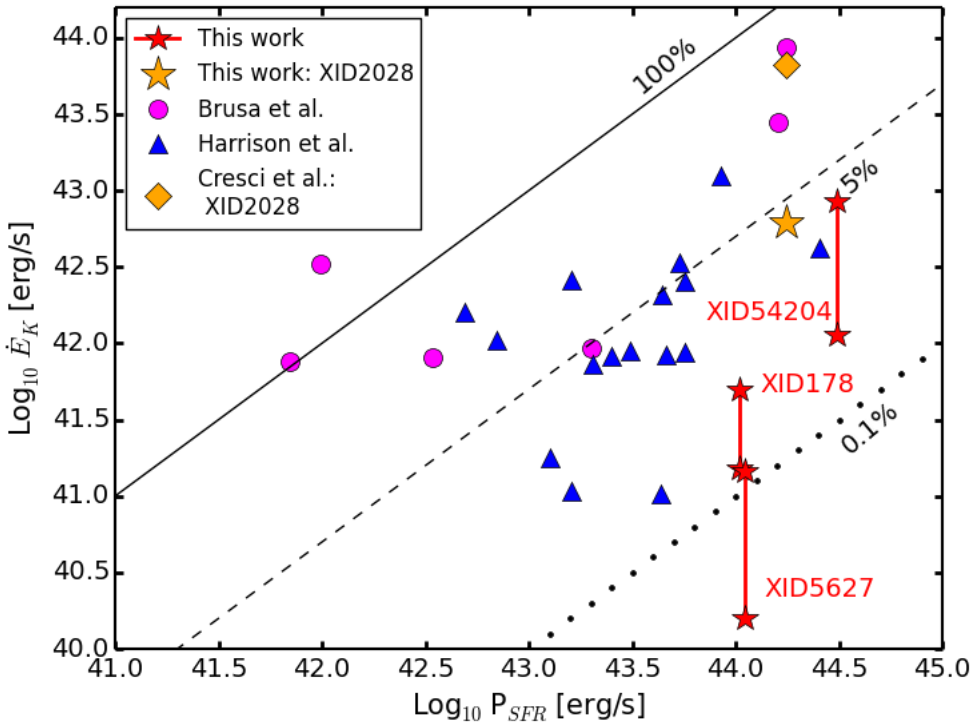

Figure 2.9: Kinetic outflow power, $\dot{E}_K$ vs. the power driven by star formation, P_{SFR}. The solid, dashed and dotted lines represent 100%, 5% and 0.1% ratios between the two powers. Our sample is represented by the star symbols while the other data points have been obtained from Brusa et al. (2015a); Cresci et al. (2015a) and Harrison et al. (2014). All data points represent outflow powers due to the ionized gas calculated from [OIII] λ5007 line, except the data point from (XID2028: Cresci et al. 2015a) which represents one of the objects from our selection and whose outflow properties were reported using Hβ line. The two points for XID2028 show the differences in power estimates from the two emission lines. The range of kinetic power from our sample is due to the different prescriptions used to derive the outflow velocity.

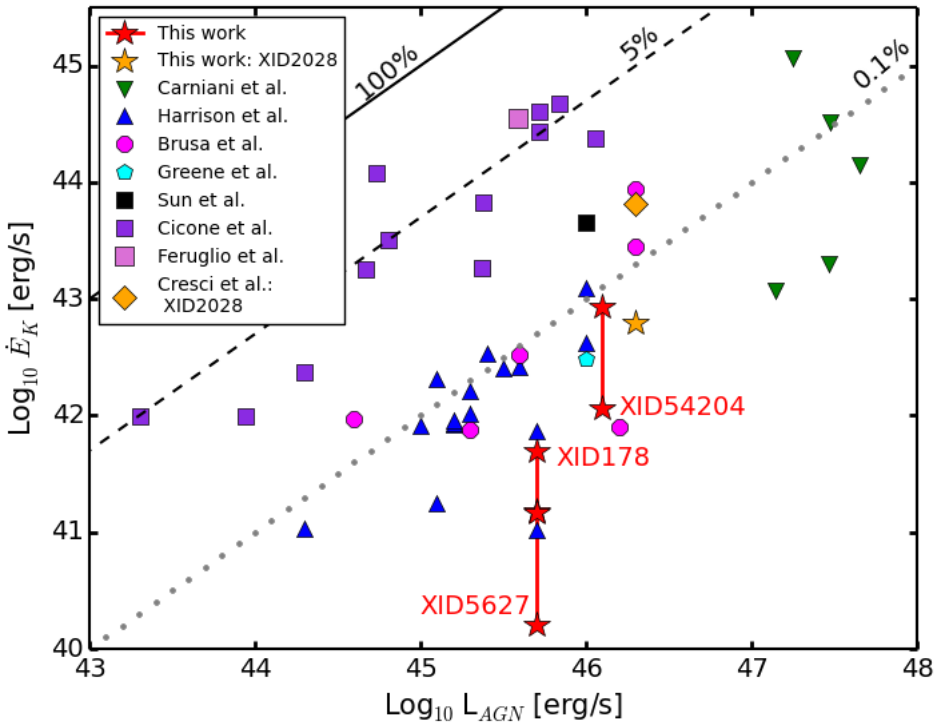

Figure 2.10: Kinetic outflow power, $\dot{E}_K$ (ionized and molecular) vs. bolometric luminosity of the AGN, L_{AGN}. The solid, dashed and dotted lines represent 100%, 5% and 0.1% of the total bolometric luminosity of the AGN in the form of the outflow power. The data points from this work are shown in red stars (XID178, XID5627). The molecular outflows are represented by squares (Cicone et al. 2014; Feruglio et al. 2015; Sun et al. 2014), while the rest of the data points represent ionized outflows (Carniani et al. 2015; Harrison et al. 2014; Cresci et al. 2015a; Brusa et al. 2015a; Greene et al. 2012). The outflow properties for all the ionized outflows were obtained using [OIII] λ5007 line except for Cresci et al. 2015a for which analysis from Hβ is shown in this plot to represent the differences in analysis from the two lines for the same data.

the radiation pressure of the wind from the AGN and the outflow energies are of the order of $\approx 20 \cdot L_{AGN}/c$ (AGN radiation pressure momentum) implying an energy conserving outflow (Cicone et al. 2014; Feruglio et al. 2015). XID178 and XID5627 have similar bolometric luminosity, outflow velocity and mass outflow rates (see Table 2.1 and 2.5). The ratio of the outflow momentum rate to that of AGN radiation pressure momentum comes out to be much less than 1:1 ($\approx$ 0.01:1), which is also consistent with previously reported ionized gas momentum rates (Carniani et al. 2015). The lower ratio might be due to the discrepancy in the outflow mass rates in the molecular and ionized gas phase.

2.7.3 Uncertainties in the estimates

Although there is substantial observational evidence that outflows are common in AGNs, the derived quantitites associated to these outflows are affected by significant uncertainties.

We have adopted the most commonly used outflow model, i.e. the bi-conical outflow, to derive the mass outflow rates and hence the power driven by the AGN. Mass outflow rate estimates would change if we considered a shell-like outflow geometry instead. This has been extensively discussed in Cicone et al. (2014) and Maiolino et al. (2012) where it was shown that a shell-like geometry gives a higher outflow rate (by a factor of ~3) relatively to the multi-conical or spherical geometry considered above. Since we do not have a 3D view of these galaxies, the exact outflow morphology of any of the targets could not be inferred. However, with the 2D images in hand, one could assume a bi-conical outflow model in all the objects with XID5627 probably having a wide-angled outflow (inferred from the broad component map in Fig. 2.3, middle right panel) towards the line of sight of the observer. This suggests that the outflow pattern might vary on an object-by-object basis and might introduce errors due to the assumptions made.

As we have illustrated in Figs. 2.9 and 2.10, using different prescriptions for determining outflow velocities introduces a range of outflow properties, the extent of which depends on the emission line profile. In all cases, w_{80} gives a higher velocity value compared to the v_{10} on the integrated spectrum and the broad component. For a Gaussian profile w_{80} is close to the FWHM of the line and relates to the typical velocity of the emitting gas, while v_{10} gives an estimate of velocity the gas moving towards us at the high velocity end. The outflow model we use do not take into account these differences.

Another important source of uncertainty is the lack of a measurement of the electron density for each single AGN studied. The range of electron density in

NLR is believed to be in the range $\leq 50 - 1500$ cm^{-3} (Peterson 1997). Observations of local galaxies have shown that the electron density generally drops with distance from the galactic centre, down to values $\lesssim 50$ cm^{-3} in the galaxy outskirts (Bennert et al. 2006). The observed outflows in our case are extended to kiloparsec scales, but if the gas is dragged out by an over-pressurized bubble the density could be relatively high. We adopt an average electron density of 100 cm^{-3}, based on recent observations by Perna et al. 2015a of a bright QSO (XID5321) using [SII] λ6716,31 for which an electron density of $\sim$120 cm^{-3} have been reported in the off-nuclear regions. However, this method is not effective in measuring electron densities lower than 100 cm^{-3} (or greater than 1500 cm^{-3}: Peterson 1997). Moreover it is challenging to resolve the [SII] doublet near Hα in many objects and is usually very faint. Hence, we have limitations from observational point of view in determining the electron densities accurately.

A similar concern applies to the temperature estimates as well. The normalization factors in Eqs. 3-5 could change by a factor of $\sim$10 depending on whether the temperature is assumed to be 10,000 K or 25,000 K since the emissivity changes by this factor.

Other sources of uncertainties come from using different lines for deriving outflow properties (such as [OIII]λ5007 and Hβ) and the multi-phase nature of outflows which has been discussed before. The overall errors in the estimates of mass outflow rates and kinetic energies are therefore large, possibly of the order of a factor $\sim$ 100.

Hence, we stress the importance of further detailed observations to constrain the outflow energies and hence accurately determine whether AGN or the star formation could drive such outflows.

2.8 Summary

We summarize below the main results of this work:

- The selection of AGN in an outflowing phase based on the empirical curve by Fabian et al. (2008) (see Fig. 2.1) seems effective. We were able to verify the presence of such outflows using a kinematic analysis of the [OIII] λ5007 line in at least four out of a sample of five objects, three of them reported for the first time in this work (XID178, XID5627 and XID54204) and the fourth (XID2028) already presented in Cresci et al. (2015a).

- In XID178 and XID5627, the outflow is extended up to ~8.5 kpc in the host galaxy while for XID54204, the [OIII] λ5007 emission is not spatially resolved. All the objects show high velocities of ~500-1800 km/s in their integrated spectra. The spatial distribution of [OIII] λ5007 in XID178 and XID5627 might suggest the presence of different outflow morphology in the galaxies.

- For XID5330 we do not have enough S/N ratio and spectral resolution to trace an extended [OIII] λ5007 emission (if present).

- HST images of the sample do not show any disturbed morphology, possibly ruling out a merger-driven scenario for the observed outflows.

- Based on the measured kinetic energies of the outflows, both star-formation ($\gtrsim$ 0.1% coupling) and AGN radiation (< 0.1% coupling) could be the dominant power source. In this work we were able to trace only the ionized phase of the outflows. Follow-up observations of the molecular components could allow us to put stronger constraints on the origin of these outflows.

- The assumptions of current models introduce errors of several orders of magnitude on the outflow properties, which makes it difficult to infer the source of these outflows. Accurate determination of the electron density and electron temperatures in these galaxies is required to confirm if these outflows are powered by an AGN or star formation. Moreover, observations at mm wavelengths are required to trace the outflows component in molecular gas phase.

From this and previous works, it is now apparent that the presence of outflows in high redshift galaxies hosting an AGN is very common. But one has to be cautious since most of these studies are based on pre-selected targets, to maximize the chance to actually detect outflows. There is a strong need for a blind IFS survey of AGN to trace the properties and the incidence of outflows as a function of AGN physical properties. We have recently started a Large Program with SINFONI at VLT, "Survey for Unveiling the Physics and the Effect of Radiative feedback" (SUPER, PI Mainieri), designed to test the presence of outflows and their impact on the host galaxy in a sample of > 40 AGNs at z~2 covering a wide range of bolometric luminosities, Eddington ratios and SFRs. Another important goal of this survey will be to minimize the uncertainties when computing the outflow energetics, in particular deep K-band observations will allow reliable determinations

of the electron density object by object using the [SII] doublets. Further details of this survey are presented in Chapter 5.
This chapter displayed the level of uncertainty we have in mass outflow rate measurements, primarily due to the unconstrained values of electron density. The next chapter focuses on spatially resolved electron density measurements in a sample of low redshift AGN host galaxies using the S7 survey. The low redshift sample have the advantage of high spatial resolution compared to the high redshift galaxies and can be used to find a trend of the density values as a function of distance from the center.

Chapter 3

Electron densities in AGN Narrow Line Region with S7 survey

3.1 Motivation

Ionizing radiation from accreting SMBH at the center of galaxies are believed to illuminate the narrow line region in AGN host galaxies. Unlike the unresolved BLR, the NLR can be extended up to the host galaxy scales. This offers a platform to study the ISM properties of the AGN host galaxies such as electron density, electron temperature and the shape of the ionizing radiation field using rest frame optical emission lines arising from the ionized gas (e.g. Kewley & Dopita 2002; Dopita et al. 2006; Bennert et al. 2006; Kewley et al. 2013).

For low redshift galaxies the spatial resolution is high enough to resolve the NLR structure and hence, study the NLR properties as a function of distance from the galactic nucleus. The electron density is a crucial parameter of the ISM as it is used to determine physical quantities such as chemical abundances in the local nebulae and mass outflow rates due to AGN or star formation. The typical NLR electron density is commonly assumed to be between ~50-10,000 cm^{-3}, which translate to a large uncertainty in the estimation of the physical quantities mentioned above (Müller-Sánchez et al. 2011; Kakkad et al. 2016).

Several studies on electron density for high redshift galaxies have been conducted in the past decade (e.g. Hainline et al. 2009; Sanders et al. 2016; Shirazi et al. 2014) most of which claim elevated electron densities linked to the higher star formation rates (Kaasinen et al. 2017). However, at these high redshifts, there are severe observational limitations in resolving the central and the outer regions

of the galaxy and most of these studies are based on ”average” density values which have been obtained from integrated spectra using one-dimensional fiber or single slit spectroscopy. This has the limitation that the estimated densities could be contaminated by the higher density nuclear regions of the galaxies. Hence, previous studies lack spatially resolved analysis, due to a combination of limited signal-to-noise (S/N) in each pixel and/or low spatial resolution.

Galaxies at low-redshift, on the other hand, overcome the limitation of low spatial resolution and therefore, are ideal to perform spatially resolved electron density studies. These studies combined with star formation and [OIII]λ5007 (hereafter [OIII]) maps would give us insights into how the density structures within the host galaxy are affected by AGN and star formation processes.

Most of the electron density studies are based on the [SII] λ6716, 6731 (hereafter [SII] doublet) or [OII] λ3726, 3729 (hereafter [OII] doublet). Both these set of lines arise from two closely spaced “metastable” energy levels due to which the relative flux values only depend on the electron density occupying these levels and any degeneracy due to different ions is also removed (Osterbrock & Ferland 2006). The usage of the [OII] doublet to determine the electron density is limited by the spectral resolution of most instruments, including WiFeS (see Sects. 1.3 and 1.6) used in this chapter, due to which the [OII] doublets are usually blended. Hence, we will use the [SII] doublet to measure electron densities in this chapter. The [SII] doublet can be used to measure densities between 50-1500 cm^{-3}, which falls within the typically estimated range of densities in the extended NLR. Below and above these values, the flux ratios of the doublets are saturated (see Fig. 1.6).

Previously spatially resolved electron density maps have been constructed using IFU and single-slit spectroscopy. Cresci et al. (2015b) presented electron density map for NGC5643 (z$\sim$0.004) using MUSE IFU spectroscopy and found that the electron density in the NLR drops below $\sim$50 cm^{-3} at a distance of 5$''$ ($\sim$400 pc) from the center of the galaxy. Using single slit spectroscopy, Bennert et al. (2006) presented the electron density as a function of radius from the center for a sample of nearby Seyfert galaxies and also found the densities to saturate in the lower limit for distances larger than 500 pc. Previous studies on the electron density structure for low redshift AGN host galaxies are limited to small samples which prevents a global understanding of the properties of the whole AGN population.

Today, the large samples of optical and near-Infrared IFU spectra of extragalactic sources building up through IFU surveys such as SAMI (Croom et al. 2012), MaNGA (Bundy et al. 2015), S7 (Dopita et al. 2015) and KASHz (Harrison et al. 2016) allow to repeat this study on a statistical sample of AGNs. In

the following chapter, we present the electron density distribution for a sample of low redshift Seyfert galaxies derived from the S7 survey with the aim to derive the electron density profiles as a function of radius and identifying the mechanisms which drive the observed density patterns.

The chapter is structured as follows. In Sect. 3.2, we briefly summarize the S7 sample selection, its observations and data reduction procedures. Sect. 3.3 gives a comprehensive overview of the analysis procedures namely line fitting, map construction and error estimation. The resulting spectra, star formation and extinction maps, [OIII] flux maps and electron density profiles are reported in Sect. 3.4. We also discuss the processes leading to observed electron density patterns and the implications of these results for high redshift studies. A summary of the main results is reported in Sect. 3.5

Throughout this chapter, we adopt a Λ-CDM cosmology with H_0=70 km/s/Mpc, $\Omega_m = 0.3$, $\Omega_\Lambda = 0.7$ and Ω_r=0.0.

3.2 Observations and Data reduction

Our sample is drawn from the *Siding Spring Southern Seyfert Spectroscopic Snapshot Survey* (S7, Dopita et al. 2015), which is an Integral Field Spectroscopic survey of nearby Seyferts and LINER galaxies at z<0.02. The observations for the S7 survey were carried out using the Wide Field Spectrograph (WiFeS) on the ANU 2.3 m telescope at Siding Spring observatory. The typical field of view is 38×25 arcsec^2 with the nucleus centered on the field of view and orientation close to the major axis of the galaxy (e.g. NGC1365 in Fig. 3.1). The observations used in this work have a moderately high spectral resolution of R=7000 (~50km/s) in the wavelength range 530< λ <710 nm and lower resolution of R=3000 for 340< λ <560 nm. The average spatial resolution for the observations is ~1 arcsec with exposure times in the range 800-1000s. The data reduction was performed using Python pipeline PYWIFES (Childress et al. 2014) which provides calibrated sky subtracted data cubes resampled on a 1×1 arsec^2 pixel scale. The error budget on flux calibration is up to 4%.

The survey is aimed at probing the ionizing mechanism of the extended narrow line region (ENLR) of nearby radio-selected AGNs. Given the redshift distribution of the sample, the spatial resolution of the data is ≤400 pc/arcsec and diagnostic lines such as [SII] used in this chapter are within the spectral range of WiFeS. We refer the reader to Dopita et al. (2015) for more details about the observing strategy and sample selection and Childress et al. (2014) for details on

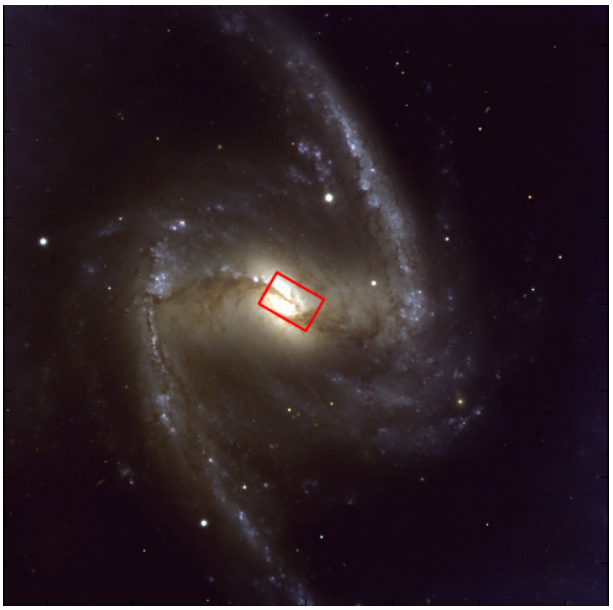

Figure 3.1: A representative figure of the FOV covered by WiFeS instrument used in the S7 survey. The figure shows a 7×7 arcmin^2 FORS1/VLT image of NGC1365, one of the galaxies targeted with the S7 survey. The WiFeS FOV (38×25 arcsec^2) is overlaid in red. North is up and east is towards left. Image Credit: ESO

data reduction.

The spectra obtained for this survey covers important diagnostic emission lines from ionized gas for the NLR such as the Balmer Hα & Hβ lines and forbidden transitions such as [OII]λ3726,3729, [OIII] λ4959,5007, [NII]λ6549,6585, and [SII]λ6716,6731. Such a wide range in the coverage of emission lines makes this survey extremely useful to disentangle the contribution to these line fluxes due to star formation or AGN or both using spatially resolved diagnostic diagrams.

3.3 Data analysis

We use the [SII] doublet flux ratio to determine electron densities as the [OII] doublet could not be resolved with the spectral resolution of WiFeS instrument. For the typical range of values of the electron density in the ENLR i.e. ~50-1500 cm^{-3}, the theoretical [SII] doublet line ratio is fairly close to unity (Osterbrock

& Ferland 2006; Sanders et al. 2016). Therefore, the inferred electron density is highly susceptible to minute changes in the flux ratio. We remove all the targets for which the [SII] line is contaminated by sky lines, stellar continuum, atmospheric absorption and where the S/N of the [SII] emission line is less than 5. The following section provides an overview of the analysis tools used in this chapter.

3.3.1 Emission line fitting

The raw data cubes of the targets include a contribution from the underlying stellar continuum which has to be carefully subtracted in order to compute the correct emission line fluxes and reproduce the emission line profiles during the line fitting procedure. We use the IDL emission line fitting toolkit, LZIFU (Ho et al. 2016) which makes use of the pPXF code (Cappellari & Emsellem 2004) to subtract the stellar continuum. Further details are given in (Ho et al. 2016). An example spectrum of NGC1365 is shown in Fig. 3.2 where the raw integrated spectrum for the "red" and the "blue" cubes[1] is shown in blue and the stellar continuum fit is overlaid in red.

Once the stellar continuum has been subtracted from the cubes, we extracted the spectra from the entire field of view, except the bottom two rows of the pixels due to instrumental defects. The extracted spectrum was used to derive an average value of electron density over all the integrated pixels. We perform Gaussian line fitting primarily for Hβ, [OIII]λ4959, 5007, [NII]λ6549, 6585, Hα and the [SII] doublet. As mentioned above, due to the fact that the [SII] flux ratios are highly sensitive to small changes in electron density, we only take into account those spectra for which the S/N > 5 for each of the [SII] doublet. We used the IDL fitting routine MPFIT (Markwardt 2012) for simultaneous fitting of the nuclear continuum and the emission lines. The emission lines were reproduced using one or multiple Gaussian models. The choice of the number of Gaussians depended on the S/N of the underlying data, the spectral resolution of the two cubes and the ability of the chosen model to reproduce the line profiles.

A few constraints were employed while performing the line fitting to avoid any degeneracy in the multi-component fits. The line widths were constrained to be always greater than 50 km/s to avoid any spurious detection due to the presence of skylines. The line widths of each narrow component were coupled to each other assuming all these components trace the gas moving at a systemic velocity of the

[1]The "blue" and "red" cube/spectrum in this chapter refer to the wavelength ranges 340< λ <560 nm and 530< λ <710 nm respectively.

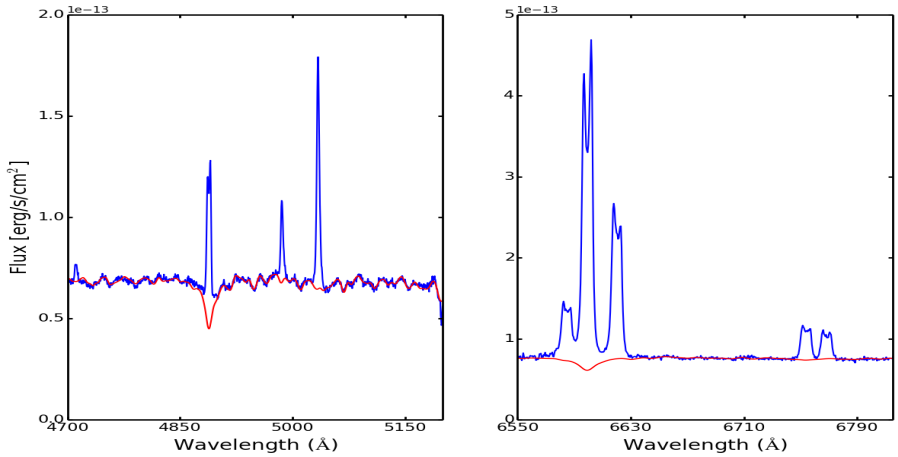

Figure 3.2: An example stellar continuum fitting in NGC1365, one of the galaxies targeted with S7 survey. The stellar continuum fit using pPXF is shown in red and the raw spectra in blue. The left panel shows the spectra in the "blue" cube zoomed in the region around Hβ and [OIII]λ4959, 5007 emission lines and the right panel shows the spectra in the "red" cube zoomed in the region around [NII]λ6549, 6585, Hα and the [SII] doublet. The X-axis in both the panels shows the observed wavelength.

host galaxy. In most of the cases, the Hα profile shows the presence of a very broad component which is relatively faint. We also coupled the relative emission line flux ratios for [OIII]λ4959,5007 and [NII]λ6549,6585 based on theoretical values (e.g. Storey & Zeippen 2000; Dimitrijević et al. 2007).

The multi-component line fitting was performed for each pixel across the FOV allowing minor variations in the wavelength centroids and line widths with respect to the values obtained in the integrated emission line fitting. The fluxes were always kept positive as we do not expect or assume the presence of absorption features once the stellar continuum has been subtracted. In the presence of broad lines from the BLR, we subtract the broad component (mainly in the case of Hα) with the same centroid and width as that obtained in the integrated spectrum and only allowing variations in the flux.

3.3.2 Determination of electron densities

For calculating electron densities, we use the prescription employed in Sanders et al. (2016):

$$n_e(R) = \frac{cR - ab}{a - R} \tag{3.1}$$

where the flux ratio R=f([SII]λ6716)/f([SII]λ6731]), a=0.4315, b=2107 and c=627.1. It is apparent that for flux ratios close to unity, the density ratio could vary between ~50-1500 cm^{-3}. A number of assumptions have been made to arrive at Eq. 3.1 by Sanders et al. (2016) which we summarize here (see also Kaasinen et al. 2017). The electron temperature is assumed to be 10,000 K and the electron densities are directly proportional to HII region pressure. For the typical temperatures in a NLR i.e. between 10,000-25,000 K, the above relation does not change considerably compared to the errors in measurement. Similarly, the latter assumption may introduce an uncertainty by overestimation of densities in metal-rich galaxies. However the errors due to this assumption is also significantly less than the measurement error. The density profile as a function of the doublet flux ratio for T=10,000 K is shown in Fig. 1.6.

A linear relation between the [SII] doublet ratio and the electron density makes it effective in measuring the electron density in the aforementioned ranges. However beyond these limits, the [SII] doublet flux ratio saturates. Therefore, we clip the maximum and minimum values to 1500 and 50 cm^{-3} respectively. The line ratios are calculated across the FOV and consequently converted to density values to arrive at density maps which are shown in Sect. 3.4.

The error cubes obtained from the PYWIFES reduction were used to create 100 mock data cubes by the addition of Gaussian random noise from the corresponding error values. We repeated the line fitting procedure for each of these mock data cubes to obtain standard deviation of various parameters used in the analysis. The average uncertainty in the density measurements is estimated at $\sim$100 cm^{-3}.

Lastly, the average seeing during the observations was $\sim$1-2 arcsec. Since the extent of emission from most of the targets is larger than the point spread function (PSF), we do not expect any significant change in our results if beam smearing is taken into account. The following section summarizes our main results and interpretations from the analysis techniques presented above.

3.4 Results and Discussion

The integrated spectrum of the blue and the red cubes zoomed around the emission lines Hβ, [OIII]λ4959,5007, Hα and [SII] doublet is shown for NGC1365 as an example in Fig. 3.3. The spectra for the rest of the sample used in this chapter along with the respective notes on each target has been moved at the end of this chapter (see Sect. 3.6). In NGC1365, there are no clear signatures for the presence of an ionized outflow from the [OIII] line profile in the blue spectrum shown in the left panel of Fig. 3.3. The narrow Hα and the [NII] profiles are doubly peaked suggesting a rotating galaxy. The Hα profile also indicates the presence of a strong broad component from the BLR. Each of the [SII] doublets in the integrated spectrum is well reproduced using two Gaussian components suggesting a rotation like in the case of Hα profile. The [SII] spectrum also reveals the presence of He I emission at $\sim$6680Å.

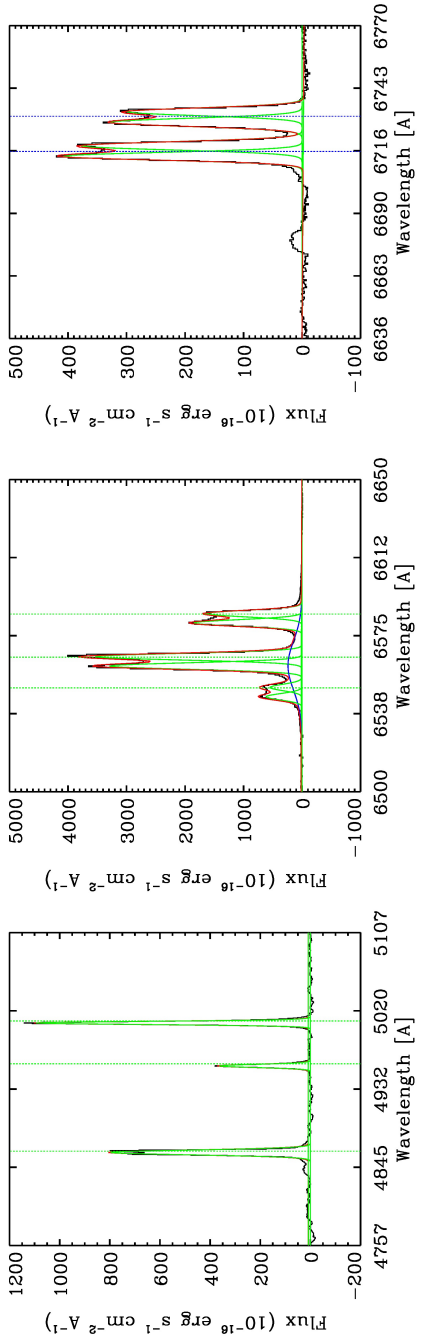

Figure 3.3: The integrated spectrum of NGC1365 from the blue cube zoomed in on Hβ and [OIII] lines (left panel), the red cube zoomed in on Hα and the [NII] lines (middle panel) and [SII] doublet (right panel). All the wavelengths on the X-axis are the rest frame wavelengths. The black line shows the observed spectrum and the red, blue and green curves show the total fit, broad Gaussian component and the narrow Gaussian component respectively. The vertical lines represent the expected position of the emission lines from the redshift of the targets. The small bump at ~6680 Å is due to He I emission.

Target	n_e [a]	β [b]
NGC613	111 ±30	0.25 ±0.03
NGC1365	148 ±15	0.05 ±0.01
NGC1672	163 ±16	0.08 ±0.01
NGC4303	110 ±60	0.15 ±0.03
NGC4691	92 ±15	0.12 ±0.01
NGC5990	133 ±23	0.08 ±0.01
NGC6000	210 ±40	0.17 ±0.02
NGC6221	168 ±26	0.19 ±0.06
NGC7469	270 ±60	0.22 ±0.03
NGC7496	200 ±40	0.14 ±0.02
NGC7582	150 ±60	0.20 ±0.02

Table 3.1: [a]Electron density calculated from the integrated spectrum extracted from the S7 field-of-view, [b]Power law index for the fit between electron density and distance from the center as presented in Eq. 3.2.

The electron density derived from the integrated spectrum for NGC1365 and the rest of the targets from this survey is given in Table 3.1. The densities mentioned in the table are calculated from the entire [SII] profile i.e. the sum of the individual Gaussian components for each line. Details about the derivation of electron density from the [SII] doublet have been mentioned in Sect. 3.3.

Fig. 3.4 shows the Hα and [OIII] flux map, extinction map, electron density map and density profiles as a function of distance from the center for NGC1365 as an example. All the maps are centered at the position of the AGN and the white bar at the upper right corner shows the representative 500 pc line at the redshift of NGC1365. The dust extinction maps were obtained using the Balmer Decrement (H_α/H_β) assuming a Calzetti et al. (2000) dust attenuation law and a fixed temperature of 10,000 K which is the same as that used for the electron density maps. The extinction maps are very useful to correct for dust obscuration in the star formation maps obtained with the narrow Hα. The electron density maps, however, are not expected to be significantly affected by the reddening correction since the [SII] doublet are closely spaced and the reddening correction factors are almost the same. For the purpose of our analysis, we compare the extinction maps with narrow Hα flux maps (or star formation maps), [OIII] and electron density maps to understand the origin of the density distribution.

For the rest of the targets, we follow a similar procedure and for simplicity we just

show the extinction and electron density maps in Figs. 3.5, 3.6 and 3.7.
Star formation maps: The top left panel in Fig. 3.4 shows the star formation map for NGC1365 as traced by the narrow component of Hα line. The star formation is rather clumpy in NGC1365 and a comparison with the extinction map in the middle left panel indicates that the star formation on the upper right clump might be highly obscured by the dust in the galaxy. The presence of dust has also been confirmed by 24 μm observations in Alonso-Herrero et al. (2012). A comparison between the SFR derived from the 24 μm continuum and narrow Hα line shows that ~85% of the ongoing star formation in the central regions of NGC1365 is taking place in dust obscured regions. We find similar patterns in case of NGC1672, NGC613, NGC4303 and NGC7469, where the unobscured star forming regions are surrounded by a ring of dust or obscuring material. The star forming regions do not necessarily coincide with regions of [OIII] emission as well which is apparent from the positions of magenta and white contours in Figs. 3.4, 3.5 and 3.6. Similarly to the case of the [SII] doublet ratio, the extinction corrections are not expected to significantly affect the [OIII] distribution.
Electron density maps: The electron density maps are shown in the middle right panel of Fig. 3.4 for NGC1365 as an example and the respective plots for other targets have been shown in the right panels of Figs. 3.5, 3.6 and 3.7. As mentioned earlier in Sect. 3.3, we have employed a signal-to-noise cut of 5 in each pixel to arrive at these density maps. This is because the density values are highly sensitive to the [SII] doublet flux ratio and hence we want to remove any uncertainty due to poor data. The overlaid white contours in all figures show the locations of unobscured star formation from the narrow Hα maps and the magenta contours show the locations of [OIII] emission. From the 500 pc line in all these maps, it is clear that we are probing the central 2-5 kpc with the WiFeS FOV. The yellow arrow in all the maps indicates the North direction.
Comparing the density maps with the location of narrow Hα contours in in Figs. 3.5 and 3.6, it is clear that in general, electron density is higher in sites of higher star formation. However, exceptions to this rule does exist, as shown in Fig. 3.7 where the density patterns do not necessarily correlate with the all the regions of narrow Hα emission. In some cases, like that of NGC7469 (Fig. 3.8), the density has an excess at the S-E end of the maps which is not necessarily a site of high star formation. However, this is also a region of high extinction as shown in the left panel of Fig. 3.8, due to which we speculate that this is a region of star formation obscured by the presence of dust. Hence, it is important to take extinction effects into account.

These maps are also useful to quantify how the electron density drops as a

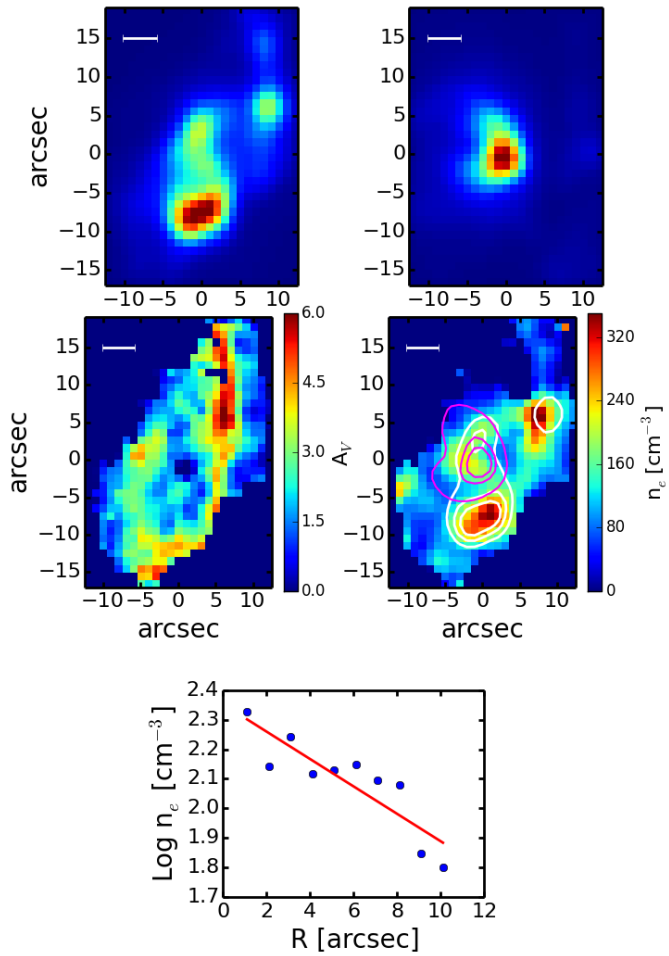

Figure 3.4: Maps and density profiles of NGC1365. *Top left*: Narrow Hα map showing the star forming regions in the host galaxy, *Top right*: [OIII] λ5007 flux map, *Center left and right*: Extinction map derived from Hα/Hβ line ratios and Electron density map derived from [SII] λ6716/[SII]λ6731 line ratio respectively (see text for further details). The overlaid white contours represent the narrow Hα emission from top left panel and the magenta contours represent the [OIII] emission from the top right panel which shows that the densities are higher in sites of star formation. The white bar in all the maps denote the 500 pc scale corresponding to 1 arcsec for the redshift of the target. *Bottom Panel:* Electron density profile as a function of radius from the center of the target ((0,0) in the maps). The blue data points represent the profiles derived from the map itself and red line shows the best fit model assuming a power law profile in density. The power law index for this target is -0.05.

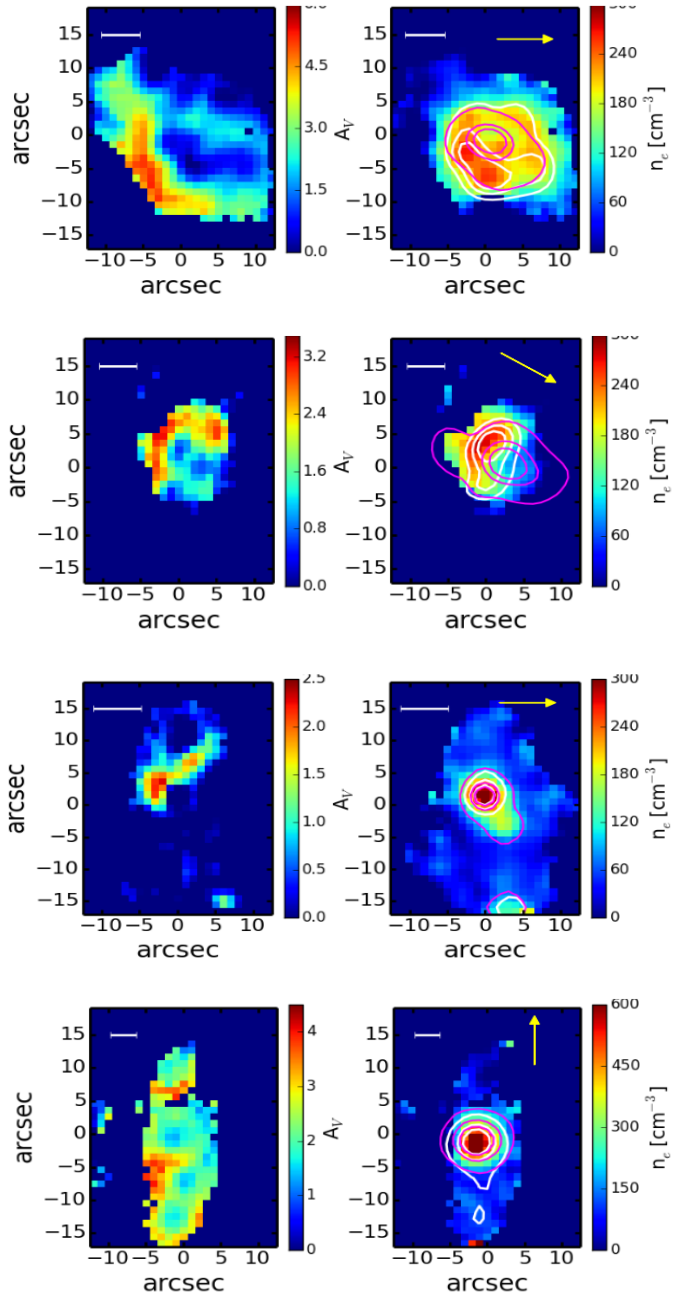

Figure 3.5: Balmer reddening maps (left) and electron density maps (right) of the targets presented in this chapter (From top to bottom: NGC1672, NGC613, NGC4691, NGC6000). The white contours trace the narrow Hα component and the magenta contours correspond to the [OIII] emission. The white line in the top right corner of all maps show the representative 500 pc line. The axes units are arcsec. The yellow arrow shows the North direction. The targets here show a spatial correlation between sites of high star formation and high densities.

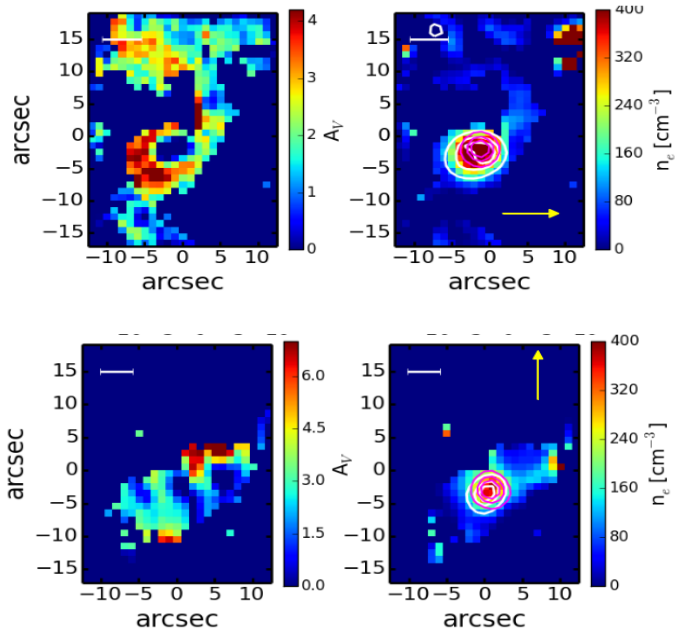

Figure 3.6: Same as Fig. 3.5 but for targets NGC6221 (top) and NGC7496 (bottom). These targets also show the spatial correlation between high density regions and higher star formation traced by narrow Hα line. See text for further details.

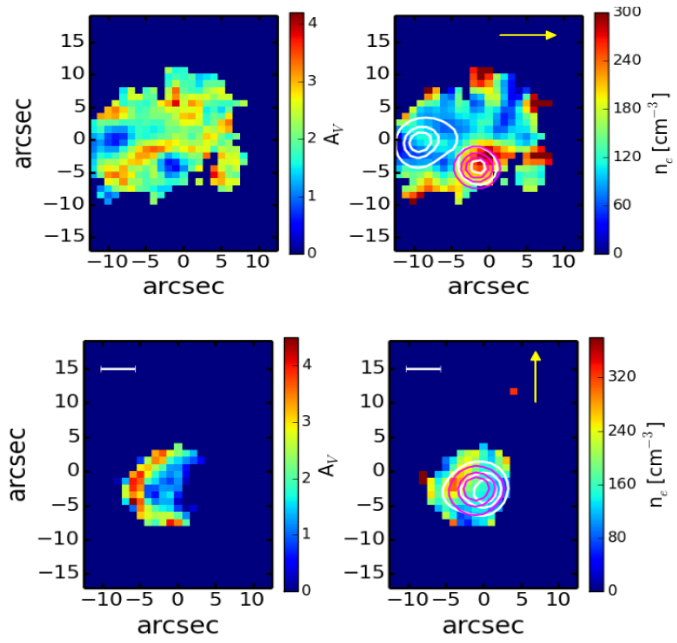

Figure 3.7: Same as Fig. 3.5 but for targets NGC5990 (top) and NGC4303 (bottom). Targets here show an exception to the general trend in the density and star formation correlation as seen in Fig.s 3.5 and 3.6.

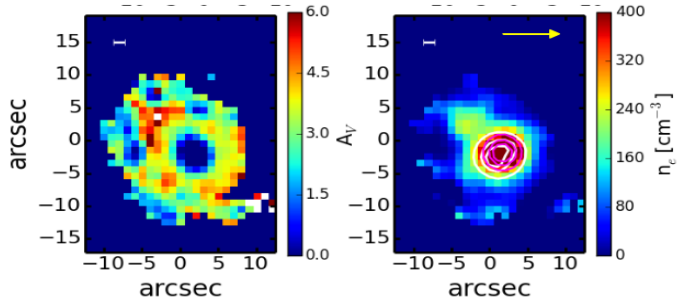

Figure 3.8: Plot conventions are the same as that of Fig. 3.5 but for the target NGC7469. The density pattern extend beyond the narrow Hα emission and a comparison with the reddening map suggests the possibility of obscured star formation.

function of distance from the central AGN. The electron density profiles were constructed with an annulus one pixel wide, which roughly matches the angular resolution of the observations and centered on the AGN. The central one arcsec region has been avoided while constructing these profiles since the densities from the [SII] method are saturated in this region. The density profile obtained from the electron density map is shown as blue data points for NGC1365 as an example in the bottom panel of Fig. 3.4, while the profiles of the rest of the targets are shown in Fig. 3.9.

It's clear from the plots in Fig. 3.9 that in general, electron density decreases as a function of distance from the center of the galaxy. This drop in density is not necessarily uniform due to the clumpy density profiles which mimic the star formation in some cases (e.g. NGC1365, Fig. 3.4). Nevertheless, to a first order approximation, we can fit these density profiles as a power law given by the following equation:

$$n_e = \alpha \cdot R^{-\beta} \tag{3.2}$$

where β is the power law index, α is the normalization constant and R is the distance (in arcsec) from the center. Table 3.1 reports the value of power law index obtained for all the targets used in this chapter. It is apparent from this table that most of the targets have a power law index between ~0.1-0.2. The fit to the density profiles obtained from the maps are shown by the red line in all the plots in Fig. 3.9.

It is apparent from the profiles that in all the cases, the electron density in the NLR drops to <50 cm^{-3} for distances larger than 1 kpc from the center. Comparison of the density maps with the position of the magenta [OIII] contours in Figs. 3.5, 3.6 and 3.7 suggests that this trend is also true in the [OIII] emitting regions. These density values have significant implication in the determination of ionized gas mass outflow rates using [OIII] as a tracer which requires an assumption in the value of electron density value. Density values of <50 cm^{-3} is significantly lower compared to the usually assumed values of 500-1000 cm^{-3} (e.g. Cano-Díaz et al. 2012; Carniani et al. 2015) which suggests that the mass outflow rate might have been underestimated by a factor of 10-20 in these studies. However, this would be true for low redshift galaxies, but we expect high redshift galaxies to have significantly different conditions as described later. Nevertheless, from the density profiles in Fig. 3.9, one can infer that in kiloparsec scales within the host galaxy, we do not expect densities to go as high as 500-1000 cm^{-3}.

The data set presented in this chapter makes use of AGN host galaxies at low

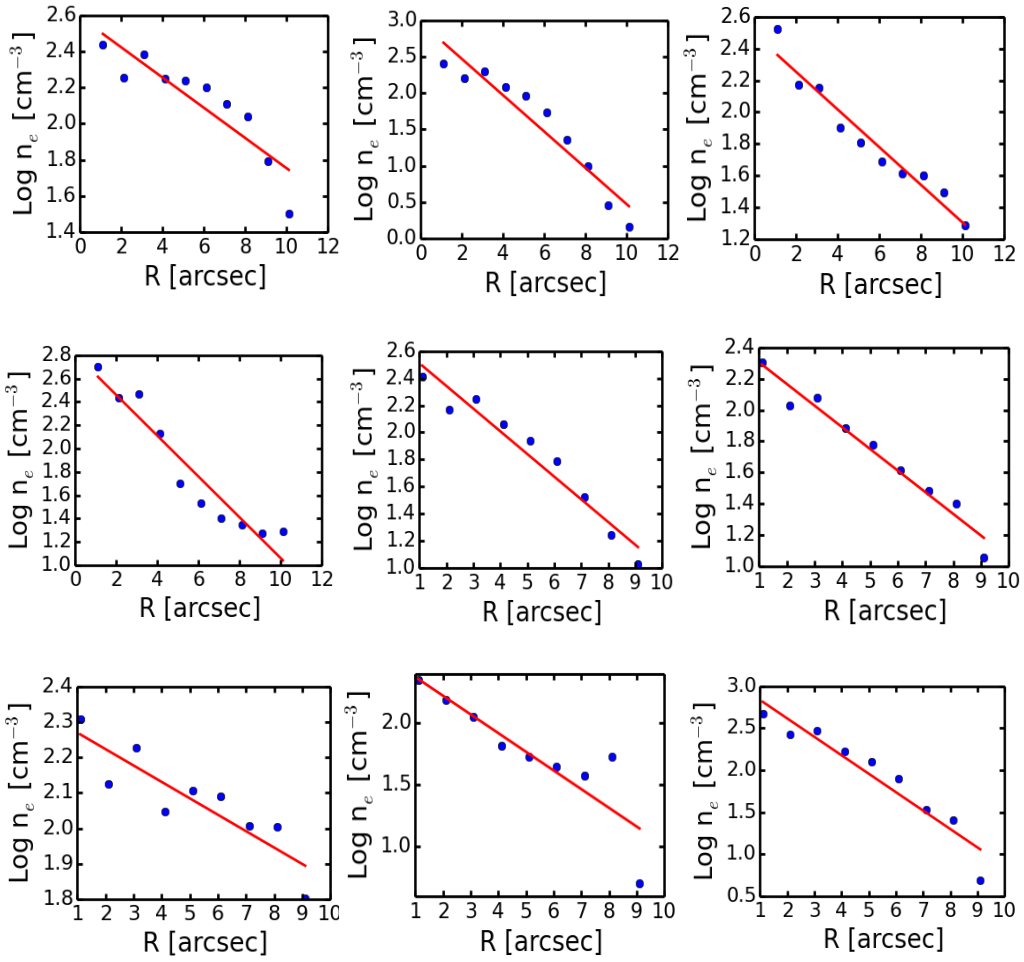

Figure 3.9: Electron density profiles of the targets presented in this chapter. From left to right, *Top panel:* NGC1672, NGC613, NGC4691; *Middle panel:* NGC6000, NGC6221, NGC7496; *Bottom Panel:* NGC5990, NGC4303, NGC7469. Blue data points show the electron density values obtained from the maps in Figs. 3.5, 3.6, 3.7 and 3.8 while the solid red line shows the power law fit to the profile (See text for details). The power law index are reported in Table. 3.1.

redshift. To understand the implications of this study for galaxies at high redshift, it is important to note that the ISM conditions at high redshift is significantly different compared to those at low redshift. Observations and theoretical models over the past decade have shed light into the history of star formation and ISM gas content as a function of cosmic time (e.g. Silk & Mamon 2012; Madau & Dickinson 2014). It is now accepted that the volume averaged star formation rate was at its maximum in the universe at $1< z <3$ and that the gas content is higher at this epoch (e.g. Scoville et al. 2014). Taking this into account along with the spatial correlation between the electron density and the star formation maps presented earlier in this section, we naively expect the electron density would also increase as a function of redshift. This has been confirmed by several works in the previous years where it has been found that the "integrated" electron densities are higher for high redshift galaxies compared to the local counterparts (e.g. Lehnert et al. 2009; Hainline et al. 2009; Bian et al. 2010; Shirazi et al. 2014; Sanders et al. 2016). Consequently, we would also expect electron density to evolve with SFR which has been inferred in some of the recent high redshift studies using single slit spectroscopy (Kaasinen et al. 2017).

3.5 Summary and Conclusions

This chapter presented a survey of electron densities in the NLR for a sample of low redshift radio selected AGNs. The electron densities were measured using the flux ratio of [SII]λ6716,6731 emission lines and spatially resolved maps of these densities were created using the optical IFU data from WiFeS intrument in the central regions of the galaxy. These density maps were then compared with the star formation maps from the narrow component of Hα emission line and [OIII] maps to discern the origin of the density structures. The star formation maps were also compared with the extinction maps to infer the presence of dust obscured star formation. The main conclusions of our analysis are summarized as follows:

- The electron densities are higher in sites of high star formation rate. This implies that we expect higher electron densities for galaxies having higher star formation rate on average which might explain recent observations of evolution of these densities with SFR for high redshift galaxies (e.g. Kaasinen et al. 2017). Dust extinction derived from Balmer reddening suggests obscured star formation in some galaxies. Consequently, we also expect the "integrated" electron density to be higher in high redshift galaxies due to maximal star formation at this epoch.

- Although the electron density maps are asymmetric, it drops as a function of distance from the center of the galaxies. To a first order approximation, these profiles can be modeled as a power law (Eq. 3.2) with the power law index between 0.1 and 0.2 which suggests that the electron densities fall below 50 cm^{-3} which is the lower limit of density measurements using the [SII] doublet.

The method of spatially resolved electron density maps presented in this chapter offers a way to have tighter constrains on the mass outflow rates measured in Chapter 2. Although a low redshift sample has been presented in this chapter, the density profiles suggests that we do not expect high densities of 500-1000 cm^{-3} in kiloparsec scales of the NLR in AGN host galaxies.
Chapters 2 and 3 gave an overview of the ionized gas dynamics in AGNs. The next chapter presents a comprehensive study of another gas phase, namely the molecular gas properties of a representative sample of moderate to high luminosity AGN host galaxies.

3.6 Spectra of S7 galaxies

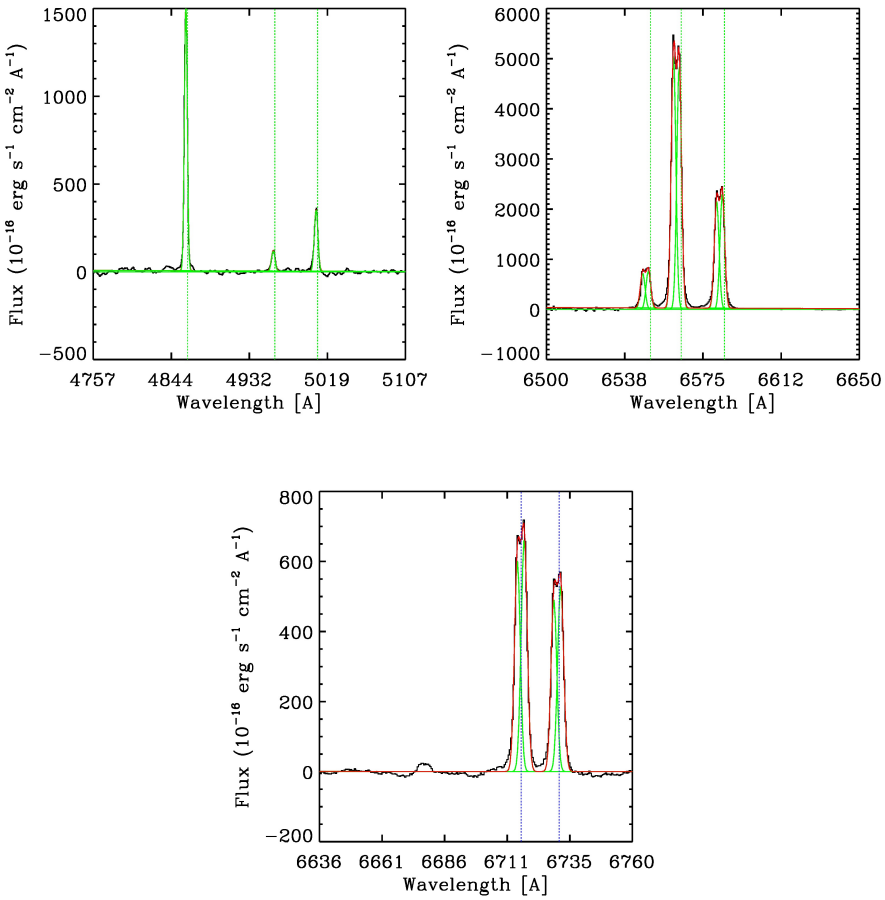

Figure 3.10: Spectra as in Fig. 3.3 for NGC1672.

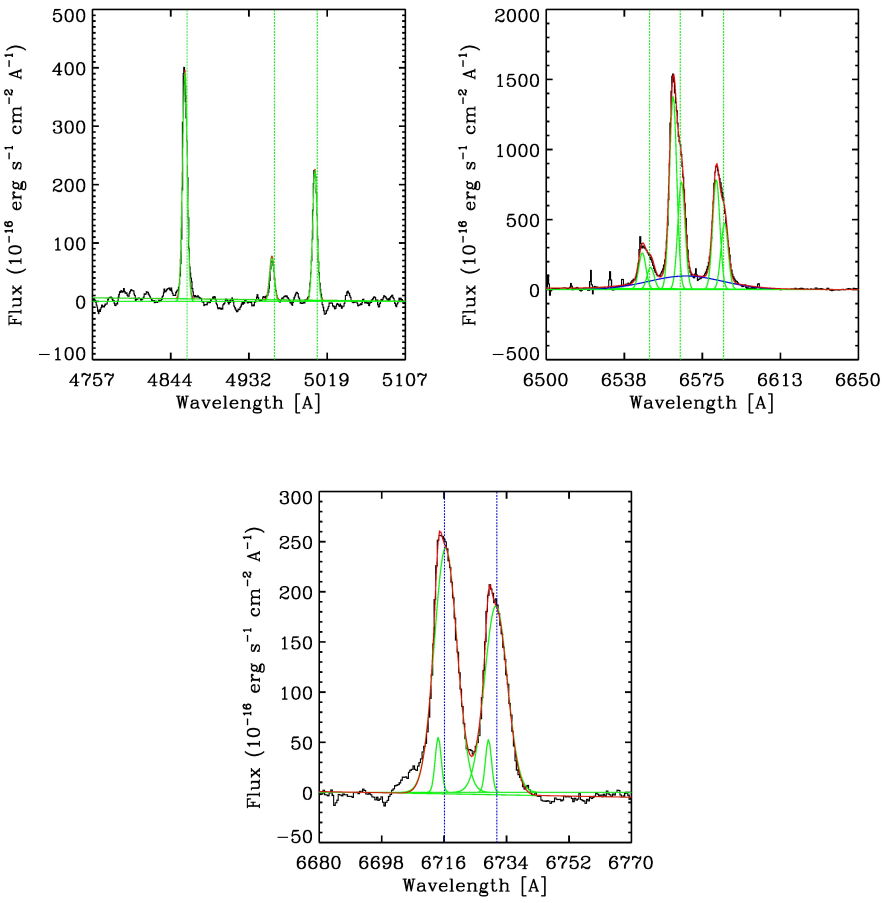

Figure 3.11: Spectra as in Fig. 3.3 for NGC613.

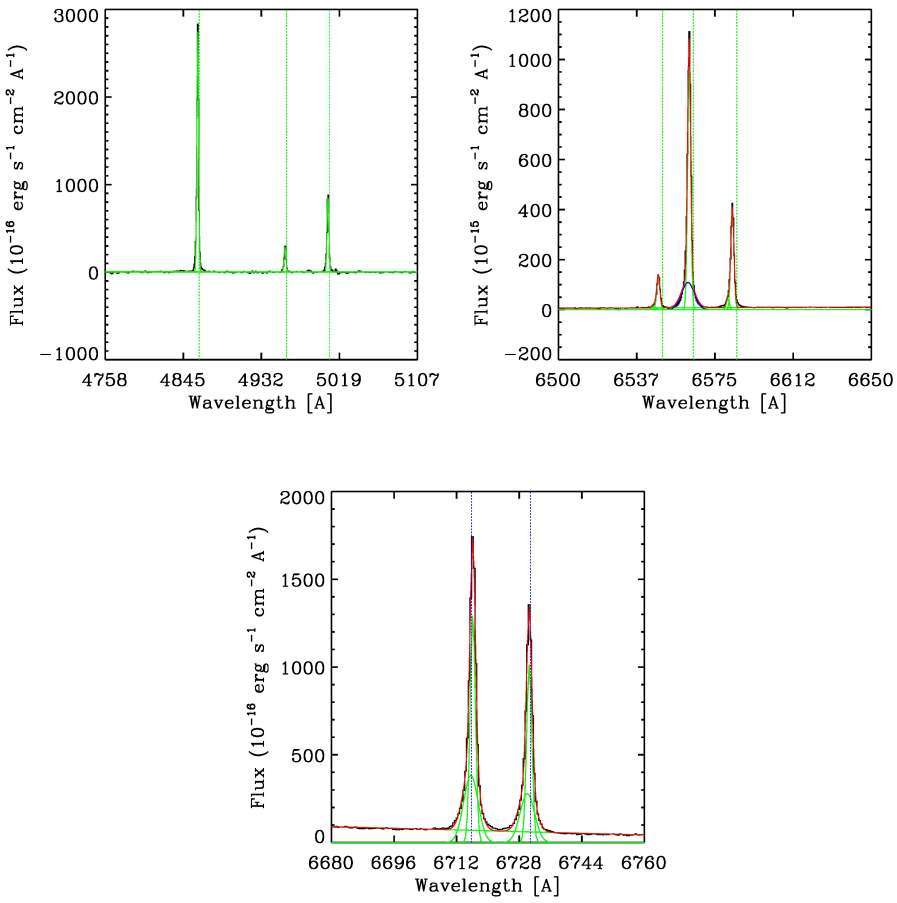

Figure 3.12: Spectra as in Fig. 3.3 for NGC4691.

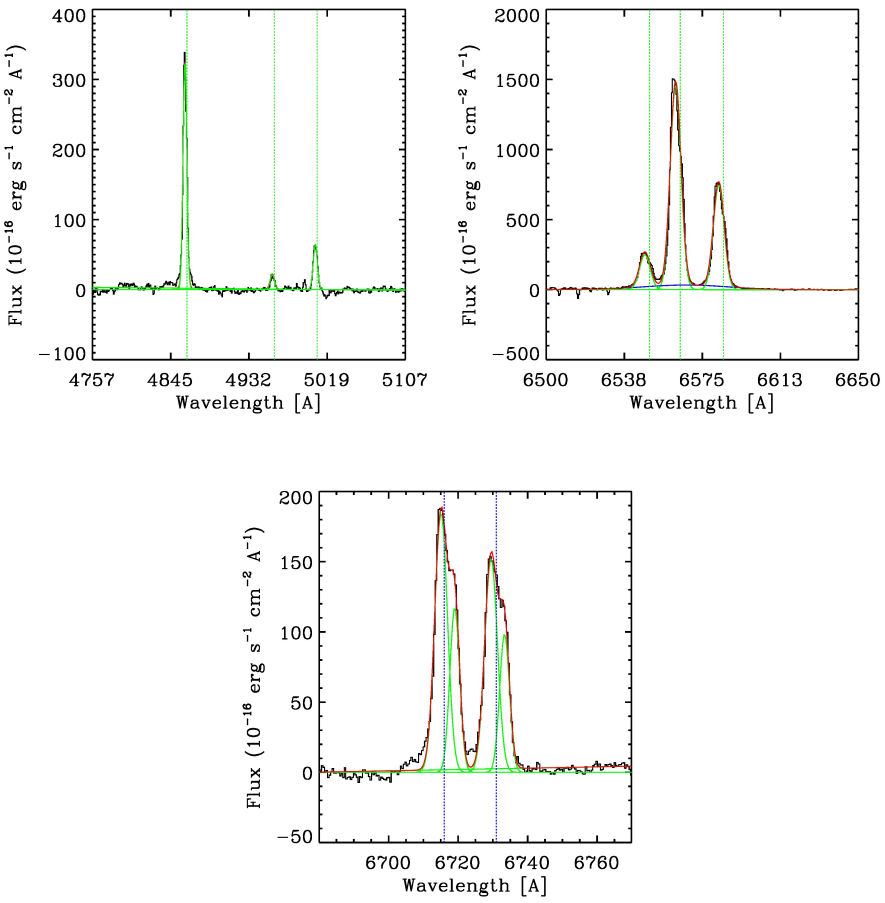

Figure 3.13: Spectra as in Fig. 3.3 for NGC6000.

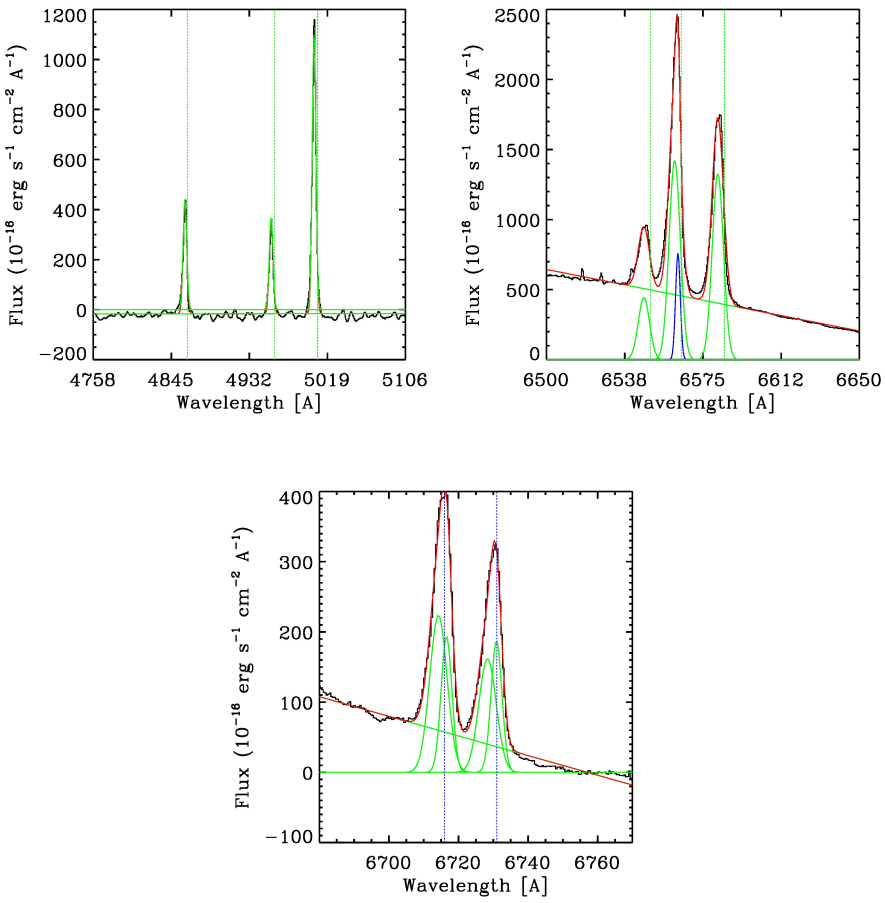

Figure 3.14: Spectra as in Fig. 3.3 for NGC7582.

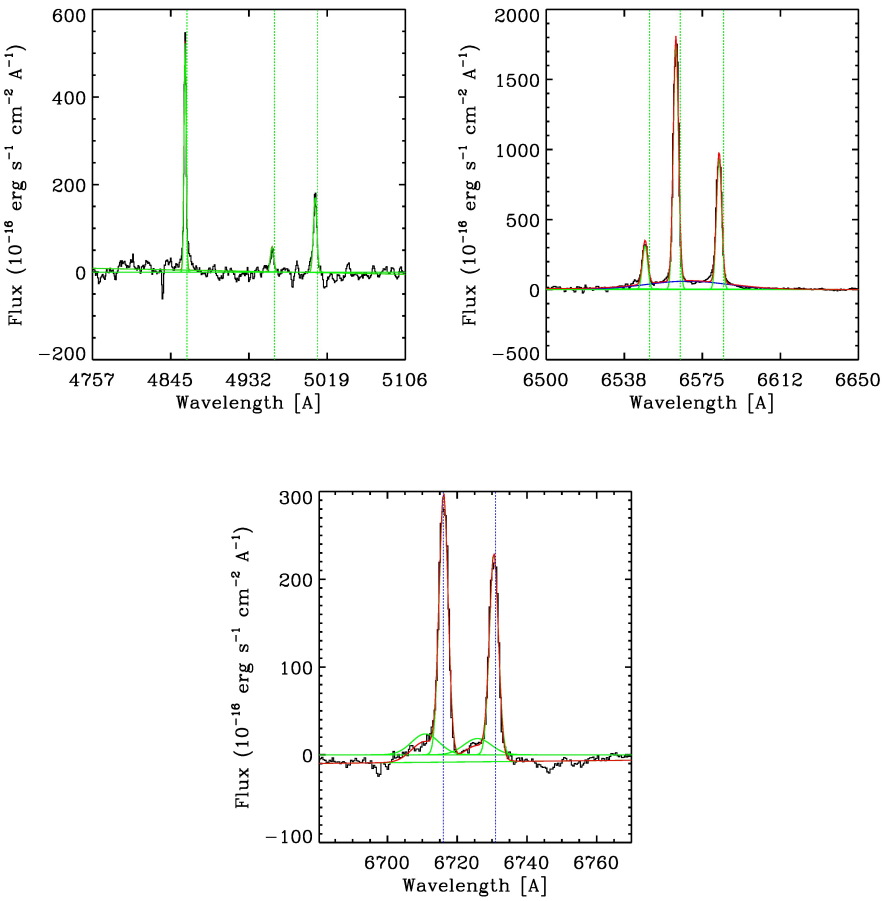

Figure 3.15: Spectra as in Fig. 3.3 for NGC4303.

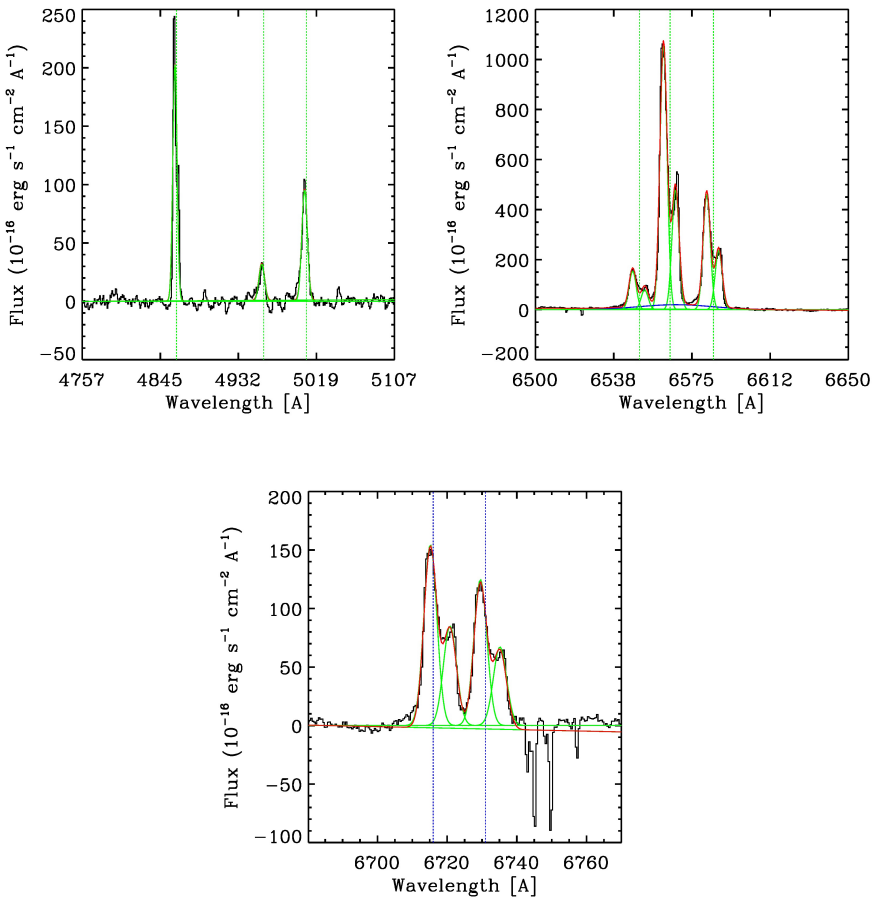

Figure 3.16: Spectra as in Fig. 3.3 for NGC5990.

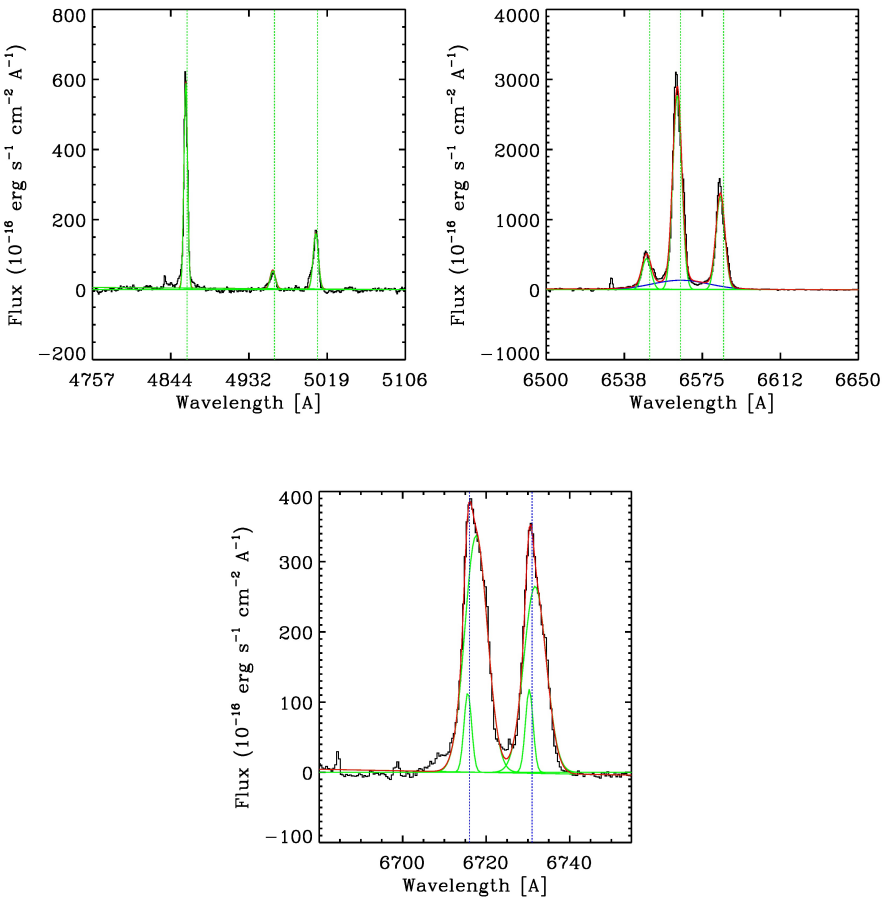

Figure 3.17: Spectra as in Fig. 3.3 for NGC6221.

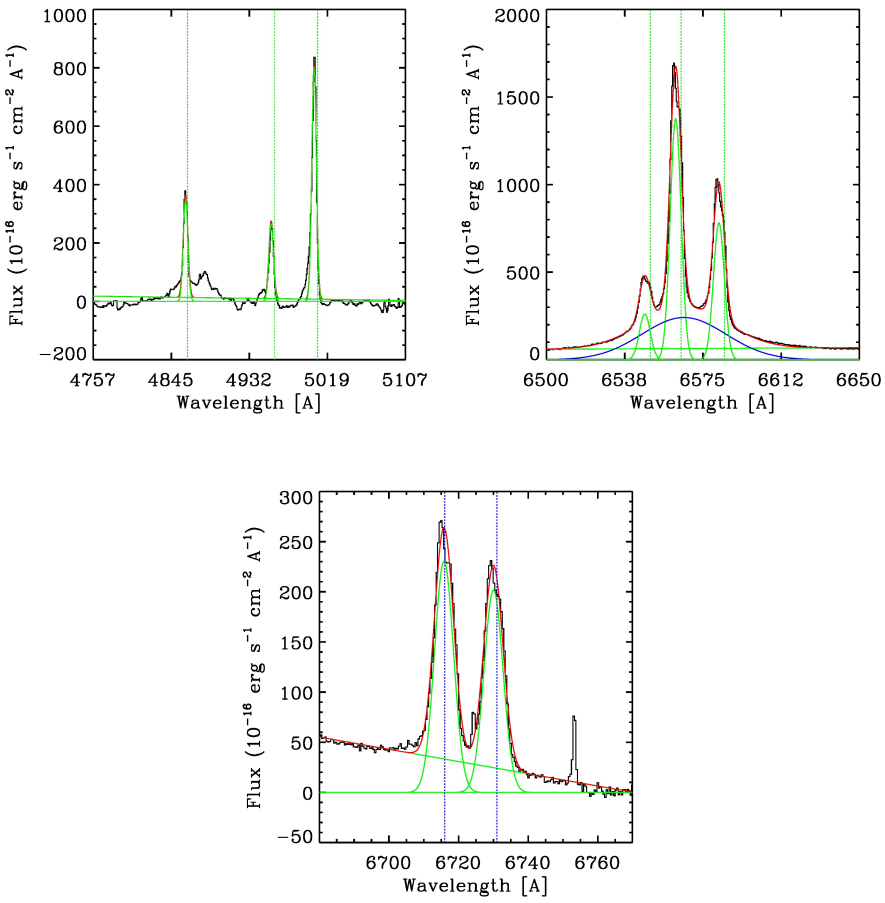

Figure 3.18: Spectra as in Fig. 3.3 for NGC7469.

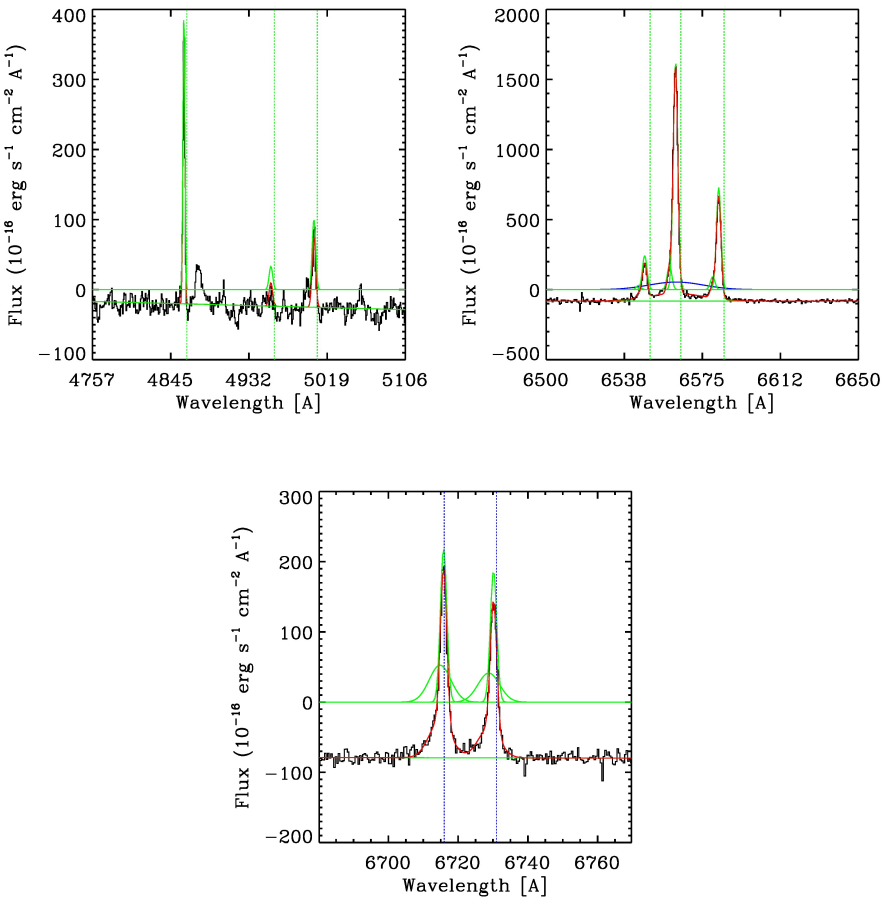

Figure 3.19: Spectra as in Fig. 3.3 for NGC7496.

Chapter 4

ALMA observations of cold molecular gas in AGN hosts at $z \sim$1.5 - Evidence of AGN feedback?

Published as D. Kakkad, V. Mainieri, M. Brusa, P. Padovani, S. Carniani, C. Feruglio, M. Sargent, B. Husemann, A. Bongiorno, M. Bonzini, E. Piconcelli, J. D. Silverman, W. Rujopakarn; MNRAS, 468, 4205 (2017)

Abstract: Similarly to the cosmic star formation history, the black hole accretion rate density of the Universe peaked at $1< z <3$. This cosmic epoch is hence best suited for investigating the effects of radiative feedback from AGN. Observational efforts are underway to quantify the impact of AGN feedback, if any, on their host galaxies. In this chapter, we present a study of the molecular gas content of AGN hosts at z$\sim$1.5 using CO[2-1] line emission observed with ALMA for a sample of 10 AGNs. We compare this with a sample of galaxies without an AGN matched in redshift, stellar mass, and star formation rate. We detect CO in 3 AGNs with $L_{CO} \sim 6.3 - 25.1 \times 10^9 L_\odot$ which translates to a molecular hydrogen gas mass of $2.5 - 10 \times 10^{10} M_\odot$ assuming conventional conversion factor of $\alpha_{CO} \sim 3.6$. Our results indicate a >99% probability of lower depletion time scales and lower molecular gas fractions in AGN hosts with respect to the non-AGN comparison sample. We discuss the implications of these observations on the impact that AGN feedback may have on star formation efficiency of $z >1$ galaxies.

4.1 Introduction

In the past decade, using mm and sub-mm telescopes there has been a remarkable progress in the study of cold molecular gas content in galaxies. (e.g. Greve et al. 2005; Daddi et al. 2010; Engel et al. 2010; Tacconi et al. 2010; Davis et al. 2011; Geach et al. 2011; Bauermeister et al. 2013; Bothwell et al. 2013; Saintonge et al. 2013; Tacconi et al. 2013; Sargent et al. 2014; Genzel et al. 2015). This information provides a key ingredient to galaxy evolutionary studies as it is out of this gas that the galaxy may form stars.

Most of the molecular gas in the ISM exists in the form of molecular hydrogen (H_2). However, in the commonly used optical or radio portions of the electromagnetic spectrum, H_2 does not have any emission or absorption lines at the typical cool temperatures of the ISM, which makes it necessary to use other molecules as its tracers in most instances. The high abundance of Carbon Monoxide (CO) makes it one of the most popular tracers, although other molecules have also often been used in the literature (e.g. Gao & Solomon 2004; Greve et al. 2005; Alaghband-Zadeh et al. 2013; Gullberg et al. 2015; Heyer & Dame 2015). The collisions of the tracer molecules with H_2 results in emission of photons due to excitation or de-excitation. The emission from these tracer molecules fall in wavelength regions which are more easily observed than those of H_2. The conversion between CO luminosity and H_2 gas mass is usually parametrized through a factor, $\alpha_{\rm CO}$, which typically ranges between 0.8 and ~4 (in units of $M_\odot$ [K km s^{-1} pc^2]$^{-1}$) for galaxies with an ISM enriched to more or less the Solar abundance (e.g. Arimoto et al. 1996).

Star forming galaxies form a tight correlation between their SFR and M_* in the range of $9.5<\log M_*/M_\odot<11.5$, the so-called "main-sequence" (MS) of star forming galaxies (e.g. Daddi et al. 2007; Elbaz et al. 2007; Noeske et al. 2007; Pannella et al. 2009; Whitaker et al. 2012; Kashino et al. 2013; Rodighiero et al. 2014; Speagle et al. 2014). The MS relation is known to exist in a range of redshifts with an evolution in its normalization (e.g Whitaker et al. 2012; Bonzini et al. 2015) as well as its slope (e.g. Speagle et al. 2014; Schreiber et al. 2015). The molecular gas properties of normal galaxies on the MS and starburst (SB) galaxies lying above the MS correlation have been the subject of several studies aiming at quantifying the relation between the molecular gas content or gas fractions of these galaxies with other galaxy properties such as the SFR. Most of these studies are based on molecular gas measurements as traced by CO. Results from previous work suggest that there are in fact two modes of star formation in high redshift galaxies: a starburst one with the molecular gas usually distributed

in a compact configuration and short consumption times ($10^7 - 10^8$ years), typical of submillimetre galaxies (and local ultra-luminous infrared galaxies [ULIRGs]); and a quiescent one, with gas reservoirs distributed in extended disks and longer consumption times (10^9 years), which is observed on the MS at $z > 1$ (and in local spiral galaxies) (Daddi et al. 2010; Genzel et al. 2010; Sargent et al. 2014; Silverman et al. 2015).

AGNs could play an important role in regulating the ISM content of their host galaxies through radiative winds and mechanical energy, which, if powerful enough, could have the capability to sweep the entire galaxy clean of gas, a process generically named radiative mode of "AGN feedback" (see review by Fabian 2012). AGN feedback has also been invoked to reduce the number of massive galaxies, which otherwise is over-predicted by simulations assuming ΛCDM cosmology (Silk & Mamon 2012). The redshift range $1< z <3$ presents an interesting laboratory to test radiative feedback from AGNs as this epoch witnessed the peak accretion activity of black holes and high star formation rate in the universe (e.g. Lilly et al. 1996; Shankar et al. 2009; Madau & Dickinson 2014). There has been growing evidence of powerful and extended kiloparsec scale outflows from these high redshift quasars (Harrison et al. 2012; Brusa et al. 2015a; Perna et al. 2015a; Kakkad et al. 2016; Wylezalek et al. 2016; Wylezalek & Zakamska 2016; Zakamska et al. 2016a) which may be affecting their host galaxies by suppressing star formation in regions dominated by the outflows (Cano-Díaz et al. 2012; Cresci et al. 2015a; Carniani et al. 2016). A detailed discussion on outflows from AGN host galaxies is given in Chapter 2.

A promising way to quantify the impact that these AGN driven outflows may have on their host galaxies is by studying their cold molecular gas properties. Nowadays, a systematic study of the molecular gas properties of AGN host galaxies is still missing. Most of the molecular gas studies in AGNs have been restricted to high luminosity AGNs which usually lie above the main-sequence, in the so called starburst regime whose molecular gas properties mimic those of the non-AGN starburst population and local ULIRGs (e.g Aravena et al. 2008; Polletta et al. 2011; Riechers 2011; Villar-Martín et al. 2013; Feruglio et al. 2014; Stefan et al. 2015; Leung & Riechers 2016). Some other studies have focused on unobscured AGNs for which measurements of gas fractions are highly uncertain owing to the inaccurate stellar mass determinations.

Also, there is very little knowledge about the molecular gas content of obscured AGNs as we move to lower bolometric luminosities at $z > 1$, which coincides with the peak of the star formation and black hole accretion activity in the universe. Mullaney et al. (2015) showed that most of these low-to-moderate

luminosity AGNs lie on the MS of the star forming galaxies which make them an ideal choice for comparative study between AGNs and normal star forming galaxies without an AGN. Throughout this chapter, we define "non-AGN" galaxies as those which lie on the MS of star forming galaxies and have an X-ray luminosity (2-10 keV) less than 10^{42} erg/s, while any object above this X ray luminosity is regarded as an AGN.

In this chapter we present an investigation of the molecular gas properties of 10 obscured AGNs at z∼1.5 with the Atacama Large Millimeter/sub-mm Array (ALMA) selected based on their position on the MS of star forming galaxies. Our ultimate aim is to compare the gas properties of the AGN sample with those of the non-AGN star forming population to infer if there is a difference in the gas content and consequently the star formation process between the two groups.

This chapter is arranged as follows: Section 4.2 mentions our strategy for selecting the AGN sample. Observation parameters and details about the data reduction are summarized in Sect. 4.3. Sect. 4.4 describes the results obtained and their implications for the big picture. Sect. 4.5 discusses our results, while in Sect. 4.6 we present our conclusions.

4.2 Target selection

We focus our study on a sample of AGNs at z ∼1.5, close to the epoch of peak accretion activity of black holes, ideal for testing radiative AGN feedback. We chose AGNs with host galaxies on the MS where most of the moderate luminosity AGN and non-AGN host galaxies are located (Mullaney et al. 2015). The non-AGN galaxy sample matched in M_*, SFR and z forms a key component of this study since it is with respect to this population that the molecular gas properties of our AGN sample will be compared to. We restrict our AGN sample to moderate luminosity ($L_{bol} \approx 10^{43-46}$erg/s) obscured AGNs which sets this study apart from previous work, which has focused on high luminosity AGNs ($L_{bol} > 10^{46}$erg/s) which usually lie above the MS. Our selection criteria aim at probing the molecular gas properties of the general moderate luminosity AGN population.

Numerous parametrizations have been used for the MS of star forming galaxies in the literature (e.g. Pannella et al. 2009; Whitaker et al. 2012; Schreiber et al. 2015). Each MS locus has been derived from a different sample and they suffer from many selection effects (Renzini & Peng 2015). For the purpose of this work, we adopt one of the most recent parametrization from Schreiber et al. (2015) which uses a large sample of galaxies to investigate the redshift evolution of the

MS in the CANDELS field. Their sample is mass complete above 2×10^{10} $M_\odot$ and is able to trace the higher end of the MS slope more accurately compared to previous works.

We selected our AGN sample in the X-ray band which is almost free from contamination by other sources such as normal star forming regions. We started with ~4500 AGNs merging the Chandra and XMM-Newton surveys of the COSMOS field (Brusa et al. 2010; Civano et al. 2012), the Chandra survey of the Extended Chandra Deep Field South (E-CDFS: Lehmer et al. 2005), and the 4Ms Chandra observations of the Chandra Deep field South (CDFS: Xue et al. 2011). All these survey areas have extensive multi-wavelength coverage from the radio to the UV band, which allow a proper physical characterization of the galaxy properties (e.g. stellar mass, star formation rate, morphology), (Tozzi & Norman 2001; Szokoly et al. 2004; Mainieri et al. 2005; Brusa et al. 2010; Salvato et al. 2011; Civano et al. 2012; Bongiorno et al. 2012; Rosario et al. 2012). Out of this large X-ray sample, we considered only those targets which have high quality flag for secure spectroscopic redshift determination (Class 3 and 4 according to convention by Lilly et al. (2007)) and accurate SFR and M_* estimates. The SFR were estimated from Herschel Photoconductor Array Camera and Spectrometer (PACS) photometry using the relation SFR = $10^{-10} \cdot L_{IR}[L_\odot]$ assuming a Chabrier initial mass function (IMF). With the Herschel PACS detection, one can effectively impose a lower limit on the SFR and consequently M_*. Based on the SFR and the AGN bolometric luminosity, $L_{bol} < 10^{46} ergs^{-1}$, we do not expect any significant contamination from the AGN to the Far-Infrared (FIR) end of the spectrum (Mullaney et al. 2012; Rosario et al. 2012). The stellar masses of the host galaxies were computed using a two component (galaxy+AGN) SED fitting technique (Bongiorno et al. 2012; Bonzini et al. 2013), assuming Chabrier IMF. Typical errors associated with the parameters such as SFR, L_{bol} and M_* due to the choice of SED templates used are about a factor of 2. We refer the reader to Bonzini et al. (2015) for details about the SED fitting. Our original selection based on the MS line derived by Pannella et al. (2009) returned a sample of 10 objects, of which C92 was an outlier in the strong starburst regime (more in Sect. 4.4). However, with the new parametrization of the MS from Schreiber et al. (2015), we arrive at a final sample of 8 objects on the MS and 2 starburst galaxies, shown by the red stars in Fig. 4.1. The basic properties of all the ALMA targets are listed in Table 4.1.

As already mentioned, a key element to this study is to have a comparison sample of non-AGN galaxies on the MS. Since there is an evolution in the properties of the galaxies and black holes with redshift (e.g. Walter et al. 2016), it is important to select our sample matched in redshift. We constructed the com-

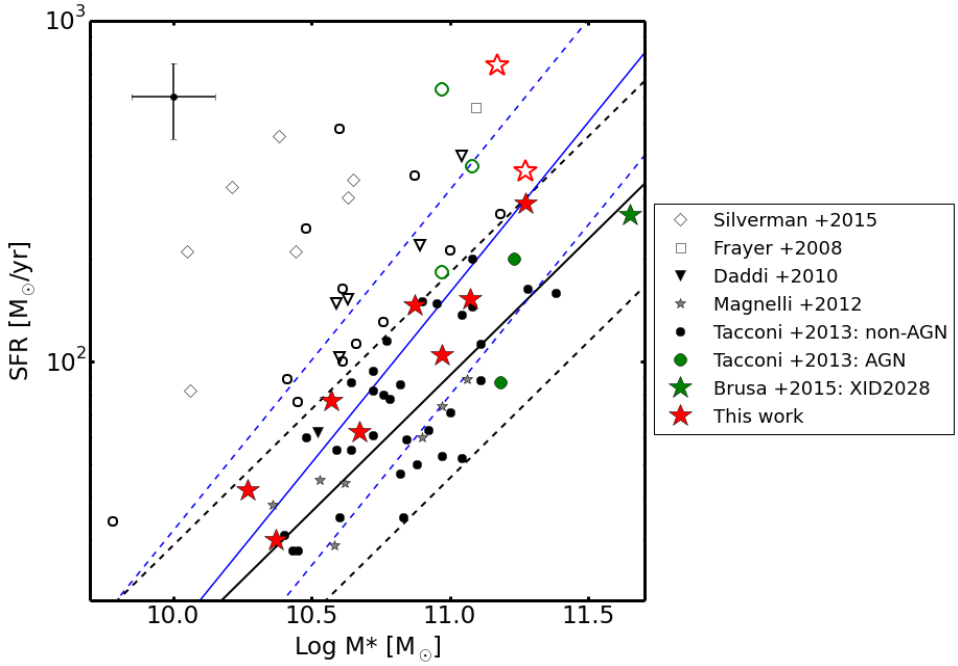

Figure 4.1: Sample selection: the solid black line corresponds to the MS line for star forming galaxies adapted from Schreiber et al. (2015) with a scatter of 0.3 dex shown by the dotted black line. Galaxies falling on the MS are shown by filled symbols while those which fall above the MS are shown by open symbols. Coloured symbols represent the AGN sample while the black and gray symbols represent the non-AGN samples. The sample from the literature are from Silverman et al. (2015); Frayer et al. (2008); Daddi et al. (2010); Magnelli et al. (2012); Tacconi et al. (2013) and Brusa et al. (2015b) (see legend). Our sample is shown by the red stars. The blue lines show the MS line with scatter derived from Pannella et al. (2009), the original basis of our sample selection. The error bars at the top left corner of the plot show the representative errors for the data points (~0.3 dex on both axes.)

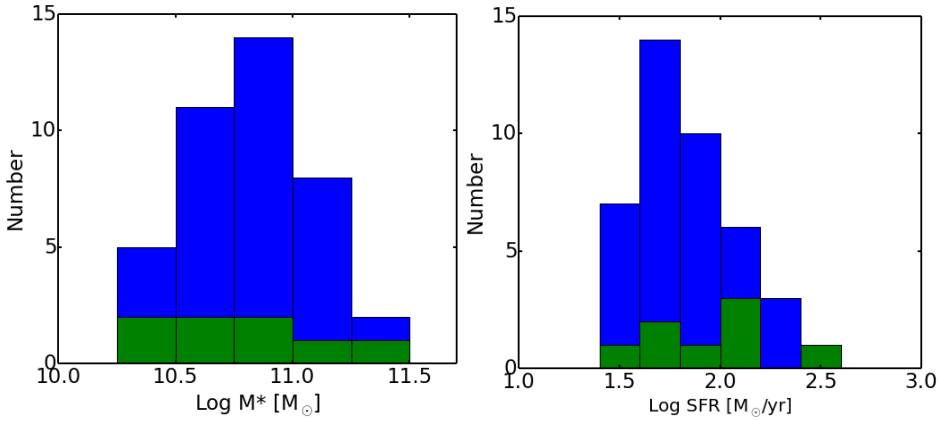

Figure 4.2: Histograms showing the M_* coverage (left) and SFR coverage (right) of the AGN sample presented in this chapter (green) and the non-AGN sample (blue).

parison non-AGN sample from the work of Daddi et al. (2010); Tacconi et al. (2013) and Magnelli et al. (2013) for which the molecular gas measurements are available from CO observations using IRAM-PdBI. We refer the reader to the corresponding papers for further details about the observations and parent sample. We selected only those objects falling in the redshift range $1 < z < 2$ and on the MS at $z \sim 1.5$. We also matched the sample from these works in SFR and M_* to that of the AGN sample to make sure we are comparing similar galaxies. This is apparent from the histograms in Fig. 4.2, which show the comparison between the M_* and SFR coverage of the AGN and non-AGN sample. All the SFR have been computed assuming a Chabrier IMF. Our final AGN sample and all the other comparison samples in the SFR-M_* plane are shown in Fig. 4.1. The red stars correspond to the ALMA sample presented in this chapter while the black and grey filled symbols are the non-AGN galaxies. The open symbols are the starburst galaxies, matched in M_* and z, to be used for analysis later to check if the properties of the AGN sample are closer to those of the non-AGN star forming galaxies or starburst galaxies. The MS line used for reference in this chapter is adapted from Schreiber et al. (2015) with a dispersion of 0.3 dex, details of which were mentioned earlier in this section. The blue line corresponds to the Pannella et al. (2009) MS parametrization, based on which the sample was initially selected. All targets but C92 fall under this parametrization (within 0.3 dex). It is apparent from the figure that the AGN and the non-AGN galaxy samples cover the same

range in the SFR-M_* plane. The same coverage in M_* is highly desirable given that observations at both low and high redshift galaxies point to an increasing gas fraction with decreasing stellar mass (e.g. Magdis et al. 2012; Saintonge et al. 2012; Tacconi et al. 2013).

We have complemented our ALMA main sequence AGN sample with literature AGN data (green filled symbols in Fig. 4.1). Five galaxies from the Tacconi et al. (2013) sample have been classified as AGN by matching them with the Nandra et al. (2015) AEGIS-X catalog with X ray luminosity, $L_{2-10keV} \sim 10^{42-43.5}$erg/s. Two of them are MS galaxies. XID2028 from Brusa et al. (2015b) is also a main sequence AGN. This source has been extensively studied in ionized (Perna et al. 2015a; Cresci et al. 2015a) as well as molecular (Brusa et al. 2015a) gas phases and has been shown to be in an active outflowing phase.

ID	RA (h:m:s)	DEC (° :′:″)	z^a	Log $L_{bol}{}^b$ (erg/s)	Log M_*^c ($M_\odot$)	Log $L_{IR}{}^d$ ($L_\odot$)	SFR^e ($M_\odot$/yr)	FIELD
DETECTIONS								
C1591*	10 01 43	+02 33 31	1.238	45.7	11.3	12.6	362	COSMOS
C92*	10 01 09	+02 22 55	1.581	45.4	11.2	12.8	740	COSMOS
#226	03 32 16	−27 49 00	1.413	42.8	10.9	12.2	146	CDFS
NON-DETECTIONS								
X5308	09 59 22	+01 36 18	1.285	45.5	11.0	12.0	104	COSMOS
X2522	09 57 28	+02 25 42	1.532	46.3	11.3	12.5	290	COSMOS
C1148	10 00 04	+02 13 07	1.563	46.8	11.1	12.2	153	COSMOS
C488	10 01 47	+02 02 37	1.171	45.4	10.3	11.6	42	COSMOS
C152	10 00 39	+02 37 19	1.188	45.5	10.4	11.5	30	COSMOS
C103	10 01 10	+02 27 17	1.433	45.1	10.7	11.8	62	COSMOS
#682	03 32 59	−27 45 22	1.155	43.4	10.6	11.9	77	CDFS

Table 4.1: Target properties:
[a]Secure spectroscopic redshifts obtained from optical spectra,
[b]AGN bolometric luminosities obtained as presented in Lusso et al. (2011),
[c]Host galaxy stellar mass obtained with a two component (AGN+galaxy) SED fit assuming a Chabrier IMF (Bongiorno et al. 2012; Bonzini et al. 2013),
[d]Total infra-red luminosity (8-1000μm) derived using Herschel PACS+SPIRE photometry,
[e]Host galaxy star formation rate computed fitting the UV-to-FIR (Herschel) photometry with the Berta et al. (2013) template library and converting the best fit 8-1000μm luminosity to a SFR using the Kennicutt (1998) prescription assuming a Chabrier IMF.
NOTE: Typical uncertainty in quantities such as L_{bol}, M_* and SFR, taking into account different SED templates used, is about 0.3 dex.
*These galaxies fall under the SB regime in SFR-M_* plane according to the Schreiber et al. (2015) MS parametrization.

4.3 Observations and Data analysis

The ALMA observations of the 10 AGN host galaxies were carried out in cycle 2 (Project code: 2013.1.00171.S, PI: V. Mainieri) using 35-38 12m antennas. The velocity/spectral resolution for all observations was ∼24 km/s. The observations were carried out in Band 3, with the receiver tuned to the frequency of ^{12}CO(2 − 1) emission (from now simply CO(2-1) unless otherwise specified, rest frame frequency = 230.5 GHz). The CO(2-1) transition was targeted in order to sample the extended, cool gas reservoir of our galaxies which is assumed to contain the bulk of the gas mass, thereby avoiding the uncertain excitation corrections affecting higher-J transitions. The observations were executed in three "scheduling blocks" to optimize the use of ALMA time by simultaneously detecting CO(2-1) for different objects with the same correlator configuration. The on-source exposure time was kept between ∼2.5-8 minutes depending on the sensitivity requirements. The root-mean-square (rms) noise requirements were calculated in order to obtain a 5σ detection of the CO line assuming the $L_{CO} - L_{IR}$ correlation as measured for MS galaxies in Daddi et al. (2010). We reached baselines up to 800 m resulting in beam sizes of $\sim 1.5'' \times 1.4''$ and $0.8'' \times 0.5''$. All the observed properties of each target are reported in Table 4.2. Summarizing, we have 3 CO detections and 7 non-detections.

We used the calibrated data products as delivered to us, while imaging for all the targets was done using CASA (version 4.2.2). The images were cleaned using the CASA task "CLEAN" with "natural" WEIGHTING. The spectral binning was kept below 100 km/s in order to get at least 4 channels for CO detection, assuming an average width of the CO(2-1) line of 400 km/s (Daddi et al. 2010). The exact choice of the width depended on where we get the maximum S/N ratio. Following this approach, imaging was done with velocity bins of 50 km/s for C92 and for the remaining targets we used 80 km/s. The imaging results are described in Sect. 4.4. The angular scale of the final image is 160″ and the analysis was restricted within 25″ of the field center.

To determine the rms values, we used the CASA task "immoments" to construct moment 0 maps by collapsing along the channels with CO detection (for C92, C1591 & #226) or along the channels with expected CO detection and computed rms on these maps. We did not compute rms directly from the spectrum since the noise is a function of frequency and this introduces systematic uncertainties in our measurements (Maiolino et al. 2015). For galaxies not detected in CO, the CO flux I_{CO} in Table 4.2 represents a 3-σ upper limit calculated from sensitivity reached over a channel width of 320 km/s around the expected position

of CO(2-1) line. The choice of 320 km/s velocity bin corresponds to the mean of the FWHM of CO(2-1) line from the CO detections (see also Table 4.3). Most of the undetected galaxies lie on the lower mass end of the AGN host mass distribution. Consequently, dynamical arguments suggests that we would expect a lower line width compared to the detected ones which are on the massive end of this distribution. This would lead to an expectation of lower CO luminosity than calculated using a width of 320 km/s based on previous reports on CO luminosity and linewidth relation in literature (e.g. Bothwell et al. 2013; Carilli & Walter 2013; Sharon et al. 2016). For C1591, C92 and #226, we reached a sensitivity of 0.21, 0.13 and 0.11 Jy/beam in 880 km/s, 320 km/s and 320 km/s wide spectral channels (these bins span the entire CO(2-1) line).

In case of a detection, the spectra were extracted from the ALMA cube using a circular aperture with a radius of ≈1.5" in case of C1591 and C92 and ≈1" in case of #226. We fit the CO(2-1) line using the IDL routine MPFIT (Markwardt 2012) using a single Gaussian component, through which the flux of the CO line and the errors on the fits were estimated. The continuum remained undetected for all targets. The CO flux was also measured by fitting the data in UV space with the CASA task "uvmodelfit" using a point source or an elliptical Gaussian model which gives the centroid of the line emission and the integrated flux. The line flux obtained with the fitting routine and the UV model fit were compared with each other and they agree well at one-sigma error levels.

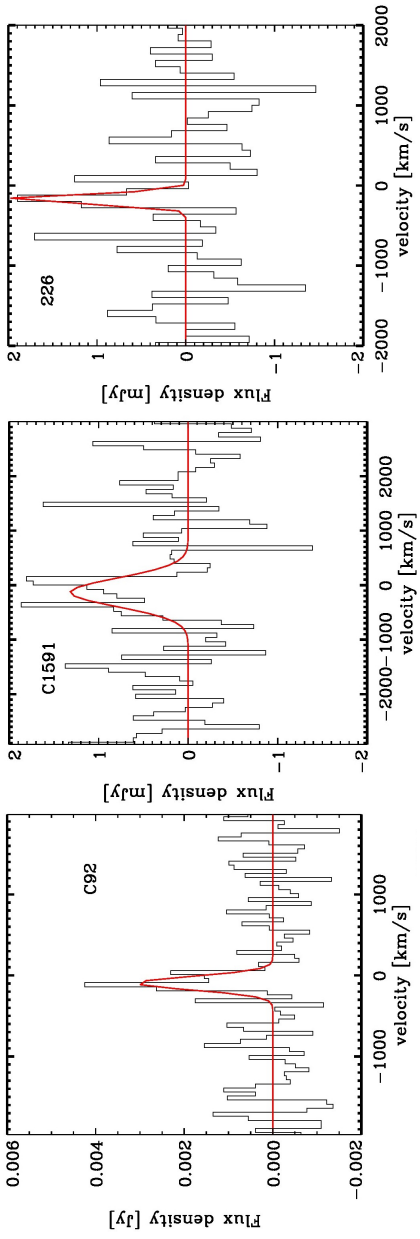

Figure 4.3: The Band 3 ALMA spectra of the three CO detected objects around the CO(2-1) line: C92 (left panel), C1591 (middle panel) and #226 (right panel). The black line corresponds to the observed spectrum while the red line corresponds to the Gaussian fit. For C92, a single channel has a width of 50 km/s while for C1591 and #226, the channel width is 80 km/s. The parameters corresponding to the Gaussian fits are given in Table 4.3.

4.4 Results and Analysis

We detect CO(2-1) emission in 3 out of the 10 targets observed with ALMA. C92 and C1591, both MS outliers, are detected with a $>5\sigma$ and $\sim4\sigma$ significance respectively, while #226, in the CDFS field and a MS candidate, is detected with $\sim3\sigma$ significance. The reported significances are observed both in the spectra and the moment (flux) maps. The statistics were obtained around a $25''$ region with respect to the field center. The results from our analysis are reported in Table 4.2.

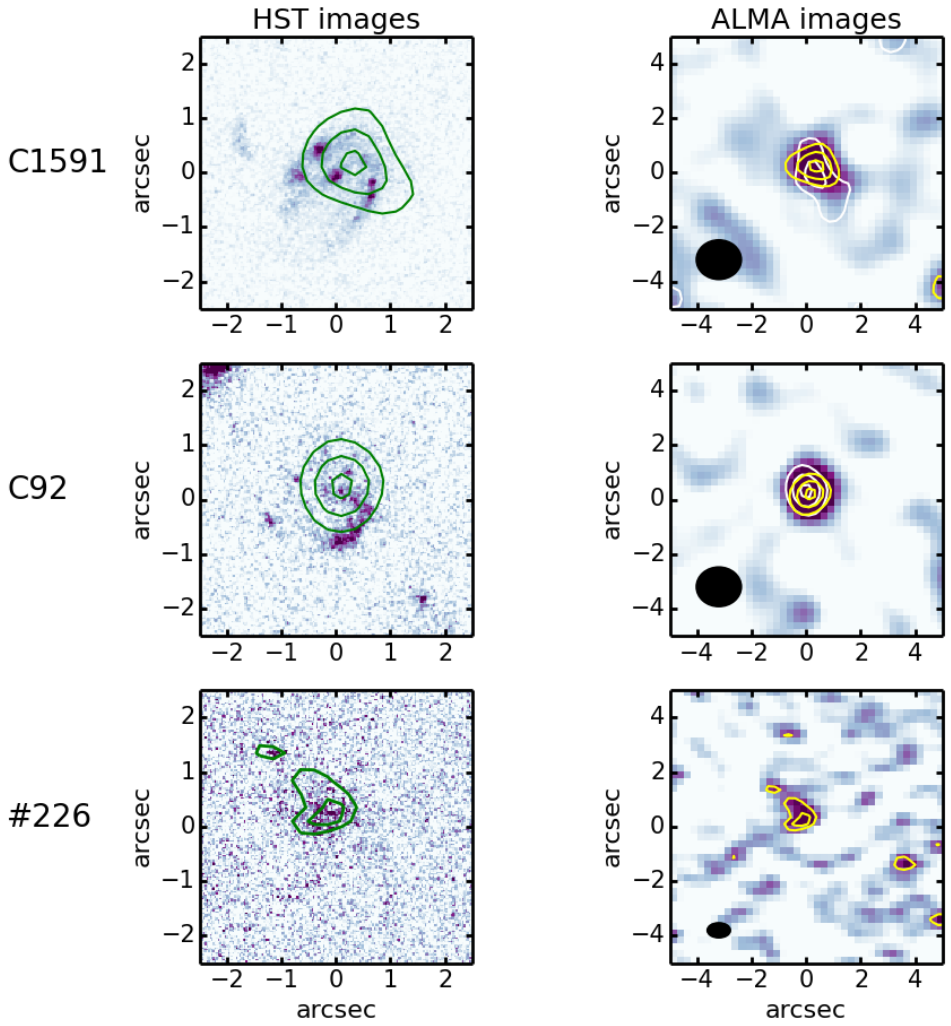

Figure 4.4: *Left panels:* HST-ACS 5″ × 5″ images of C1591 (top), C92 (middle) and #226 (bottom). The overlaid CO contours are at levels 0.6, 0.9 and 1.1 Jy km/s over a velocity bin of 880 km/s for C1591, 0.5, 0.7 and 0.9 Jy km/s over a velocity bin of 350 km/s for C92 and 0.2, 0.3 and 0.4 Jy km/s over a velocity bin of 320 km/s for #226. All the HST images show that the molecular gas traced by the CO emission line has a similar spatial extension compared to the optical/UV counterpart. *Right panels:* CO(2-1) emission line integrated maps over velocity bins of 880 km/s (C1591), 350 km/s (C92) and 320 km/s (#226). The overlaid yellow and white contours in C1591 and C92 represent the CO emission in the two peaks visible in the respective spectrum in Fig. 4.3 while the yellow contours in #226 represent the CO emission from the entire line. The CO emission in C1591 is marginally resolved. The inset ellipse is the synthesized beam during observations.
Note the different scales of the two panels, for visualization purposes. North is up and East is towards left in all the maps.

ID	z_{CO}[a]	t_{exp}[b] (s)	Beam size[c] ″×″	I_{CO}[d] (Jy km/s)	Log L'_{CO}[e] (K km/s pc^2)	M_{H_2}[f] ($M_\odot$)	f_{gas}[g]
DETECTIONS							
C1591*	1.237	151.2	1.6x1.4	0.86±0.21	10.2±2.4	10.7±2.6	0.2±0.1
C92*	1.581	151.2	1.6x1.4	1.01±0.13	10.4±1.2	11.0±1.3	0.4±0.1
#226	1.389	151.2	0.8x0.5	0.29±0.11	9.8±3.7	10.4±3.9	0.2±0.2
NON-DETECTIONS							
X5308	-	151.2	1.6x1.4	<0.60	<10.0	<10.6	<0.3
X2522	-	151.2	1.6x1.4	<0.65	<10.2	<10.8	<0.2
C1148	-	151.2	1.6x1.4	<0.65	<10.2	<10.8	<0.3
C488	-	483.84	1.5x1.4	<0.30	<9.6	<10.2	<0.5
C152	-	483.84	1.5x1.4	<0.35	<9.7	<10.3	<0.4
C103	-	483.84	1.5x1.4	<0.30	<9.8	<10.4	<0.3
#682	-	151.2	0.8x0.5	<0.60	<9.9	<10.5	<0.5

Table 4.2: Observed target properties:
[a]Redshift calculated from the observed CO(2-1) peak,
[b]On source exposure time in seconds,
[c]Beam size achieved during observations,
[d]The CO flux in Jy km/s. In case of non-detection this represents a 3σ upper limit on the flux obtained from sensitivity reached over 240 km/s channel width around the expected position of CO line (see text for further details).
[e]The CO(1-0) luminosity calculated following Solomon & Vanden Bout (2005). We employ a conversion factor of 0.8 to convert from $L_{CO(2-1)}$ to $L_{CO(1-0)}$. The values of L'_{CO} for non-detection represent the 3σ upper limit.
[f]Molecular mass calculated from CO luminosity following the canonical relation, $M_{H2} = \alpha_{CO} L'(CO)$ with α_{CO} = 3.6, commonly used in literature for MS galaxies,
[g]Gas fraction $f_{gas} = M_{H_2}/(M_{H_2} + M_*)$.
*All these galaxies are classified as starbursts according to the MS line from Schreiber et al. (2015) as mentioned in Table 4.1.

ID	v^{a}_{center} (km/s)	Δv^{b} (km/s)	f^{c} (Jy km/s)
C1591	-133.36±80	616±71	0.86±0.21
C92	-77.23±50	224±18	1.01±0.13
#226	-169.80±80	137±22	0.29±0.11

Table 4.3: Line fitting results for the three detections: [a]Central velocity of the Gaussian fit, [b]Width (full width half maximum [FWHM]) of the Gaussian, [c]Flux of the Gaussian.

During the design of our ALMA program we used the parametrization of the MS line for star forming galaxies presented in Pannella et al. (2009) which is shown by the blue line in Fig. 4.1. All targets but C92 fell uniformly along this line. For C92 we have in the meantime revised the estimate of the SFR which moved it outside the MS region. As mentioned in Sect. 4.2, we adopt here the latest parametrization of the MS from Schreiber et al. (2015) as it traces the higher mass end of the slope more accurately. Consequently, the slope of the entire MS line is flatter than the one quoted by Pannella et al. (2009)[1]. This resulted in C92 and C1591 being classified as starburst galaxies.

The extracted spectra of each detected object with the Gaussian fits to the emission line profiles are shown in Fig. 4.3 and the results of various fitting parameters are reported in Table 4.3. In all cases, the peak of the CO emission is blueshifted compared to the optical wavelengths obtained from the COSMOS & CDFS catalogue, which is apparent from the central velocity of the Gaussian fits as reported in Table 4.3. Redshifts obtained from the optical catalogues in the respective fields have been used as a reference for all the plots.

4.4.1 Molecular mass from CO

C1591 has a very broad CO emission line profile with a FWHM of 616 ± 71 km/s as shown in Fig. 4.3, middle panel. The CO emission from C1591 shows a double peaked profile suggesting a rotating galaxy. The flux map corresponding to the integrated CO profile is shown in Fig. 4.4, top right panel. The overlaid white and yellow contours are the emission from these two peaks, each of width 200 km/s. The top left panel of Fig. 4.4 shows the HST-ACS image of C1591 with CO

[1]Due to low number statistics at the high mass end, it is debated if the slope is constant throughout this range of mass.

emission line contours of the entire profile overlaid suggesting a similar extension of CO emission compared to the UV/optical image. Using CASA task *imfit*, we fit an elliptical Gaussian model to the CO(2-1) emission line integrated map over a velocity width of 880 km/s which gives values of the image component size convolved with the beam as 2.25±0.15″ and 1.51±0.16″. This suggests a marginal extension in the CO emission profile in the image. Deconvolving the image from the beam, we arrive at a half-light radius of ∼0.5″ (≡4.15 kpc) for C1591.

The CO emission line width in C92 is narrower with respect to C1591 and with a high significance of detection. Therefore, we were able to get the spectrum in smaller bins 50 km/s wide (see Fig. 4.3). A closer look suggests a double peaked CO emission profile in C92 as well and we constructed the flux maps with the overlaid contours, similar to the case of C1591. This is shown in the middle panel of Fig. 4.4. The HST map does not reveal a wider extent of molecular gas in the host galaxy compared to the UV/optical image and the CO map shows that the emission is not resolved with the synthesized ALMA beam. An X-shooter spectrum of C92, which is also known as XID60053, is available and the results were published in Brusa et al. (2015b). This object has a high extinction ($A_V \sim 6$) due to which the H_α and [OIII] emission lines are barely detected.

The marginally resolved CO emission from C1591 can be used to calculate the gas mass using the dynamical mass method which has been frequently used in literature (e.g. Carilli et al. 2010; Daddi et al. 2010; Hodge et al. 2012; Tan et al. 2014). Within a half-light radius ($r_{1/2}$), the dynamical mass for a spherically symmetric case is given by the following equation:

$$M_{dyn}(r < r_{1/2}) \simeq \frac{5\sigma^2 r_{1/2}}{G} \tag{4.1}$$

where $\sigma = \Delta v_{CO}/2.355$ is the velocity dispersion of the CO emission line with Δv_{CO} being the line width (FWHM) and G is the gravitational constant. The gas mass can then be derived by subtracting the stellar mass and the dark matter component using the following equation (Daddi et al. 2010):

$$M_{dyn} = 0.5 \times (M_* + M_{gas}) + M_{DM}(r < r_{1/2}) \tag{4.2}$$

Here we assume a dark matter component within the half-light radius to be 25% of the total dynamical mass (e.g. Daddi et al. 2010). This assumption is based on observations of local spirals (Pizagno et al. 2005) where the total mass at the half-light radius is dominated by baryons. Using this dynamical method, we obtain a gas mass of $6.0 \pm 2.4 \times 10^{10} M_\odot$ for C1591. At the redshift of C1591, HI

gas content is negligible compared to H_2, hence the reported gas mass is believed to be the mass of molecular hydrogen in the host galaxy (e.g. Neeleman et al. 2016).

For all sources, including C1591, we calculate the CO luminosity using the result from Solomon & Vanden Bout (2005):

$$L'_{CO} = 3.25 \times 10^7 \; I_{CO} \; \nu_{obs}^{-2} \; D_L^2 \; (1+z)^{-3} \tag{4.3}$$

where I_{CO} is the CO[2-1] flux in Jy km/s, ν_{obs} is the observing frequency in GHz, D_L is the luminosity distance in Mpc at redshift z. In case of non-detection, we use the rms from the measurements (see Sect. 4.3 for a description on calculation of rms) to estimate 3σ upper limits on the CO luminosity. Stacking of spectra from the sources with no detection revealed no emission lines, justifying our estimation of upper limits for these sources. In all cases, we assume an excitation correction of 0.8 to convert from $L_{CO(2-1)}$ to $L_{CO(1-0)}$[2]. The calculated CO luminosities and the upper limits are reported in Table 4.2.

The above calculated CO luminosities are then converted into molecular mass using $M_{H_2} = \alpha_{CO} L'(CO)$. α_{CO} presents the biggest systematic uncertainty in molecular gas measurements using CO since its value could lie anywhere between 0.8-3.6 (e.g. Arimoto et al. 1996; Bolatto et al. 2013) depending on various factors such as metallicity and specific SFR (sSFR) (e.g. Genzel et al. 2012; Hunt et al. 2015). For the purpose of our study, we use an α_{CO} value of 3.6, which is commonly used in literature for MS galaxies at a similar redshift as our AGN sample (e.g. Daddi et al. 2010; Tacconi et al. 2013), ignoring the possibility that AGNs might have different α_{CO} due to hard ionizing radiation (see Sect. 4.5). The gas mass measurement using the dynamical method for C1591 described above gives an α_{CO} value of 4.1±1.6 which is well within the value of 3.6 used here for all cases. To be consistent, we recalculate the molecular gas mass for the MS comparison sample using α_{CO}=3.6 and for literature data using CO[3-2] emission line, we employ an excitation correction of 2 to convert to CO[1-0] luminosity following Tacconi et al. (2013).

4.4.2 Observed relations for AGNs

The main goal of this chapter is to identify whether the presence of an AGN affects the molecular gas content of its host galaxy and consequently the star formation

[2]Literature values range from 0.7-0.85. See e.g. Frayer et al. (2008); Daddi et al. (2010); Brusa et al. (2015b); Silverman et al. (2015)

process. To answer these questions, we compare our molecular mass measurements with those of normal star forming galaxies and starburst galaxies without an AGN. Details of the comparison sample were mentioned earlier in Sect. 4.2. We stress again that the comparison sample has been matched in redshift and stellar mass to make sure we compare galaxies with similar properties.

Figure 4.5 shows the various correlations obtained for our targets in the context of the entire comparison sample. Before fitting any function to the AGN sample, we did a survival two-sample test using R function *survdiff()* implemented in python on each plot to check the probability that the AGN sample and the non-AGN sample are drawn from the same distribution. The function returns a p-value from a chi-squared distribution. For all the correlations derived in this section, we obtain a p-value of 0.008 i.e. a >99% probability that our AGN sample has a different distribution from the normal MS star forming galaxies. While deriving the correlations for AGNs, we kept the slope of the linear function to be equal to that of the MS relations for ease of comparison with the non-AGN sample.

The top left panel in Fig. 4.5 shows L'_{CO} vs. L_{IR} plot for galaxies between redshift 1 and 2. The infrared luminosity, L_{IR} here represents the total infrared luminosity for all the sample in the plot. The color coding of different points is the same as in Fig. 4.1. We employ a standard excitation correction of 0.8 to convert from CO(2-1) luminosity to CO(1-0) luminosity for our as well as all the comparison samples for consistency. First of all, we do not find a significant difference in the L'_{CO}-L_{IR} correlation for MS and non-AGN starburst galaxies as reported in previous works such as those of Genzel et al. (2010), Sargent et al. (2014), and Tacconi et al. (2013). These works used a compilation of local as well as high redshift galaxies. However, when we only consider the high redshift galaxies between $1< z <2$, only one correlation is required to describe the star burst and MS population in the L'_{CO}-L_{IR} plane given by the following mean equation adapted from Sargent et al. (2014) for MS galaxies and shown as a black line in Fig. 4.5, upper left panel:

$$Log\ L'_{CO}[L\odot] = (0.81 \pm 0.03) \cdot Log\ L_{IR}[L\odot] + (0.54 \pm 0.02) \tag{4.4}$$

This is consistent with the more recent results (e.g. Genzel et al. 2015; Silverman et al. 2015). Our MS AGN sample lie below this correlation and considering all the 3σ upper limits as detections, we derive an average best-fit function for L'_{CO}-L_{IR} correlation for AGNs:

$$Log\ L'_{CO}[L\odot] = 0.81 \cdot Log\ L_{IR}[L\odot] + (0.25 \pm 0.35) \tag{4.5}$$

This is given by the red line in Fig. 4.5, upper left panel. Thus the mean L'_{CO}-L_{IR} correlation for AGNs is a factor "at least" 2 lower than that of main sequence non-AGN galaxies. Such a trend is also recovered in a flux-flux plot as well. We also stress here that the derived line for AGNs is itself an upper limit since most of the data points used to fit this correlation are upper limits.

The difference in the properties of the two sets of galaxies (non-AGN star forming and the starburst galaxies) becomes apparent once we convert these CO luminosities into gas masses and this is shown in Fig. 4.5, top right panel. The solid and the dotted lines are the average correlations obtained by Sargent et al. (2014), where the dotted line indicates the limiting locus for starbursts which are strong outliers to the MS and have among the largest star formation efficiencies (SFEs). This plot is an ideal indicator of the SFE. The galaxies that follow a lower correlation, such as the starburst galaxies along the dotted black line, have a higher SFE compared to those following a higher correlation, such as the MS galaxies along the solid black line. This is because for the same molecular gas mass, there is more star formation in the SB galaxies compared to MS galaxies. Our AGN host galaxies on the MS are consistently below the average MS line in the M_{H_2} − SFR plane indicating that the star formation efficiency of the AGN host galaxies is higher than for the non-AGN population. We derive the functional form for the best fit relation for the AGNs in the MS (taking the upper limits as detections):

$$Log\ M_{H_2}[M_\odot] = 0.81 \cdot Log\ SFR[M_\odot/yr] + (8.90 \pm 0.35) \tag{4.6}$$

The intercept for this equation is a factor of ∼2 lower than the average line for the MS galaxies (see Sargent et al. (2014) for the best fit M_{gas} − SFR relation for main sequence non-AGN galaxies). These values thus support our assertion above that AGN host galaxies tend to have a higher SFE compared to M_* and SFR matched non-AGN galaxies. We note here that the α_{CO} value adopted for our galaxies is the same as for the main sequence non-AGN population used in this study. In a scenario where hard ionizing radiation from AGNs could destroy these molecules, conversion factor α_{CO} would be lower for AGN host galaxies and the estimated gas mass would decrease even further. This argument is further strengthened once we take into account the single detection we have from ALMA which is well below the locus of the MS galaxies. In fact, this detection falls in the region of the starburst galaxies in the M_{H_2} − SFR plane at this redshift. The AGN host galaxies which are starbursts also fall into the same region which confirms previous results that starbursting AGN hosts have properties similar to those of

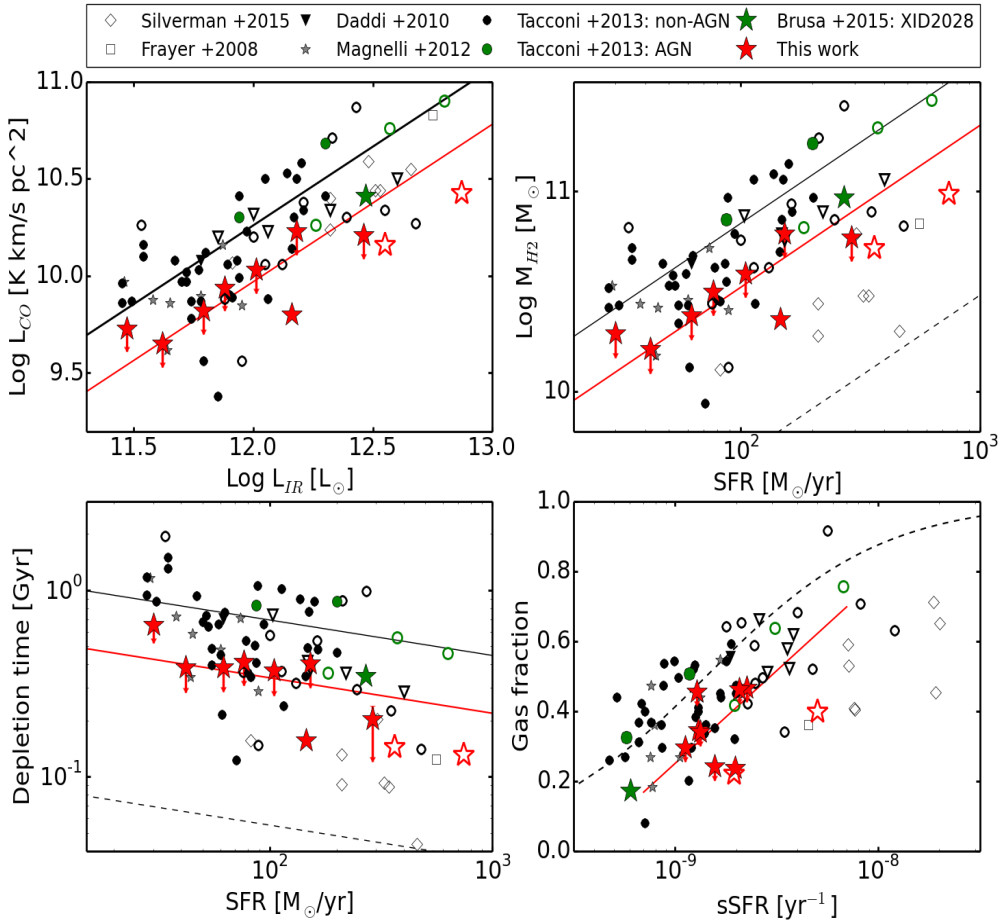

Figure 4.5: In all plots, the colored symbols represent the AGN sample from this work (red stars-filled and unfilled) and the previous works (green symbols). The filled symbols represent the main sequence galaxies while the open symbols represent the starburst population. The red line represents the best fit for AGNs in the MS, considering all the 3σ upper limits as detections. *Top left panel:* CO luminosity vs. total infrared luminosity. The solid black line is the correlation adapted from Daddi et al. (2010). *Top right panel:* CO based molecular gas mass measurements vs. SFR for the entire sample. We assume a conversion factor of α_{CO} to be 3.6. In our ALMA sample, we have one detection from the MS galaxies and two detections from the SB galaxies. The black solid line and the dashed line are the correlations between M_{mol} and SFR for MS galaxies and SB galaxies respectively, adapted from Sargent et al. (2014). *Lower left panel:* The depletion time (=M_{H_2}/SFR) vs. SFR plot for the entire sample. The solid and the dashed lines are the positions of the MS and SB galaxies as compiled in Sargent et al. (2014). *Lower right panel:* Gas fractions vs. specific SFR (=SFR/M_*) for the entire sample. The dotted line shows the position of main sequence non-AGN galaxies adapted from Tacconi et al. (2013).

the non-AGN starburst population.

Lower gas mass for a given star formation rate is indicative of higher SFE as discussed above and lower depletion time scales as well. This is confirmed by the depletion time scale (t_{dep} = M_{gas}/SFR) vs. SFR plot in the lower left panel of Fig. 4.5. Starbursts tend to occupy the region with lower gas depletion time scales as they are believed to be efficient in converting the available cold gas content into stars, while in the case of normal star forming galaxies, they occupy a region of higher t_{dep} (the exact functional forms of the two lines are given in Sargent et al. (2014)). The best fit relation between t_{dep} and SFR for our AGN sample in the MS is:

$$Log\ t_{dep}[Gyr] = -0.19 * Log\ SFR[M_{\odot}/yr] - (0.09 \pm 0.35) \quad (4.7)$$

Our AGN sample on the MS have depletion time scales at least a factor of 2 lower than those of the main sequence non-AGN galaxies of similar stellar mass.

Finally, for each one of our AGNs we derived the gas fraction, f_{gas} = M_{gas}/(M_{gas} + M_*) and plotted it against the specific SFR (sSFR) as shown in the lower right panel of Fig. 4.5. The gas fraction rather than the total gas content is the most appropriate parameter to use in order to compare the gas content of galaxies independently of their stellar masses. The best fit correlation for AGN host galaxies can be described using the following equation:

$$f_{gas} = 0.53 \cdot Log\ sSFR + (5.02 \pm 0.35) \quad (4.8)$$

This is shown by the solid red line in Fig. 4.5, lower right panel and the relation is valid for 10^{-9} yr^{-1} < sSFR < 10^{-8} yr^{-1}. The black dashed line in the same panel shows the best fit function for MS galaxies adapted from Tacconi et al. (2013). Although some of our data points fall within the general population of the MS galaxies, the average line fitting function for AGNs show gas fractions less by a factor of at least 2 compared to the MS galaxies. Hence, together with a higher SFE, these moderate luminosity AGN host galaxies also show a lower gas fraction.

4.5 Discussion

The observation of high SFE, lower gas depletion time scales and lower gas fractions in our AGN sample may be an indirect evidence of AGN feedback on the

host galaxy. However with the current data we cannot distinguish between a positive or a negative feedback scenario (in other words, we cannot tell if the AGNs are shifted right or down in Fig. 4.5).

Negative Feedback: As mentioned earlier, AGNs are known to host powerful outflows within their host galaxies. These outflows may drive the gas away from the galaxy, hence preventing further star formation without affecting the current star formation rate. As an example, for XID2028, it has been shown from observations with SINFONI (Cresci et al. 2015a) that this galaxy hosts a powerful outflow traced by the ionized gas. The PdBI molecular gas observation for this object using CO(3-2) emission line is shown by the green star in all the plots (Brusa et al. 2015b). Similar to the properties of our AGN sample, this target seems to have a higher SFE, lower depletion time scale and lower gas fraction compared to the "average" best fit functions of the MS galaxies. A confirmation of the depleted gas content in XID2028 comes from the molecular gas mass measurements obtained from the dust mass, which is a factor of ∼2 lower than the values obtained assuming $\alpha_{\rm CO}$ = 3.6, supporting the hypothesis that the outflow observed in the ionized gas phase may be depleting the cold molecular gas in the host galaxy.

To prove the presence of on-going outflows in our sample, we will need deeper observations in the sub-mm and near infrared regime to trace the molecular and ionized gas phase respectively. The presence of molecular gas observations coupled with the outflow power estimates in such a sample will tell us whether there is a relation between the outflow power and the available molecular gas in the host galaxy.

Positive feedback: An alternative scenario is that the AGN could in fact enhance the star formation as well which would result in an increase in the SFE of the host galaxies. Incidences of such positive AGN feedback have been reported in the literature (e.g. Croft et al. 2006; Silk 2013; Gabor & Bournaud 2014; Cresci et al. 2015c) and it is believed that the star formation is triggered in the pressurized medium as the outflows shock against the surrounding ISM. The effects of positive feedback could be investigated with high resolution 0.1" continuum and CO imaging, coupled with similar resolution star formation maps.

Change in gas phase due to AGN: If the outflows are not powerful enough to expel the gas, the strong ionizing radiation from AGNs might also have the ability to change the status of the gas by either destroying the molecules or ionizing them. This could be observed in other wavebands of the electromagnetic spectrum. Thus, a multi-wavelength approach is fundamental to understand the observations of the AGN sample presented in this chapter.

Starburst followed by an AGN phase: Lastly, the current observations would

also be consistent with a starburst episode followed by an AGN phase (Bergvall et al. 2016) and we might happen to catch the targets in the latter phase. An insight into the star formation history of the AGN sample might give us a clue about the observed correlations.

Finally it is worth noting that the AGN sample from Tacconi et al. (2013) does not show any remarkable difference in its molecular gas properties from those of the non-AGN population at odds with our sample and the target from Brusa et al. (2015a). For example, in Fig. 4.5, lower right panel, the gas fraction of the Tacconi et al. (2013) AGN sample fall almost on (or a bit above) the MS line as while our sample falls below this MS line by a factor > 2 on average. The main difference between our AGN and the AGN sample from Tacconi et al. (2013) is that our AGN are on average brighter ($L_{bol} \sim 10^{43} - 10^{47}$ erg/s) than the PHIBBS AGN (i.e. the Tacconi et al. (2013) AGN) which have X-ray luminosity of $10^{42} - 10^{43.5}$ erg/s which translates into $L_{bol} \sim 10^{43.5} - 10^{45}$ erg/s. We infer that in the case of our AGNs, the gas might have been depleted by a more powerful AGN feedback due to the higher bolometric luminosities, which are responsible for the observed lower gas fraction.

4.6 Summary and Conclusions

We have presented the molecular gas mass measurements obtained from ALMA observations of ^{12}CO[2 − 1] in a representative sample of 10 AGNs, 8 of which lie on the MS of star forming galaxies and 2 are classified as starbursts. Their selection is based on their position with the aim to compare the molecular gas fractions and SFE of these AGN hosts on the MS with a redshift, M_* and SFR matched sample of non-AGN star forming galaxies. The following points summarize results and conclusions of this work:

- We detect CO emission in 3 out of the 10 AGNs observed with ALMA, C92, C1591 and #226 with a significance of ¿5σ, ∼4σ and ∼3σ respectively. The emission line widths are in the range ∼140-620 km/s. For the rest of the sample, we use 3σ upper limits as proxy for CO luminosity for analysis.

- Molecular gas for all the objects has been determined assuming the conventional conversion factor, α_{CO} to be 3.6. For C1591, a starbursting AGN system, the observed CO emission is marginally resolved and we could use dynamical analysis as well to measure the gas mass. The gas mass measured

using the dynamical analysis agrees within the errors with that estimated using $\alpha_{CO} = 3.6$.

- Using the same conversion factor between CO luminosity and molecular gas mass for the non-AGN comparison sample and the AGN sample,we find that AGN hosts have on average a gas fraction lower by a factor of $\geq$2, higher SFR and consequently $\geq$2.3 times lower gas depletion time scales compared to non-AGN main sequence galaxies of similar stellar mass and SFR at z$\sim$1.5. In fact, the AGNs follow a different correlation compared to the non-AGN comparison sample. These differences are significant at the $> 99\%$ level.

- Our hypothesis is that the gas depletion may be an indirect evidence of the impact of AGN feedback on the host galaxy. Powerful winds from the central source might be sweeping the galaxies clean of molecular gas content and/or enhance star formation in the shocked medium. The AGN radiative field might also change the status of the ISM by heating, ionization and disruption of molecules. Multiwavelength studies of statistical samples, aimed to prove or disprove this scenario are ongoing.

Chapter 5

Conclusions and Future prospects

This thesis has presented several observational approaches to unveiling the presence of radiative AGN feedback for high redshift galaxies by analyzing the ionized gas dynamics and the molecular gas content. The following chapter summarizes the work presented in this thesis, gives an outlook of the outstanding challenges and the future work.

5.1 Summary of this thesis

I have presented two observational approaches to study the dynamics and content of ionized and molecular gas using IFS and sub-mm spectroscopy respectively. My studies focused in the redshift range 1<z<3 where galaxies are at the peak of their star formation and black hole accretion activity. The main results of the individual work are summarized below:

- **Ionized outflows in AGN host galaxies at high redshift:** For AGN with high accretion rates, radiative AGN feedback may be in the form of winds or outflows due to radiation pressure acting on the surrounding gas and dust. The aim of chapter 2 was to trace and characterize properties of AGN driven outflows for galaxies at z∼1.5 such as morphology, spatial extent, mass rate and the kinetic power. We used Integral Field Spectroscopy (SINFONI/VLT) to properly characterize the spatial extension of the outflows. The targets were pre-selected based on their peculiar values of high accretion rates and column density and one goal of our study was to validate the efficiency of this selection in tracing objects in an outflowing phase. After a careful PSF analysis, we detected extended kiloparsec scale outflows

in three out of five targets. The absence of disturbed morphology in the HST images ruled out mergers as a cause of this turbulent ionized medium. Within the assumptions of the outflow model, we came to the conclusion that the observed ionized outflows in this work and others from the literature can be driven by both star formation and the AGN. Molecular outflows on the other had show a larger coupling between their outflow kinetic power and the bolometric luminosity of the AGN suggesting that a major fraction of the outflowing mass might be in the molecular phase. Lastly, a major challenge in the estimation of ionized outflow rates is the large systematic uncertainties due to inaccurate constraints on the metallicity, velocity definitions, electron temperature and most importantly, electron density which represents the major contributor to the error budget.

- **Constraining electron densities in AGN Narrow Line Region using S7 survey:** Our SINFONI work motivated a systematic study of the electron density in the NLR of AGN host galaxies, which was the basis of chapter 3. Our aim was to better understand the density structures within the AGN host galaxies and bring down the systematic uncertainties in the mass outflow estimates. We used the sample from the *Siding Spring Southern Seyfert Spectroscopic Snapshot Survey* (S7) obtained with the optical IFU WiFeS mounted at the ANU 2.3 m telescope. These data have a high enough spectral and spatial resolution to construct electron density maps using the [SII]λ6716,6731 lines. We found that the electron densities are higher in sites with high star formation suggesting that the densities derived from the sulfur doublet are correlated with the star formation in most of the targets. This would also imply that high redshift galaxies would on average have higher electron densities since the star formation rate increases with redshift (up to z$\sim$3). Based on the electron density profiles, we expect the density to fall below 50 cm^{-3} for distance from the center of the galaxy larger than 500 pc on average. Such low density values, also in sites of [OIII]λ5007 emission from which outflow mass is usually calculated, means that the mass outflow rates might have been underestimated in recent studies where a higher density was generally assumed.

- **ALMA molecular gas observations reveal AGN feedback at high redshift:** Chapters 2 and 3 presented an overall picture of the ionized gas kinematics within the host galaxies of AGNs at low and high redshift. However as pointed out in Chapter 2, molecular gas is believed to represent the dom-

inant gas phase in these galaxies. This motivated a study of the molecular gas content in AGN host galaxies at high redshift which was presented in Chapter 4. We selected a representative sample of moderate luminosity AGNs (L_{bol} $\sim 10^{43-46}$ erg/s) hosted on the Main Sequence of star forming galaxies at redshift of z$\sim$1.5. These galaxies were observed with ALMA Band 3 to get an estimate of the molecular gas using CO(2-1) transition as a tracer. We compared the molecular gas properties of these AGN host galaxies with a comparison sample of non-AGN host galaxies or normal star forming galaxies matched in SFR, M_* and z. We detected CO in 3 out of 10 galaxies and applying 3-σ upper limits to the non-detected galaxies, we found that the AGNs occupy a separate parameter space in the M_{gas} vs. SFR plane and f_{gas} vs. sSFR plane suggesting a higher star forming efficiency and lower gas fraction in AGN host galaxies compared to normal star forming galaxies. We interpreted these observations as an evidence of AGN feedback. Future follow-up observations would be needed to further disentangle between different possibilities described in Sect. 5.2.

The chapters in this thesis are the corner stone for future works related to ionized and molecular gas studies in galaxies hosting an AGN. The resolution of the challenges surrounding the ionized gas studies targeting optical emission lines in chapters 2 and 3 will have significant impact on the upcoming surveys such as KASHz and SUPER (see Sect. 5.2). My work also shows that it is pivotal to observe multiple gas phases in a galaxy as each phase opens a new window to different physical processes. However, it is equally important to understand the systematic uncertainties without which we would never reach a conclusion on the observational front. In the next section, I will present my future projects to address some of the open issues highlighted by this thesis.

5.2 Ongoing work and future prospects

Several follow-up projects have emerged as a result of the work presented in this thesis. The following section gives an overview of my current efforts to answer some of the outstanding questions in this field:

5.2.1 Are outflows removing the molecular gas from AGN host galaxies?

There are now in the literature several examples of AGN driven outflows at both low and high redshift. While there are a few cases where these outflows are known to affect the star formation within the host galaxies (e.g. Cano-Díaz et al. 2012; Cresci et al. 2015a; Carniani et al. 2016; Maiolino et al. 2017), there has been little or no evidence that these outflows are affecting the cold molecular gas content in the AGN host galaxies, the fuel for the formation of new stars. Our work on molecular gas observations in high redshift AGN host galaxies using ALMA in Chapter 4 prompted us to follow-up a fraction of these targets with XSHOOTER to trace the presence of ionized outflows. I am the principle investigator of this project and it will test one of the plausible scenarios to explain the observations namely the "negative AGN feedback". In this scenario, we hypothesize that the outflows from the AGN are responsible for the lower molecular gas fractions in the host galaxies. The observations have been taken in April, 2017 and analysis on-going.

5.2.2 Constraining $\alpha_{\rm CO}$ in AGN host galaxies

In chapter 4 we described that one of the main limitations of measuring molecular gas content using CO as a tracer is the large uncertainty in the conversion factor from CO luminosity to molecular gas. For normal star forming galaxies, this can be done with metallicity measurements from transitions such as [OIII]5007 and [NII]6548 using relation in Eqs. 1 and 2 in Sanders et al. (2015) or methods prescribed in Maiolino et al. (2008). For galaxies hosting an AGN, these calibrations could not be applied since we will need to remove the AGN contribution to the emission lines used as metallicity calibrators. With the high S/N for [OII]3727, [NII]6548, Hβ and Hα in each pixel for a sub-sample of S7 survey data described in chapter 3, the AGN contribution can be disentangled by constructing a BPT diagram for the entire field of view and calculating the fraction of pixels for which AGN radiation has a significant contribution to the ionization. Taking this fraction into account, we can use the metallicity calibrations for star forming galaxies and consequently calculate the $\alpha_{\rm CO}$ for these AGN host galaxies using the prescriptions presented in Genzel et al. (2012). Hence, the combination of IFU and sub-mm observations can provide a more secure molecular mass estimate for these galaxies.

5.2.3 SUPER survey to reveal radiative AGN feedback

In chapter 2, we described an effective criterion to select AGNs in a blow-out phase. Similarly, a few IFU studies targeting AGN outflows have pre-selected their targets to maximize the chance of observing outflows in AGN host galaxies in order to study feedback effects. A clear limitation of these studies is that we have a selection bias towards targets expected to show an outflow and which have high luminosity. Such studies cannot provide a comprehensive picture of the general AGN population at high redshift.

The *sinfoni Survey for Unveiling the Physics and Effect of Radiative feedback* (SUPER) is designed to eliminate such selection effects by a blind selection of the AGN sample. Hence, the approach of this survey is not to pre-select AGN with already known outflows or with high chances of being in a blow-out phase (Chapter 2) but rather to cover the widest possible range in AGN properties. I am a member of this survey which has been awarded 280 hours of SINFONI observing time. The survey will map the ionized gas kinematics and short time scale star formation using the emission lines Hβ, [OIII]λ5007, Hα and in some cases [SII]λ6716, 6731 to constrain electron densities with high spatial resolution of $\sim$1 kpc using the AO capabilities of SINFONI. The targets have been selected from the combination of CDFS (Xue et al. 2011), COSMOS (Brusa et al. 2010; Civano et al. 2016) and XMM-XXL (Pierre et al. 2007) surveys. All these surveys have a wealth of multi-wavelength ancillary data which allows us to accurately estimate the SFR, M_* (for type 2 AGNs), bolometric luminosity, secure spectroscopic redshifts and black hole masses. The sample consists of both Type 1 and Type 2 AGNs in the redshift range of 2.1-2.5 covering nearly 4 orders of magnitude in bolometric luminosity and a similar range in the Eddington ratios as shown in Fig. 5.1. This survey will provide tight scaling relations between the frequency, mass, mass outflow rate and momentum rate of ionized outflows, and AGN bolometric luminosity and Eddington ratio. It will also tell us on a statistical sample of AGN if the star formation is indeed quenched by AGN-driven outflows.

The near-infrared SINFONI observations tracing the ionized gas are complemented by sub-mm data from from Atacama Pathfinder Experiment Telescope (APEX) and ALMA which will trace the dense and the diffuse molecular gas using [CI](2-1), CO(7-6) and CO(3-2) transitions. Hence, this will be one of the first surveys which will combine ionized gas dynamics with molecular gas content for a statistical sample of AGNs.

The integrated spectrum and various maps obtained for one of the target, X_N_115_23 from the SINFONI H and K band observations are shown in Figs.

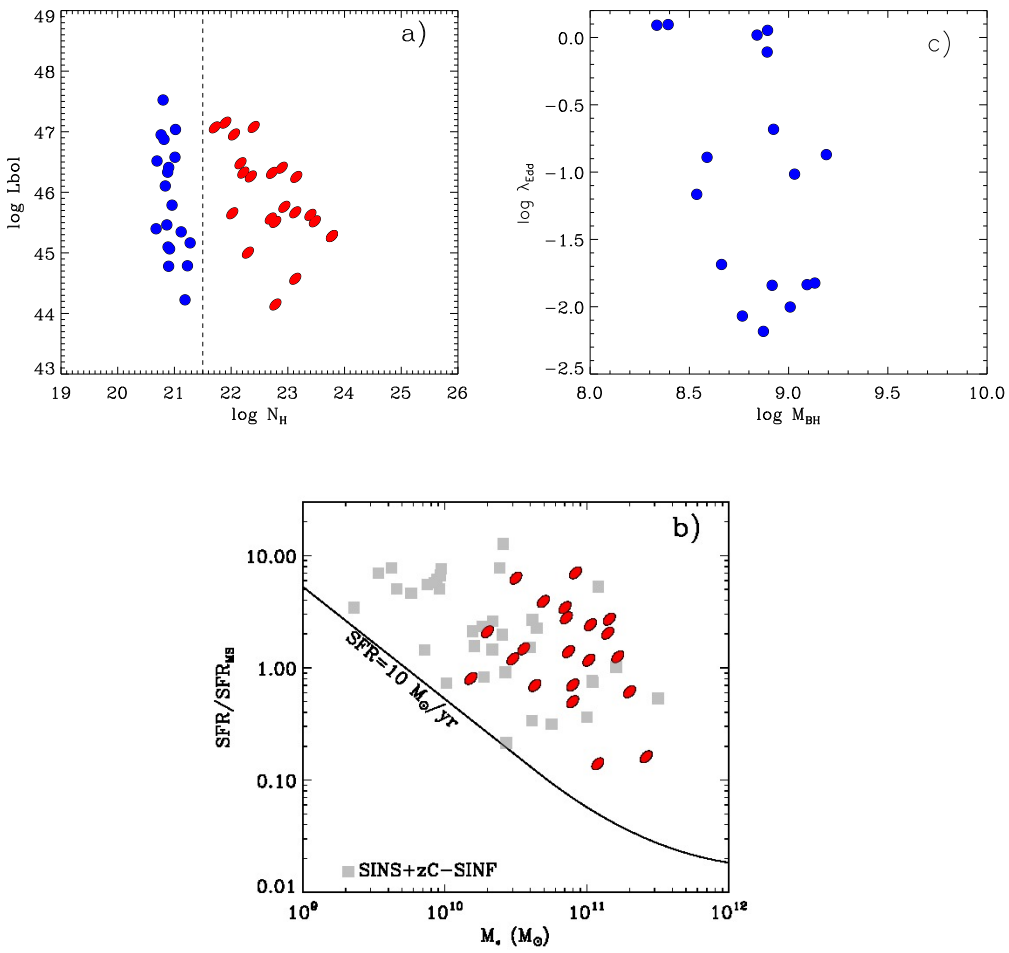

Figure 5.1: *Top left panel:* Bolometric AGN luminosities vs. column density of the SUPER targets. Blue are the Type 1 AGNs and red are type 2 AGNs. As it is apparent from the plot, the SUPER targets span ∼4 orders of magnitude in bolometric luminosity and column density. *Top right panel* The Eddington ratio vs. black hole masses for the Type 1 AGNs showing the wide range of accretion rates probed by the SUPER survey. *Bottom panel:* Normalized SFR with respect to the Main Sequence vs. Stellar mass for Type 2 AGNs obtained from SED fitting of UV to Herschel PACS band photometric data points. The red filled symbols represent the AGNs while the grey symbols represent non-AGN sample for which AO assisted SINFONI data is available with which our results will be compared.

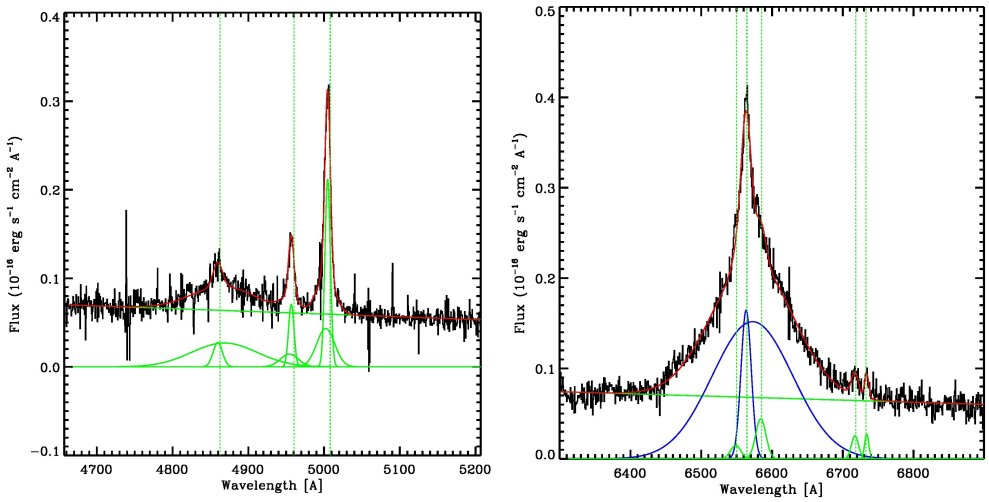

Figure 5.2: H-band (left panel) and K-band (right) integrated spectra of X_N_115_23. The wavelength on the X-axis corresponds to the rest frame wavelength. All the green lines correspond to the individual components of the fitting function used namely the continuum and the narrow Gaussians and the blue line in the K band spectrum corresponds to the broad Hα component. Vertical dashed green lines show the expected position of the emission lines.

5.2 and 5.3. Details about the emission line fitting and the definitions of velocities can be obtained in chapters 2 and 3. The H-band integrated spectrum clearly shows the presence of a broad component in [OIII] emission suggesting the presence of an outflow. The Hβ emission line shows a weak narrow component on top of a faint broad component. The Hα profile is also well reproduced using a narrow and a broad component and the high S/N in the overall spectrum allows us to map the star formation as well traced by the narrow Hα component after subtracting the broad line shown in blue (Fig. 5.2).

The presence of an outflow is apparent in the flux and the velocity maps shown in Fig. 5.3. The offset between the narrow and the broad component of [OIII] emission in the top right panel suggests the presence of an outflow in the S-E direction. This is confirmed by the velocity and velocity dispersion maps as well which show extremely high velocity outflows reaching values exceeding 1000 km/s. Judging by the velocity maps, we can infer that the outflow is not directed towards the observer, hence the actual outflow velocity should be larger than the measured 1000 km/s. Such high velocity outflows cannot be explained by star formation and supernovae driven winds. The high bolometric AGN luminosity of this target ($L_{bol} \sim 10^{46.6}$ erg/s) suggests that we are witnessing a high velocity AGN-driven outflow. These preliminary maps also suggest that the star formation as traced by the narrow Hα component is not affected by the presence of this outflow.

Another target, X_N_35_20 at a bolometric luminosity of $10^{45.1}$ erg/s (an order of magnitude less than the previous target) does not show the presence of an outflow or any [OIII] emission which shows the diversity of AGN targeted in this survey. To summarize, the SUPER survey is a promising way to understand the impact of radiative feedback on a large sample of AGN with a range in luminosities and at the end of this study, we aim to have reached a better understanding of the processes through which AGNs affect their host galaxies.

5.3 Final Remarks

Theoretical and Observational work over the last few decades have established the fact that the black hole at the centers of the galaxies is no mere ornament but plays a pivotal role in shaping the galaxies as we know today. My work in this thesis is a step towards the understanding of how this interaction actually happen. We are in an era of IFU surveys at low and at high redshifts: KMOS-3D, KROSS, KASHz, SUPER, S7, SAMI and MaNGA. The statistically significant samples targetted

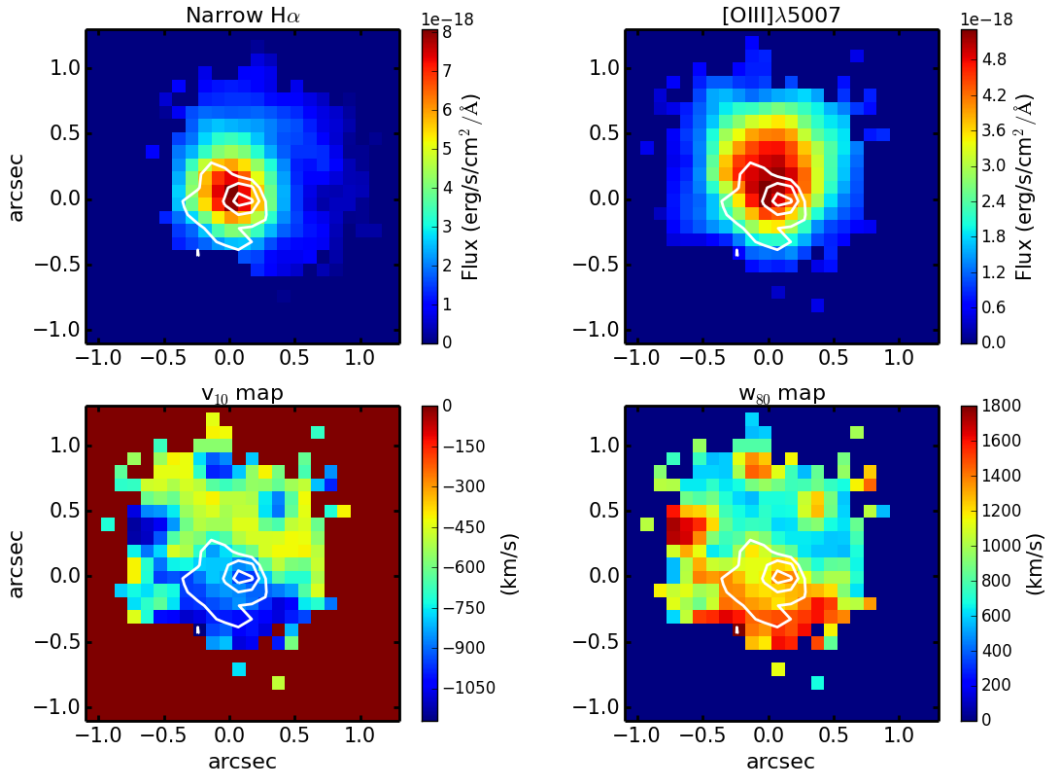

Figure 5.3: Plots showing various flux and velocity maps of X_N_115_23, one of the targets of SUPER survey. *Top left panel* shows the narrow Hα map. *Top right panel* shows the narrow [OIII]λ5007 emission. *Bottom left panel* shows the v_{10} profile which is the velocity at the 10th percentile of the [OIII] emission and *bottom right panel* shows the dispersion map as traced by the w_{80} parameter i.e. the width at 80% of the total flux of [OIII] emission. Details about the non-parametric definition of velocities can be found in chapter 2. In all the maps the white contours correspond to the broad [OIII] emission. North is up and east is towards left in all the maps.

by these surveys will help us to make significant progres in understanding galaxy evolution. Future facilities as the Large Synoptic Survey Telescope, James Webb Space Telescope, Square Kilometer Array, European-Extremely Large Telescope, ATHENA and many others over the next decade or two, will open new windows to various gas phases of the ISM across a wide range of redshifts. Hence, the study of AGNs and high redshift galaxies is here to stay in the forefront of extra-galactic astronomy in the upcoming years.

Appendix A

List of acronyms used in this thesis

AEGIS	All-Wavelength Extended Groth strip International Survey
AGN	Active Galactic Nuclei
ALMA	Atacama Large Millimeter/sub-millimeter Array
ANU	Australian National University
AO	Adaptive Optics
APEX	Atacama Pathfinder Experiment Telescope
ATHENA	Advanced Telescope for High ENergy Astrophysics
BLR	Broad Line Region
CANDELS	Cosmic Assembly Near-infrared Deep Extragalactic Legacy Survey
CASA	Common Astronomy Software Application
CDFS	Chandra Deep Field South
CDM	Cold Dark Matter
COSMOS	COSMOlogical evolution Survey
E-CDFS	Extended Chandra Deep Field South
E-ELT	European Extremely Large Telescope
ENLR	Extended Narrow Line Region
ESA	European Space Agency
ESO	European Southern Observatory
FOV	Field-of-View
FIR	Far-infrared
FWHM	Full Width at half Maximum
GMC	Giant Molecular Clouds
GMOS	Gemini Multi-Object Spectrograph
HARMONI	High Angular Resolution Monolithic Optical and Near-infrared Integral field spectrograph

HST	Hubble Space Telescope
IDL	Interactive Data Language
IFS	Integral Field Spectroscopy
IFU	Integral Field Unit
IGM	Intra-Galactic Medium
IMF	Initial Mass Function
IR	Infrared
IRAM-PdBI	Institut de Radio Astronomie Millimétrique- Plateau de Bure Interferometer
ISM	Interstellar Matter
JHU	John Hopkins University
JWST	JAmes Webb Space Telescope
KASHz	KMOS AGN survey at High-redshift
KMOS	K-band Multi-Object Spectrograph
KROSS	KMOS Redshift One Spectroscopic Survey
L.A. Cosmic	Laplacian Cosmic Ray Identification procedure
LINER	Low Ionization Nuclear Emission Region
LMIRCam	Large binocular telescope Mid InfraRed Camera
LZIFU	LaZy Integral Field Unit
M_*	Stellar mass
MaNGA	Mapping Nearby Galaxies at Apache point observatory
MIR	Mid-infrared
MS	Main Sequence
NASA	National Aeronautic and Space Administration
NGC	New General Catalog
NLR	Narrow Line Region
NRAO	National Radio Astronomy Observatory
PACS	Photoconductor Array Camera and Spectrometer
PHIBBS	IRAM Plateau de Bure HIgh-z Blue Sequence Survey
PMAS	Potsdam Multi-Aperture Spectrophotometer
pPXF	penalized PiXel Fitting
PSF	Point Spread Function
PWV	Precipitable Water Vapor
PYWIFES	Python based data reduction pipeline for WiFeS
QSO	Quasi Stellar Object
S/N	Signal-to-noise
S7	Siding Spring Southern Seyfert Spectroscopic Snapshot survey
SAMI	Sydney-AAO Multi-object Integral Field Spectrograph
SED	Spectral Energy Distribution

SFE	Star Formation Efficiency
SFR	Star Formation Rate
SINFONI	Spectrograph for INtegral Field Observations in the Near Infrared
SMA	Sub-Millimeter Array
SMBH	Super Massive Black Hole
STScI	Space Telescope and Science Institute
SUPER	sinfoni Survey for Unveiling the Physics and Effect of Radiative feedback
ULIRGS	Ultra-Luminous InfraRed Galaxies
UV	Ultra-Violet
VLT	Very Large Telescope
WiFeS	Wide Field Spectrograph
XID	X-ray ID

Bibliography

Aird, J., Nandra, K., Laird, E. S., et al. 2010, MNRAS, 401, 2531

Alaghband-Zadeh, S., Chapman, S. C., Swinbank, A. M., et al. 2013, MNRAS, 435, 1493

Alexander, D. M., Swinbank, A. M., Smail, I., McDermid, R., & Nesvadba, N. P. H. 2010, MNRAS, 402, 2211

Alonso-Herrero, A., Sánchez-Portal, M., Ramos Almeida, C., et al. 2012, MNRAS, 425, 311

Antonucci, R. 1993, ARAA, 31, 473

Aravena, M., Bertoldi, F., Schinnerer, E., et al. 2008, A& A, 491, 173

Arimoto, N., Sofue, Y., & Tsujimoto, T. 1996, PASJ, 48, 275

Bahcall, J. N., Kirhakos, S., & Schneider, D. P. 1994, ApJL, 435, L11

Bauermeister, A., Blitz, L., Bolatto, A., et al. 2013, ApJ, 768, 132

Begelman, M. C. 2003, Science, 300, 1898

Bennert, N., Jungwiert, B., Komossa, S., Haas, M., & Chini, R. 2006, A& A, 459, 55

Bentz, M. C., Peterson, B. M., Pogge, R. W., Vestergaard, M., & Onken, C. A. 2006, ApJ, 644, 133

Bergvall, N., Marquart, T., Way, M. J., et al. 2016, A& A, 587, A72

Berta, S., Lutz, D., Santini, P., et al. 2013, A& A, 551, A100

Bian, F., Fan, X., Bechtold, J., et al. 2010, ApJ, 725, 1877

Bolatto, A. D., Wolfire, M., & Leroy, A. K. 2013, ARA& A, 51, 207

Bondi, H. 1952, MNRAS, 112, 195

Bongiorno, A., Merloni, A., Brusa, M., et al. 2012, MNRAS, 427, 3103

Bonzini, M., Mainieri, V., Padovani, P., et al. 2015, MNRAS, 453, 1079

Bonzini, M., Padovani, P., Mainieri, V., et al. 2013, MNRAS, 436, 3759

Bothwell, M. S., Smail, I., Chapman, S. C., et al. 2013, MNRAS, 429, 3047

Brusa, M., Bongiorno, A., Cresci, G., et al. 2015a, MNRAS, 446, 2394

Brusa, M., Civano, F., Comastri, A., et al. 2010, ApJ, 716, 348

Brusa, M., Feruglio, C., Cresci, G., et al. 2015b, A& A, 578, A11

Bundy, K., Bershady, M. A., Law, D. R., et al. 2015, ApJ, 798, 7

Calzetti, D., Armus, L., Bohlin, R. C., et al. 2000, ApJ, 533, 682

Cano-Díaz, M., Maiolino, R., Marconi, A., et al. 2012, A& A, 537, L8

Cappellari, M. & Emsellem, E. 2004, PASP, 116, 138

Cappelluti, N., Brusa, M., Hasinger, G., et al. 2009, A& A, 497, 635

Cappi, M. 2006, Astronomische Nachrichten, 327, 1012

Carilli, C. L., Daddi, E., Riechers, D., et al. 2010, ApJ, 714, 1407

Carilli, C. L. & Walter, F. 2013, ARA& A, 51, 105

Carniani, S., Marconi, A., Maiolino, R., et al. 2015, A& A, 580, A102

Carniani, S., Marconi, A., Maiolino, R., et al. 2016, A& A, 591, A28

Cavagnolo, K. W., McNamara, B. R., Wise, M. W., et al. 2011, ApJ, 732, 71

Chartas, G., Brandt, W. N., Gallagher, S. C., & Garmire, G. P. 2002, ApJ, 579, 169

Childress, M. J., Vogt, F. P. A., Nielsen, J., & Sharp, R. G. 2014, APSS, 349, 617

Cicone, C., Maiolino, R., Sturm, E., et al. 2014, A& A, 562, A21

Civano, F., Elvis, M., Brusa, M., et al. 2012, ApJs, 201, 30

Civano, F., Marchesi, S., Comastri, A., et al. 2016, ApJ, 819, 62

Coatman, L., Hewett, P. C., Banerji, M., et al. 2017, MNRAS, 465, 2120

Conselice, C. J., Wilkinson, A., Duncan, K., & Mortlock, A. 2016, ApJ, 830, 83

Crenshaw, D. M., Kraemer, S. B., Boggess, A., et al. 1999, ApJ, 516, 750

Cresci, G., Mainieri, V., Brusa, M., et al. 2015a, ApJ, 799, 82

Cresci, G., Marconi, A., Zibetti, S., et al. 2015b, A& A, 582, A63

Cresci, G., Marconi, A., Zibetti, S., et al. 2015c, A& A, 582, A63

Croft, S., van Breugel, W., de Vries, W., et al. 2006, ApJ, 647, 1040

Croom, S. M., Lawrence, J. S., Bland-Hawthorn, J., et al. 2012, MNRAS, 421, 872

Croton, D. J., Springel, V., White, S. D. M., et al. 2006, MNRAS, 365, 11

Daddi, E., Bournaud, F., Walter, F., et al. 2010, ApJ, 713, 686

Daddi, E., Dickinson, M., Morrison, G., et al. 2007, ApJ, 670, 156

David, L. P., O'Sullivan, E., Jones, C., et al. 2011, ApJ, 728, 162

Davies, L. J. M., Huynh, M. T., Hopkins, A. M., et al. 2017, MNRAS, 466, 2312

Davies, R. I. 2007, MNRAS, 375, 1099

Davis, T. A., Alatalo, K., Sarzi, M., et al. 2011, MNRAS, 417, 882

Debuhr, J., Quataert, E., & Ma, C.-P. 2011, MNRAS, 412, 1341

Delvecchio, I., Gruppioni, C., Pozzi, F., et al. 2014, MNRAS, 439, 2736

Di Matteo, T., Springel, V., & Hernquist, L. 2005a, NATURE, 433, 604

Di Matteo, T., Springel, V., & Hernquist, L. 2005b, NATURE, 433, 604

Dimitrijević, M. S., Popović, L. Č., Kovačević, J., Dačić, M., & Ilić, D. 2007, MNRAS, 374, 1181

D'Onofrio, M., Marziani, P., & Sulentic, J. W. 2012, Fifty Years of Quasars: From Early Observations and Ideas to Future Research, 386

D'Onofrio, M., Rampazzo, R., Zaggia, S., et al. 2016, From the Realm of the Nebulae to Populations of Galaxies, 435, 585

Dopita, M. A., Fischera, J., Sutherland, R. S., et al. 2006, ApJ, 647, 244

Dopita, M. A., Shastri, P., Davies, R., et al. 2015, ApJs, 217, 12

Eisenhauer, F., Abuter, R., Bickert, K., et al. 2003, in Society of Photo-Optical Instrumentation Engineers (SPIE) Conference Series, Vol. 4841, Instrument Design and Performance for Optical/Infrared Ground-based Telescopes, ed. M. Iye & A. F. M. Moorwood, 1548–1561

Elbaz, D., Daddi, E., Le Borgne, D., et al. 2007, A& A, 468, 33

Engel, H., Tacconi, L. J., Davies, R. I., et al. 2010, ApJ, 724, 233

Evans, I., Koratkar, A., Allen, M., Dopita, M., & Tsvetanov, Z. 1999, ApJ, 521, 531

Fabian, A. C. 2012, ARA& A, 50, 455

Fabian, A. C., Vasudevan, R. V., & Gandhi, P. 2008, MNRAS, 385, L43

Fath, E. A. 1909, Lick Observatory Bulletin, 5, 71

Faucher-Giguère, C.-A. & Quataert, E. 2012, MNRAS, 425, 605

Ferrière, K. M. 2001, Reviews of Modern Physics, 73, 1031

Feruglio, C., Bongiorno, A., Fiore, F., et al. 2014, A& A, 565, A91

Feruglio, C., Fiore, F., Carniani, S., et al. 2015, A& A, 583, A99

Ford, H. C., Tsvetanov, Z. I., Ferrarese, L., & Jaffe, W. 1998, in IAU Symposium, Vol. 184, The Central Regions of the Galaxy and Galaxies, ed. Y. Sofue, 377

Frayer, D. T., Koda, J., Pope, A., et al. 2008, ApJl, 680, L21

Gabor, J. M. & Bournaud, F. 2014, MNRAS, 441, 1615

Ganguly, R., Brotherton, M. S., Cales, S., et al. 2007, ApJ, 665, 990

Gao, Y. & Solomon, P. M. 2004, ApJ, 606, 271

Gaskell, C. M. 2009, NAR, 53, 140

Geach, J. E., Smail, I., Moran, S. M., et al. 2011, ApJl, 730, L19

Genzel, R., Pichon, C., Eckart, A., Gerhard, O. E., & Ott, T. 2000, MNRAS, 317, 348

Genzel, R., Tacconi, L. J., Combes, F., et al. 2012, ApJ, 746, 69

Genzel, R., Tacconi, L. J., Gracia-Carpio, J., et al. 2010, MNRAS, 407, 2091

Genzel, R., Tacconi, L. J., Lutz, D., et al. 2015, ApJ, 800, 20

Granato, G. L., De Zotti, G., Silva, L., Bressan, A., & Danese, L. 2004, ApJ, 600, 580

Greene, J. E. & Ho, L. C. 2005, ApJ, 630, 122

Greene, J. E., Zakamska, N. L., & Smith, P. S. 2012, ApJ, 746, 86

Greve, T. R., Bertoldi, F., Smail, I., et al. 2005, MNRAS, 359, 1165

Gullberg, B., De Breuck, C., Vieira, J. D., et al. 2015, MNRAS, 449, 2883

Gültekin, K., Richstone, D. O., Gebhardt, K., et al. 2009, ApJ, 698, 198

Hainline, K. N., Shapley, A. E., Kornei, K. A., et al. 2009, ApJ, 701, 52

Harms, R. J., Ford, H. C., Tsvetanov, Z. I., et al. 1994, ApJL, 435, L35

Harrison, C. M., Alexander, D. M., Mullaney, J. R., et al. 2016, MNRAS, 456, 1195

Harrison, C. M., Alexander, D. M., Mullaney, J. R., & Swinbank, A. M. 2014, MNRAS, 441, 3306

Harrison, C. M., Alexander, D. M., Swinbank, A. M., et al. 2012, MNRAS, 426, 1073

Hasinger, G., Cappelluti, N., Brunner, H., et al. 2007, ApJs, 172, 29

Heckman, T. M. & Best, P. N. 2014, ARA& A, 52, 589

Heyer, M. & Dame, T. M. 2015, ARA& A, 53, 583

Ho, I.-T., Medling, A. M., Groves, B., et al. 2016, APSS, 361, 280

Ho, L. C., Filippenko, A. V., & Sargent, W. L. W. 1998, in IAU Symposium, Vol. 184, The Central Regions of the Galaxy and Galaxies, ed. Y. Sofue, 463

Ho, L. C., Goldoni, P., Dong, X.-B., Greene, J. E., & Ponti, G. 2012, ApJ, 754, 11

Hodge, J. A., Carilli, C. L., Walter, F., et al. 2012, ApJ, 760, 11

Holt, J., Tadhunter, C. N., Morganti, R., & Emonts, B. H. C. 2011, MNRAS, 410, 1527

Hönig, S. F., Beckert, T., Ohnaka, K., & Weigelt, G. 2006, A& A, 452, 459

Hopkins, A. M. & Beacom, J. F. 2006, ApJ, 651, 142

Hunt, L. K., García-Burillo, S., Casasola, V., et al. 2015, A& A, 583, A114

Husemann, B., Scharwächter, J., Bennert, V. N., et al. 2016, A& A, 594, A44

Husemann, B., Wisotzki, L., Sánchez, S. F., & Jahnke, K. 2013, A& A, 549, A43

Hutchings, J. B., Holtzman, J., Sparks, W. B., et al. 1994, ApJL, 429, L1

Jun, H. D., Im, M., Lee, H. M., et al. 2015, ApJ, 806, 109

Kaasinen, M., Bian, F., Groves, B., Kewley, L. J., & Gupta, A. 2017, MNRAS, 465, 3220

Kakkad, D., Mainieri, V., Brusa, M., et al. 2017, ArXiv e-prints

Kakkad, D., Mainieri, V., Padovani, P., et al. 2016, A& A, 592, A148

Kant, I. 1905, Universal Natural History and Theory of Heaven (in English and German)

Kashino, D., Silverman, J. D., Rodighiero, G., et al. 2013, ApJl, 777, L8

Kellermann, K. I. 2015, in IAU Symposium, Vol. 313, Extragalactic Jets from Every Angle, ed. F. Massaro, C. C. Cheung, E. Lopez, & A. Siemiginowska, 190–195

Kennicutt, Jr., R. C. 1998, ARA& A, 36, 189

Kerr, R. P. 1963, Physical Review Letters, 11, 237

Kewley, L. J. & Dopita, M. A. 2002, ApJs, 142, 35

Kewley, L. J., Dopita, M. A., Leitherer, C., et al. 2013, ApJ, 774, 100

King, A. 2005, ApJl, 635, L121

King, A. & Nixon, C. 2015, MNRAS, 453, L46

King, A. & Pounds, K. 2015, ARA& A, 53, 115

King, A. R., Zubovas, K., & Power, C. 2011, MNRAS, 415, L6

Klypin, A. A., Trujillo-Gomez, S., & Primack, J. 2011, ApJ, 740, 102

Kormendy, J., Bender, R., & Cornell, M. E. 2011, NATURE, 469, 374

Kormendy, J. & Ho, L. C. 2013, ARA& A, 51, 511

La Franca, F., Onori, F., Ricci, F., et al. 2016, Frontiers in Astronomy and Space Sciences, 3, 12

Lanzuisi, G., Civano, F., Elvis, M., et al. 2013, MNRAS, 431, 978

Lehmer, B. D., Brandt, W. N., Alexander, D. M., et al. 2005, ApJs, 161, 21

Lehnert, M. D., Nesvadba, N. P. H., Le Tiran, L., et al. 2009, ApJ, 699, 1660

Leung, T. K. D. & Riechers, D. A. 2016, ApJ, 818, 196

Lilly, S. J., Le Fevre, O., Hammer, F., & Crampton, D. 1996, ApJl, 460, L1

Lilly, S. J., Le Fèvre, O., Renzini, A., et al. 2007, ApJs, 172, 70

Lípari, S. L. & Terlevich, R. J. 2006, MNRAS, 368, 1001

Liu, G., Zakamska, N. L., Greene, J. E., Nesvadba, N. P. H., & Liu, X. 2013, MNRAS, 436, 2576

Luridiana, V., Morisset, C., & Shaw, R. A. 2015, A& A, 573, A42

Lusso, E., Comastri, A., Vignali, C., et al. 2011, A& A, 534, A110

Lutz, D. 2014, ARA& A, 52, 373

Madau, P. & Dickinson, M. 2014, ARA& A, 52, 415

Magdis, G. E., Daddi, E., Sargent, M., et al. 2012, ApJl, 758, L9

Magnelli, B., Lutz, D., Santini, P., et al. 2012, A& A, 539, A155

Magnelli, B., Popesso, P., Berta, S., et al. 2013, A& A, 553, A132

Magorrian, J., Tremaine, S., Richstone, D., et al. 1998, AJ, 115, 2285

Mainieri, V., Hasinger, G., Cappelluti, N., et al. 2007, ApJs, 172, 368

Mainieri, V., Rosati, P., Tozzi, P., et al. 2005, A& A, 437, 805

Maiolino, R., Carniani, S., Fontana, A., et al. 2015, MNRAS, 452, 54

Maiolino, R., Gallerani, S., Neri, R., et al. 2012, MNRAS, 425, L66

Maiolino, R., Nagao, T., Grazian, A., et al. 2008, A&A, 488, 463

Maiolino, R., Russell, H. R., Fabian, A. C., et al. 2017, ArXiv e-prints

Maraschi, L., Ghisellini, G., & Celotti, A. 1992, ApJL, 397, L5

Marconi, A. & Hunt, L. K. 2003, ApJL, 589, L21

Markwardt, C. 2012, MPFIT: Robust non-linear least squares curve fitting, Astrophysics Source Code Library

Martini, P. & Weinberg, D. H. 2001, ApJ, 547, 12

Matsuoka, K., Silverman, J. D., Schramm, M., et al. 2013, ApJ, 771, 64

McElroy, R., Croom, S. M., Pracy, M., et al. 2015, MNRAS, 446, 2186

Mejía-Restrepo, J. E., Trakhtenbrot, B., Lira, P., Netzer, H., & Capellupo, D. M. 2016, MNRAS, 460, 187

Menci, N., Fiore, F., Puccetti, S., & Cavaliere, A. 2008, ApJ, 686, 219

Menci, N., Fontana, A., Giallongo, E., Grazian, A., & Salimbeni, S. 2006, ApJ, 647, 753

Merloni, A. 2016, in Lecture Notes in Physics, Berlin Springer Verlag, Vol. 905, Lecture Notes in Physics, Berlin Springer Verlag, ed. F. Haardt, V. Gorini, U. Moschella, A. Treves, & M. Colpi, 101

Merloni, A., Bongiorno, A., Bolzonella, M., et al. 2010, ApJ, 708, 137

Mullaney, J. R., Alexander, D. M., Aird, J., et al. 2015, MNRAS, 453, L83

Mullaney, J. R., Pannella, M., Daddi, E., et al. 2012, MNRAS, 419, 95

Müller-Sánchez, F., Prieto, M. A., Hicks, E. K. S., et al. 2011, ApJ, 739, 69

Nandra, K., Laird, E. S., Aird, J. A., et al. 2015, ApJs, 220, 10

Nayakshin, S. 2014, MNRAS, 437, 2404

Neeleman, M., Prochaska, J. X., Ribaudo, J., et al. 2016, ApJ, 818, 113

Nenkova, M., Sirocky, M. M., Nikutta, R., Ivezić, Ž., & Elitzur, M. 2008, ApJ, 685, 160

Nesvadba, N. P. H., Lehnert, M. D., De Breuck, C., Gilbert, A. M., & van Breugel, W. 2008, A& A, 491, 407

Nesvadba, N. P. H., Polletta, M., Lehnert, M. D., et al. 2011, MNRAS, 415, 2359

Noeske, K. G., Weiner, B. J., Faber, S. M., et al. 2007, ApJl, 660, L43

Nyland, K., Alatalo, K., Wrobel, J. M., et al. 2013, ApJ, 779, 173

Osterbrock, D. E. & Ferland, G. J. 2006, Astrophysics of gaseous nebulae and active galactic nuclei

Ostriker, J. P., Choi, E., Ciotti, L., Novak, G. S., & Proga, D. 2010, ApJ, 722, 642

Padovani, P. 2016, ARA& A, 24, 13

Pannella, M., Carilli, C. L., Daddi, E., et al. 2009, ApJl, 698, L116

Perna, M., Brusa, M., Cresci, G., et al. 2015a, A& A, 574, A82

Perna, M., Brusa, M., Salvato, M., et al. 2015b, A& A, 583, A72

Peterson, B. M. 1997, An Introduction to Active Galactic Nuclei

Peterson, B. M., Denney, K. D., De Rosa, G., et al. 2013, ApJ, 779, 109

Piconcelli, E., Jimenez-Bailón, E., Guainazzi, M., et al. 2005, A& A, 432, 15

Pier, E. A. & Krolik, J. H. 1992, ApJ, 401, 99

Pierre, M., Chiappetti, L., Pacaud, F., et al. 2007, MNRAS, 382, 279

Pizagno, J., Prada, F., Weinberg, D. H., et al. 2005, ApJ, 633, 844

Polletta, M., Courvoisier, T. J.-L., Hooper, E. J., & Wilkes, B. J. 2000, A& A, 362, 75

Polletta, M., Nesvadba, N. P. H., Neri, R., et al. 2011, A& A, 533, A20

Pounds, K. A., Reeves, J. N., King, A. R., et al. 2003, MNRAS, 345, 705

Reeves, J. N., O'Brien, P. T., & Ward, M. J. 2003, ApJL, 593, L65

Renzini, A. & Peng, Y.-j. 2015, ApJL, 801, L29

Riechers, D. A. 2011, ApJ, 730, 108

Rodighiero, G., Renzini, A., Daddi, E., et al. 2014, MNRAS, 443, 19

Rosario, D. J., Santini, P., Lutz, D., et al. 2012, A& A, 545, A45

Rupke, D. S. N. & Veilleux, S. 2011, ApJL, 729, L27

Rupke, D. S. N. & Veilleux, S. 2013, ApJ, 768, 75

Saintonge, A., Lutz, D., Genzel, R., et al. 2013, ApJ, 778, 2

Saintonge, A., Tacconi, L. J., Fabello, S., et al. 2012, ApJ, 758, 73

Salpeter, E. E. 1964, ApJ, 140, 796

Salvato, M., Ilbert, O., Hasinger, G., et al. 2011, ApJ, 742, 61

Sanders, R. L., Shapley, A. E., Kriek, M., et al. 2015, ApJ, 799, 138

Sanders, R. L., Shapley, A. E., Kriek, M., et al. 2016, ApJ, 816, 23

Sargent, M. T., Daddi, E., Béthermin, M., et al. 2014, ApJ, 793, 19

Schawinski, K., Koss, M., Berney, S., & Sartori, L. F. 2015, MNRAS, 451, 2517

Schmidt, M. 1963, NATURE, 197, 1040

Schreiber, C., Pannella, M., Elbaz, D., et al. 2015, A& A, 575, A74

Scoville, N., Abraham, R. G., Aussel, H., et al. 2007, ApJs, 172, 38

Scoville, N., Aussel, H., Sheth, K., et al. 2014, ApJ, 783, 84

Seyfert, C. K. 1943, ApJ, 97, 28

Shakura, N. I. & Sunyaev, R. A. 1973, in IAU Symposium, Vol. 55, X- and Gamma-Ray Astronomy, ed. H. Bradt & R. Giacconi, 155

Shankar, F., Bernardi, M., Sheth, R. K., et al. 2016, MNRAS, 460, 3119

Shankar, F., Weinberg, D. H., & Miralda-Escudé, J. 2009, ApJ, 690, 20

Sharon, C. E., Riechers, D. A., Hodge, J., et al. 2016, ApJ, 827, 18

Shirazi, M., Brinchmann, J., & Rahmati, A. 2014, ApJ, 787, 120

Silk, J. 2013, ApJ, 772, 112

Silk, J. & Mamon, G. A. 2012, Research in Astronomy and Astrophysics, 12, 917

Silk, J. & Rees, M. J. 1998, A& A, 331, L1

Silverman, J. D., Daddi, E., Rodighiero, G., et al. 2015, ApJl, 812, L23

Solomon, P. M. & Vanden Bout, P. A. 2005, ARA& A, 43, 677

Somerville, R. S. & Davé, R. 2015, ARA& A, 53, 51

Speagle, J. S., Steinhardt, C. L., Capak, P. L., & Silverman, J. D. 2014, ApJs, 214, 15

Springel, V. 2005, MNRAS, 364, 1105

Stefan, I. I., Carilli, C. L., Wagg, J., et al. 2015, MNRAS, 451, 1713

Storey, P. J. & Zeippen, C. J. 2000, MNRAS, 312, 813

Subramanian, S., Ramya, S., Das, M., et al. 2016, MNRAS, 455, 3148

Sun, A.-L., Greene, J. E., Zakamska, N. L., & Nesvadba, N. P. H. 2014, ApJ, 790, 160

Szokoly, G. P., Bergeron, J., Hasinger, G., et al. 2004, ApJs, 155, 271

Tacconi, L. J., Genzel, R., Neri, R., et al. 2010, NATURE, 463, 781

Tacconi, L. J., Neri, R., Genzel, R., et al. 2013, ApJ, 768, 74

Tadhunter, C. 2016, ARA& A, 24, 10

Tan, Q., Daddi, E., Magdis, G., et al. 2014, A& A, 569, A98

Thorne, K. S. 1974, ApJ, 191, 507

Tombesi, F., Cappi, M., Reeves, J. N., et al. 2010, A& A, 521, A57

Tozzi, P. & Norman, C. 2001, ApJ, 546, 63

Tremaine, S., Gebhardt, K., Bender, R., et al. 2002, ApJ, 574, 740

Urry, C. M. & Padovani, P. 1995, PASP, 107, 803

van Dokkum, P. G. 2001, PASP, 113, 1420

Vasudevan, R. V., Fabian, A. C., Mushotzky, R. F., et al. 2013, MNRAS, 431, 3127

Veilleux, S., Cecil, G., & Bland-Hawthorn, J. 2005, ARA& A, 43, 769

Veilleux, S., Meléndez, M., Sturm, E., et al. 2013, ApJ, 776, 27

Villar-Martín, M., Rodríguez, M., Drouart, G., et al. 2013, MNRAS, 434, 978

Walter, F., Decarli, R., Aravena, M., et al. 2016, ArXiv e-prints

Wang, J.-M., Qiu, J., Du, P., & Ho, L. C. 2014, ApJ, 797, 65

Whitaker, K. E., van Dokkum, P. G., Brammer, G., & Franx, M. 2012, ApJl, 754, L29

Wylezalek, D. & Zakamska, N. L. 2016, MNRAS, 461, 3724

Wylezalek, D., Zakamska, N. L., Liu, G., & Obied, G. 2016, MNRAS, 457, 745

Xue, Y. Q., Luo, B., Brandt, W. N., et al. 2011, ApJs, 195, 10

Zakamska, N. L. & Greene, J. E. 2014, MNRAS, 442, 784

Zakamska, N. L., Hamann, F., Pâris, I., et al. 2016a, MNRAS, 459, 3144

Zakamska, N. L., Hamann, F., Pâris, I., et al. 2016b, MNRAS

Zubovas, K. & King, A. 2012, ApJl, 745, L34

Acknowledgments

This note of thanks is dedicated to both people and places which have always been there with me during my PhD.
Thanks Vincenzo and Paolo for imparting the wisdom and helping me keep my patience during these 3 years. Your support has really been important for shaping what's of me today. Thank you Andreas for the helpful discussions and for being a very supportive supervisor. Thanks Bernd and Gergö for being amazing fellow mentors and guiding me through every step. Thanks Marcella, Giovanni, Stefano, Mike, Brent, Rebecca for the productive discussion sessions. Thanks to my mom, dad and my sisters, for always being there and believing in me.
Thank you Christine for being a wonderful office mate and an amazing friend over these 3 years. Thanks Belinda, Dinko and Kate for tolerating a child like me. We will all remember that E.4.24 is and the party office of ESO. Of course, my, oops, "our" office would have been incomplete without the cheerful whales and unicorn drawings from Anke. Belinda, Angela, Johanna, thanks for helping me understand sarcasm and even make a sign for me. Apologies I am still too bad getting sarcasm, but eventually I'll get there.
Thank you Judy, Anna, Annagrazia, Chiara, Theresa & Theresa, Adrian, Ivan, Maud, Audrey, Chris & Chris, Katha, Johanna, Fabrizio, Christian, Owen, Damien, Graham, Philip(p), Martha, Linda, Wolfgang. You guys have been amazing friends and without you, these 3 years would not have been complete. I will always remember the climbing and tap house sessions, not to forget all those "easy" hikes. I promise I will keep the tradition of taking you guys to easy hikes in future.
Now to the inanimate things, which mainly includes places which have been very dear to me during my last three years. I am very thankful to all those geological phenomenon which created these alps which allowed me to hike all those weekends to de-stress. Of course thanks to Tap house and "We make cupcakes" in Munich which has kept its promise of regular supply of beers and cakes respectively.